Natural Resources Canada | Ressources naturelles Canada

CanmetENERGY
Leadership in ecoInnovation

Modelling the Heat Transfer, Lading Response, and Pressure Relief of Crude Oil Rail Tank Cars in a Fire

Final Report for TC # R.4.D.
TP 15499E
ISBN: 978-0-660-40730-2
Catalogue Number: T44-3/26-2021E-PDF

Prepared for:
Transport Canada
c/o Kiran Shoib, A/Project Manager, Engineering, Transportation of Dangerous Goods

Prepared by:
Allan Runstedtler, Research Scientist
Robert Symonds, Research Scientist
Patrick Boisvert, Senior Research Engineer
Natural Resources Canada, CanmetENERGY-Ottawa

August 20, 2021

Canada

Disclaimer:

Neither Natural Resources Canada nor any of its employees makes any warranty express or implied, or assumes any legal liability or responsibility for the accuracy, completeness, or usefulness of its contents. Reference in the report to any specific commercial product, process, service, or organization does not necessarily constitute or imply endorsement, recommendation, or favouring by Natural Resources Canada. The views and opinions of authors expressed in this report do not necessarily state or reflect those of Natural Resources Canada.

Abstract

This report describes combined heat/mass transfer and crude oil property/reaction modeling of rail car tanks exposed to fire. The work was commissioned by Transport Canada and was carried out over several years by Natural Resources Canada/CanmetENERGY-Ottawa labs. The intent is to explore key aspects that affect heating rate, thermal response of the lading, and release of the lading through the pressure release valve (PRV), and to present case studies of fire scenarios. The cases simulated considered typical fill levels of a range of crude oils, a dilbit, and a condensate in a fully engulfing fire. The important phenomena are examined and model validation is described. Conclusions are drawn regarding which variables were found to be important for improving safety in accidents.

Key words: Boiling liquid expanding vapour explosion (BLEVE), Transport, Computational fluid dynamics (CFD) modeling, Properties, Reaction kinetics, Pool fire

Contents

1. Introduction

Transport Canada commissioned a study to determine which variables are important to consider when modelling crude oil inside a tank car that is exposed to fire conditions, and to model selected fire accident scenarios to illustrate how a lading inside a tank car may react. This work was performed by Natural Resources Canada/CanmetENERGY-Ottawa labs through experimental testing, modelling, and model validation, and this report details the results of this effort. The intent of this research is to gain a better understanding of crude oil behaviour and properties under high temperature, high pressure conditions, and to better inform standards, regulations, best practices, and emergency response for tank cars carrying flammable dangerous goods.

Given the complex nature of crude oil and the many phenomena simultaneously occurring when a tank car is exposed to fire, significant research is required to understand how these accidents scenarios may unfold. When a tank car carrying a flammable lading derails, spills and subsequent ignition are possible. The resulting fire could impinge on other nearby tank cars that have not lost containment. Heat transferred from the fire to the tank contents increases the pressure inside the tank, which may not be adequately relieved by the pressure relief valve (PRV), particularly if the PRV becomes partially blocked. The combination of increased pressure and weakening tank material can lead to rupture of the tank due to thermal tears and, under some conditions, could result in a Boiling Liquid Expanding Vapour Explosion (BLEVE).

The present work extends the capability for modeling the response of rail tank cars to fire. It introduces a higher degree of complexity in the representation of the heat transfer and the lading response than the Analysis of Fire Effects on Tank Cars model (AFFTAC model), which is a comparatively simpler and easier-to-run computer model, commonly used to evaluate thermal protection systems for tank car designs. The results of this modeling study could be compared to AFFTAC results to identify any deficiencies or large discrepancies that may exist with the simpler model, although the comparison itself is beyond the scope of this work. Several studies in the open literature, though applied to liquefied petroleum gases instead of crude oil, are instructive. Birk [1] identified important scale considerations for fire testing of pressure vessels such as the fire heat flux and the sizing of pressure release valves. D'Aulisa et al. [2] studied fire exposure of tanks containing liquefied gases such as propane. They carried out a 2-D simulation using ANSYS-Fluent® for up to the first eight minutes of fire exposure and validated the results against large-scale experimental data. Landucci et al. [3], again for liquefied petroleum gases, compared lumped models, in which the contents of a tank are assumed to have uniform properties, to a CFD model and found that there was a need for the CFD methods in predicting the temperature distribution and pressure increase in tanks. Earlier, Yu et al. [4] had developed closed-form solutions from an integral analysis for cylindrical and spherical vessels containing liquefied petroleum gases. Previous work on the heat transfer and thermal response of rail tank cars has not focussed on crude oil. Consequently, it has not considered key attributes of crude oil over the range from light, through light-medium, to medium and heavy crudes—those of viscosity, multiple boiling points of complex mixtures, the chemical reactions that occur when heated, and the pressure relief of both gases and liquids. The approach described in this report addresses these key attributes of crude oil. It is not a comparison of a CFD model *versus* a lumped model. Rather, it is a combined CFD and lumped method in which the CFD provides data such as heat and mass transfer rates and the lumped method, *via* HYSYS and Matlab, addresses other complexities such as temperature-dependent properties and chemical reaction rates. The lumped method is also used to simulate fire scenarios relatively quickly.

Over the course of this study, the optimal use of the various modeling approaches, and how to combine their contributions most effectively, was determined. The resulting combination is depicted in Figure 1.1, including some key information exchanges. A 2-D computational fluid dynamics (CFD) model of the cross-section of the tank and its contents was created to account for the heat transfer and crude oil heat-up, with an external boundary condition representing the fire. The gas and liquid properties of various crudes, and how they changed with temperature and pressure, were provided by HYSYS calculations. In return, the heat transfer information from the CFD model was utilized in HYSYS calculations to perform analysis of crude oil response in fire scenarios over long exposure times and multiple pressure relief discharges. In addition, a combined MATLAB and HYSYS calculation was used to assess the need to include crude oil chemical reactions as part of the analysis. Two additional, separate CFD studies were carried out to support the modeling effort. First, a 3-D CFD model of a pressure relief valve was developed, and analyzed for gas and liquid flow and the respective discharge coefficients. Second, a 2-D CFD model of the annular gap between the tank shell and protective jacket was performed to understand the mechanism for heat transfer from the fire, across the annulus, to the tank shell and to assess the amount of thermal protection provided by this air-filled gap.

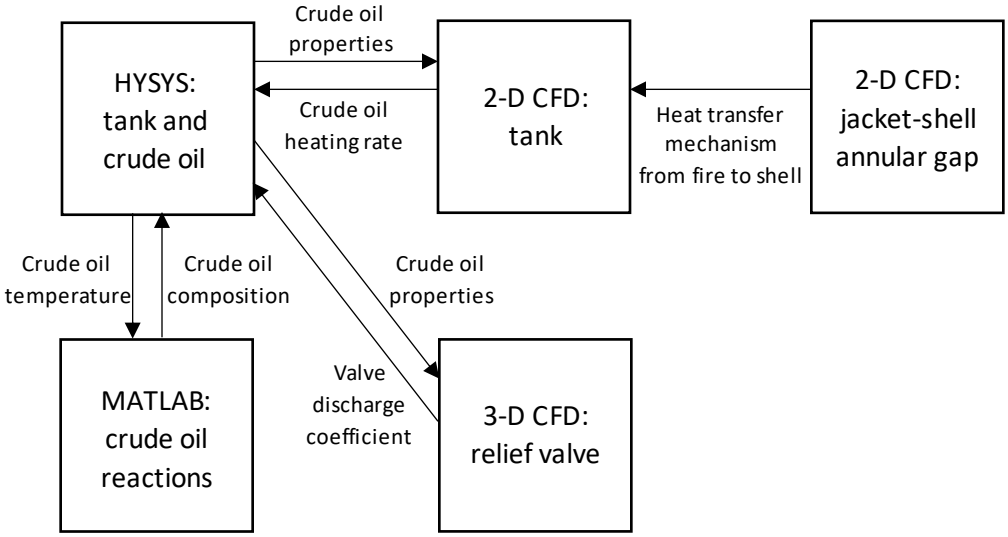

Figure 1.1: The combination of models used for this study and their interaction

Two modeling validation exercises were carried out to support different aspects of this modeling effort. First, crude oil equilibrium and thermal cracking experiments were conducted at CanmetENERGY-Ottawa, which were used to develop and verify physical and chemical behavior of crude oils. Second, combined CFD and HYSYS modeling was compared to data from a physical experiment conducted by the United States Department of Transportation – Federal Railroad Administration [5] to develop and verify the

modeling of heat transfer and to compare model predictions regarding pressure relief to observations from the experiment. This comparison to US DOT/FRA experiments is summarized in Appendix A.

2. Properties of Tank Car and Lading

In a typical tank car used for crude oil service, a steel shell containing the crude oil has a 3 mm-thick steel jacket surrounding it, with a 4-inch annular gap separating the two. Thermal protection is installed in the annulus between the shell and jacket. The 2-D CFD tank model will consider the extreme cases of a bare shell exposed directly to the fire and the addition of ½ inch-thick ceramic fiber blanket between the jacket and the shell. The heat transfer from the jacket across the annular air gap to the shell will be considered in the separate 2-D CFD model. The thermal conductivity of steel is at least two orders of magnitude greater than that of the thermal protection so its precise value is not important, and the jacket is not included in the CFD model layers. The dimensions and properties of the shell are provided in Table 2.1.

Table 2.1: Steel shell dimensions and properties

Inner diameter	117 ⅞ inch
Thickness	9/16 inch
Density	7854 kg/m^3
Heat capacity	434 J/(kg·K)
Thermal conductivity	60.5 W/(m·K)

The thermal conductivity of the ceramic fiber blanket is provided in Table 2.2, as well as the thermal conductivity of air for comparison. Also for comparison, note that the thermal conductivity of solid alumina-silica ceramic is approximately 2 W/(m·K) at 25°C, which is higher than that of air. The blanket reduces heat transfer *via* two mechanisms. The first is by blocking thermal radiation and the second is by suppressing convective motion of the air in the ceramic matrix. Consequently, the only heat transfer mode available through the air is conduction. The alternate heat transfer path is conduction through the solid ceramic. Comparing the density of solid alumina-silica ceramic (approximately 2450 kg/m^3) to that of the blanket (in this study, 72 kg/m^3), it is apparent that the blanket consists mostly of empty space (air) so the heat transfer path through the solid ceramic is minimal. In fact, it has been observed that the gas in which a blanket is immersed significantly affects its thermal conductivity [6]. Table 2.2 shows that the thermal conductivity of the blanket is close to that of air at lower temperatures. As the temperature rises, the thermal conductivity of the blanket rises faster than that of air, possibly because conduction through the solid ceramic increases in proportion to conduction through the air. Given the higher thermal conductivity of ceramic compared to air, the heat transfer resistance would likely reduce if the blanket were compressed or compacted over time. The model in this study uses the properties in Table 2.2. It assumes no flaws in the thermal protection and that the ceramic blanket has not degraded or compacted over time or by exposure to high temperatures.

Table 2.2: Thermal conductivity and specific heat capacity of the thermal protection as a function of temperature, adapted from [7]. The thermal conductivity of air is provided for comparison (from [8]). The density of the blanket is 72 kg/m^3.

	Blanket		Air
Temperature [°C]	Thermal Conductivity [W/(m·K)]	Specific Heat Capacity [J/(kg·K)]	Thermal Conductivity [W/(m·K)]
0.0	0.02982	788.0	0.024
100.0	0.04172	826.0	0.032
200.0	0.05362	862.0	0.038
300.0	0.06855	896.0	0.044
400.0	0.08647	928.0	0.050
500.0	0.10819	957.0	0.056
600.0	0.13375	984.0	0.061
700.0	0.16383	1010.0	0.066
800.0	0.19868	1033.0	0.071
900.0	0.23849	1053.0	0.076
1000.0	0.28395	1072.0	0.081
1100.0	0.33586	1088.0	0.086
1200.0	0.39499	1102.0	0.091

The specific heat capacity (heat capacity per unit mass) of air and the ceramic material are similar (1000 J/(kg·K)). Since the ceramic material represents most of the blanket's mass, it is responsible for most of its heat capacity. The more dense the blanket, the more heat it can absorb. The heat capacity of the blanket results in a modest transient effect, as it takes time for the blanket to heat-up from its initial temperature to its steady-state temperature distribution, upon exposure to the fire. This elapsed time was estimated by solving the transient heat conduction problem, where the blanket is initially at ambient temperature and is suddenly exposed to fire on one side. It was found that the thermal protection blanket takes approximately four minutes to reach its steady state temperature distribution, thus slightly delaying the lading heat-up, and that this elapsed time depends only on the dimensions and properties of the blanket.

A range of ladings was studied, from a condensate through light crude oil to a medium crude oil. They are summarized in Table 2.3. Note that although the medium sour crude has 1.35 times the density of the condensate, it has 31 times the viscosity. Although increasing viscosity generally accompanies increasing density, the variation in viscosity, which affects the oil's ability to flow, can be much more dramatic. There is also a major difference between the condensate and the crude oils in that the condensate has a low and narrow boiling/evaporation temperature range whereas the evaporation of crude oils occurs over a larger temperature range. The consequences of this will be explored in Section 8.1.

Table 2.3: List and comparison of the different ladings

Name	Crude Oil Type	Liquid density [kg/m³] at 300 K	Liquid viscosity [Pa·s] at 300 K
C1	Condensate	640	0.0003
L1	Light Crude	798	0.0018
LM1	Light Medium Crude	818	0.0046
LM2	Light Medium Crude	841	0.0051
MS1	Medium Sour Crude	862	0.0093

The tank was filled to 95% by volume unless otherwise specified. The head space above the lading initially contained air. As the crude oil was heated, the head space contained both air and the equilibrium crude oil vapour.

Initial fill level significantly affects the time to reach venting pressure. To illustrate, consider that for a 50% initial fill, a 3% increase in liquid volume (caused by its thermal expansion) causes a 3% reduction in the vapour space. On the other hand, for a 95% initial fill, a 3% increase in liquid volume causes a 57% reduction in the vapour space, and for a 97% initial fill, a 3% increase in liquid volume causes a 99.7% reduction in the vapour space, resulting in nearly an infinite pressure rise. Note that the heat transfer required to heat the 97%-full tank is not significantly different than that required to heat the 95%-full tank, but their pressure responses are profoundly different. Therefore, for high initial fill levels, small increases in fill level significantly decrease the time to pressurize the tank.

3. Overview of Heat Transfer

When modeling a rail tank car in a fire, the first quantity to consider is the temperature of and the heat generated by the fire. The adiabatic flame temperature for many fuels is around 1900°C. Open pool fires never come close to this temperature because the fire is very uncontrolled, meaning that there is an overabundance of fuel in some places (as evidenced by smoke) and an overabundance of air in others (both of which yield lower temperature), and there is no control of heat loss like in a refractory-lined furnace. National Research Council Canada measured [9] laboratory-scale pool fire temperatures of approximately 900°C as perceived by thermocouples on the exterior of the tank. The size of the fire affects the proportion of heat lost to heat released—the larger the fire, the smaller this proportion (because the ratio of exposed area to overall fire volume is lower), so very large fires could have higher temperatures. If we assume the fire to be opaque and perfectly emitting/absorbing, which becomes an increasingly better assumption the larger the fire, then the maximum heat flux from such a fire is given by the fourth power of fire temperature (in Kelvin) multiplied by the Stefan-Boltzmann constant ($5.67 \times 10^{-8}\ W/(m^2K^4)$). For 900°C (1173 K) this works out to approximately $100\ kW/m^2$, and for 1100°C (1373 K) it is approximately $200\ kW/m^2$. National Research Council Canada measured [9] laboratory-scale pool fire heat fluxes of approximately $100\ kW/m^2$, which corresponds to their 900°C temperature measurement. This is not necessarily the heat flux the tank absorbs because the tank surface heats up and radiates back to the fire. The radiant exchange between a fully engulfing, perfectly emitting fire and a convex tank can be described by

$$\dot{q} = \epsilon\, \sigma \left({T_f}^4 - {T_s}^4 \right) \tag{3.1}$$

where σ is the Stefan-Boltzmann constant, ϵ is the emissivity of the tank outside surface (jacket, shell, or thermal protection), T_f is the fire temperature (in Kelvin) and T_s is the outside surface temperature (in Kelvin). Therefore, the surface temperature of the tank depends on the radiant heat flux, $\dot{q}$ (and *vice versa*). For a given fire temperature, we may calculate the surface temperature of the tank for a range of heat fluxes. This is provided in Figure 3.1 for the surface emissivity of carbon steel ($\epsilon = 0.8$).

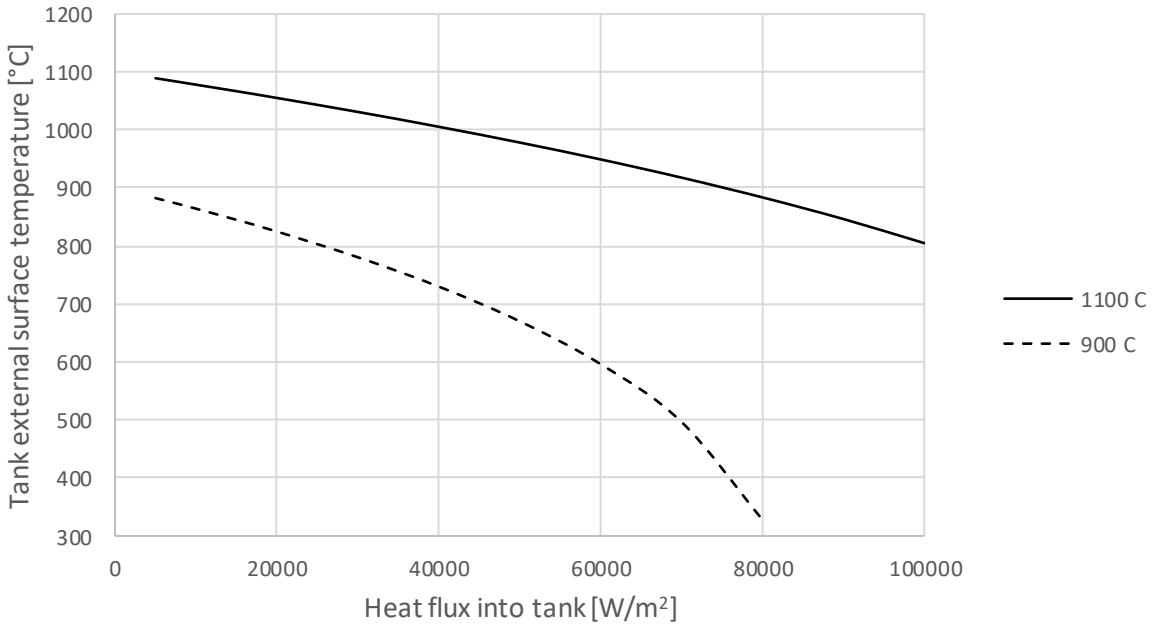

Figure 3.1: Tank outside surface temperature versus heat flux for surface emissivity, $\epsilon = 0.8$, and fire temperatures, 900°C (1173.15 K) and 1100°C (1373.15 K)

Figure 3.1 implies that the outside surface temperature, T_s, is close to that of the fire, T_f, when the heat flux is low, such as when there is ½-inch thermal protection (a simple conduction calculation shows that the heat flux is approximately 7,000 W/m^2). However, the behavior changes for bare-shell or poorly thermally protected tanks, which allow much higher heat fluxes into the tank. For example, in order for the heat flux to reach approximately 50,000 W/m^2, the outside surface temperature must drop to 670°C. This shows that the fire requires a significant difference in temperature between itself and the tank to transfer this level of heat. The liquid convection inside the tank provides the cooling of the tank shell that results in this temperature difference. For bare shell tanks, the overall heat flux rate is that which balances the flux from fire to tank with the flux from tank to lading. Therefore, there are two extreme cases. The first is that of the well-protected tank, in which the maximum heat flux reaches about 7,000 W/m^2, and is limited by conduction through the thermal protection. The second is that of the unprotected tank, in which the maximum heat flux is much higher, though below the 100,000 W/m^2 output by the fire, and is

determined by the balance between fire-to-tank (radiant transfer) and tank-to-lading (convective transfer). Another heat transfer path is from the steel shell into the headspace, where the shell is adjacent to gas/vapour, not liquid. Convective heat transfer is a relatively ineffective heat transfer mechanism involving gases. Thermal radiation dominates the heat transfer from the shell in this region of the tank. Finally, heat conduction through the steel shell is a potential path from higher temperature regions of the steel to lower temperature regions. The limiting factor for this mode, however, is that the steel shell provides little cross sectional area to transfer heat. Consequently, it is not expected to provide much relief for hot spots that develop on the shell, such as those adjacent to the gas space.

There are two transient effects related to the heat transfer. The main transient effect is that the convective motion of the liquid lading takes time to establish itself (and start transferring heat) from its initially stationary state. The other is that it takes time for the thermal protection to heat-up from its initial ambient temperature, as it has a finite heat capacity. As discussed in Section 2, it takes about four minutes for ½-inch-thick ceramic fiber blanket to reach its steady state temperature distribution.

In addition to unprotected shell and thermally-protected cases, the transfer of heat across the annulus between jacket and shell was investigated. This could represent a scenario where all thermal insulation had degraded, and only an annular air gap remained. Heat transfer across the annulus is examined in Appendix B, where the conductive and convective heat transfer across the annulus is found to be inconsequential. In a fire situation (i.e., when the jacket temperature is high), the overwhelming majority of heat crossing the annulus occurs by thermal radiation. Without thermal protection, the only phenomenon that curtails the radiant heat transfer is that the surfaces of the jacket and shell are not perfectly emitting. This implies that substantial thermal protection could be achieved by reducing the emissivity of the inside surface of the jacket and/or the outside surface of the shell. This thermal protection strategy is investigated in Appendix B.

4. Overview of Thermal Cracking Reactions

In previous phases of crude oil equation of state modeling work, experimental testing of three crudes (a medium crude (MBL), heavy synthetic (AHS), and dilbit (CDB)) was performed to determine (1) their initial lading properties at standard conditions and (2) their thermal cracking kinetics over a temperature range of 350 to 450°C. The complete initial lading properties data set, including density, viscosity, light-ends compositions, and simulated distillation curves, was achieved using a combination of in-house characterization and data provided by Transport Canada. These initial lading properties formed the basis for assay analysis in Aspen HYSYS (see Section 5), required for CFD, AFFTAC, and fire scenario modelling. Details pertaining to the thermal cracking kinetics can be found in a previous report entitled “Crude Oil Equation of State Modeling and Experimental Test Validation - Tasks 1 to 4 Year-end Progress Report” [10] and in the journal publication entitled “Five-Lump Mild Thermal Cracking Reaction Model Crude Oils and Bitumen with VLE Calculation.” [11]

The three crude oils were experimentally tested by heating samples up to 350, 400, 425, and 450°C at 1240 kPa. A five-lump reaction model, detailed in [11] and section 4.2, incorporated into the process simulator with vapour liquid equilibria (VLE) calculations was optimized to the experimental data obtained. The goodness of fit between the model predicted values and experimental values for the

medium crude (MBL), heavy synthetic (AHS), and dilbit (CDB) were determined to be 0.99, 0.99, and 0.98, respectively. Moreover, 80, 85, and 89% of the optimized model's predicted values had less than 10% error for the medium crude, heavy synthetic, and dilbit, respectively. It should be noted that, aside from the medium crude, the crude oils in this section are distinct from those in the CFD portion of the work. Test runs of the reactive model were performed, where the differences between models that use reactions or VLE alone and the combined VLE-reaction model were demonstrated. The combined model is assumed more accurate as the thermal cracking reactions occur mostly in the liquid phase of the system at mild thermal conditions (400-500°C). The system composition in the liquid and vapour phases were determined for a temperature ramp of 1°C/min and the phase properties of the system were calculated. The vapour mass fraction of the simulated system was of interest, as the entire system was predicted to be vapourized around 480°C. This exemplifies a worst-case scenario in which the entire volume of crude oil is vapourized due to system temperature increase (i.e., exposure to a fire).

4.1 Thermal Cracking and Lump Characterization

Thermal cracking is the endothermic (heat activated) cleavage of carbon-carbon bonds in hydrocarbons. In the case of a crude oil tank car exposed to a heat source, thermal cracking of the components of crude oil would be observed. Crude oil is made up of hundreds of different components that vary molecularly and provide different crude oil fractions with different bulk properties. The result is a large set of possible thermal cracking reactions.

Additionally, thermal cracking reactions have free-radical mechanisms, which can involve any of the oil's components and their activated radicals. This results in a complex system of reactions that cannot be efficiently modelled if all possible reactions are to be accounted. Discrete lumping involves the classification of crude oil components into groups; this approach simplifies the modeling procedure without compromising its efficacy. Discrete lumping involves grouping components of similar chemical and physical properties into a lumped pseudo-component that has average properties. Discrete lumps were used in the model developed and they were defined based on component normal boiling points (NBP), which mirrors characterization of crude oil in HYSYS. This makes the model-HYSYS integration possible (see Section 5). A five-lump model was used to represent the crude oil in the reactive model.

4.2 Reaction Network and Reaction Kinetics

The reaction network implemented in the reactive model was based on the reaction pathways proposed by Singh et al. [12] and is shown in Figure 4.2.1. The conversion pathways were defined with the assumption that each component lump can be converted to all other "lighter" (lower boiling point) lumps.

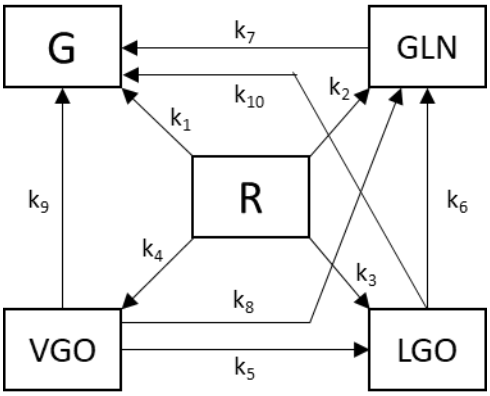

Figure 4.2.1: Five lump kinetic pathway proposed by Singh et al. [12].

The lumps shown in Figure 4.2.1 were used in the model to represent the crude oil in the rail cars. The assigned names and normal boiling point ranges of each lump are listed, where initial boiling point (IBP) is defined at 36°C:

G – Gas (C1-C5, <IBP)

GLN – Gasoline (IBP-150°C)

LGO – Light gas oil (150-350°C)

VGO – Vacuum gas oil (350-500°C)

R – Residue (500+°C)

Thermal cracking has been experimentally observed to have pseudo-first-order kinetics [13]. Each of the reaction pathways in the model above are represented as first-order kinetics. In the context of a tank car system, batch reactor equations were used to model the closed system. The system can be represented using the following mass balance equations:

$$(d[G])/dt=k_1[R] + k_7[GLN] + k_{10}[LGO] + k_9[VGO]$$

$$(d[GLN])/dt=k_2[R] + k_8[VGO] + k_6[LGO] - k_7[GLN]$$

$$(d[LGO])/dt=k_3[R] + k_5[VGO] - (k_6 + k_{10})[LGO]$$

$$(d[VGO])/dt=k_4[R] - (k_5 + k_8 + k_9)[VGO]$$

$$(d[R])/dt=-(k_1 + k_2 + k_3+k_4)[R]$$

where, [R], [VGO], [LGO], [GLN], and [G] are mass concentrations in units of wt% or $(kg_{lump})/(kg_{total})$ and k_n are the kinetic constants for each reaction pathway. Normally, the concentrations are based on volume (i.e., kg/m^3), but since the system is closed (prior to opening of the PRV) the mass is constant and it can be used to standardize each species' relative amount in the system.

5. AspenHYSYS and Matlab Models

Based on previous experience and expertise related to advanced process simulation within the fluidized bed conversion and gasification group at NRCan, CanmetENERGY – Ottawa, Aspen HYSYS was selected to perform the equation of state modeling for a variety of crude oil types. Aspen HYSYS, commonly referred to as just HYSYS, has built-in property packages that provide accurate thermodynamic, physical, and transport property predictions for hydrocarbons, non-hydrocarbons, petrochemical, and chemical fluids. The simulator uses experimental data to create a database of over 1500 components and over 16000 fitted binaries and has many types of built-in property packages, including:

- Equation of States (EOSs)
- Activity Models
- Vapour Pressure Models

For oil, gas, and petrochemical applications, the Peng-Robinson EOS is generally the recommended property package and was therefore selected for all process simulation work detailed in this report. The Peng-Robinson EOS is accurate for a variety of systems over a wide range of conditions, and rigorously solves most single phase, two phase, and three phase systems. This was verified *via* experimental test validation (see Section 4).

Aspen HYSYS contains a dynamic process utility to model the pressure letdown of a vessel, or in this case, the venting of a tank car. This dynamic 'depressuring utility' can be configured with various valve models and heat transfer scenarios. In this case, the system is modeled as a single vessel, which can contain a gas or gas-liquid mixture, and depressurization can take place through a single vapour valve, a single liquid valve, or both a vapour and liquid valve. The utility also allows heat loss to the environment to be modeled and includes special calculation methods for calculating the heat flux to the vessel from an external heat source. Some examples include fire mode, adiabatic mode and radiative mode.

5.1 HYSYS Crude Oil Characterization

Due to the nature of crude oils, determination of all the individual species and their respective mass fractions is very difficult by standard laboratory analytical characterization methods, especially for high carbon number species. Therefore, the petroleum characterization method in HYSYS converts the laboratory assay analyses of condensates, crude oils, petroleum cuts, and coal-tar liquids into a series of discrete hypothetical components based on normal boiling point cuts. These 'hypocomponents' provide the basis for the property package to predict the remaining thermodynamic and transport properties necessary for fluid modeling.

HYSYS produces a complete set of physical and critical properties for the crude oil hypocomponents with a minimal amount of information. However, the more information that can be supplied about the fluid, the more accurate these properties are, and the better HYSYS can predict the fluid's actual behaviour under varying conditions (e.g., elevated temperatures and pressures). HYSYS accepts five standard laboratory analytical assay procedures (Figure 5.1.1):

1) True boiling point distillation (TBP)

2) ASTM D86 and D1160 distillations (separately or combined)

3) ASTM D2887 simulated distillation

4) Equilibrium flash vapourization (EFV)

5) Chromatographic analysis

Other information that can be input into the assay model includes: molecular weight, mass density, Watson (UOP) K, viscosity, and light end hydrocarbon composition, all at standard conditions. It should be noted that parameters such as molecular weight, mass density, and viscosity can be input as a function of temperature (dependant curves), if such information is available.

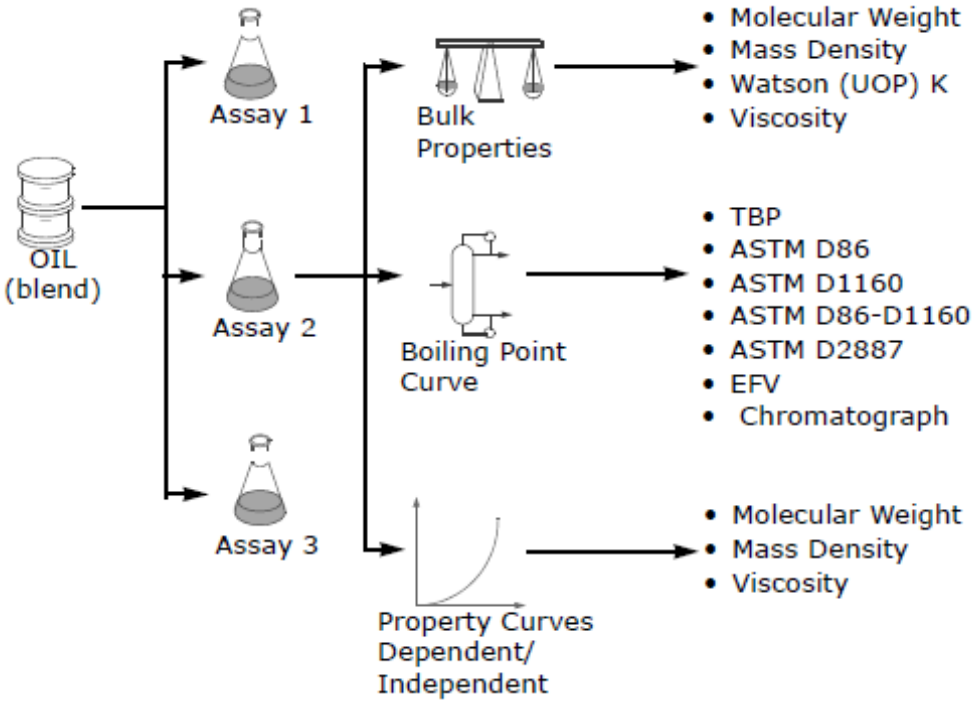

Figure 5.1.1: HYSYS oil characterization flow chart.

5.2 Dynamic Tank Car Modeling with and without Thermal Cracking Reactions

Figure 5.2.1 provides a detailed flowsheet outlining all the inputs, outputs, and activity pathways required for crude oil modeling under rail car fire conditions using HYSYS/UniSim process simulation software. It should be noted that UniSim was utilized in previous modeling work before switching to HYSYS; the activity pathways are identical in both circumstances. The modeling steps required when not considering thermal cracking reactions are as follows:

1) Selection of thermodynamic property package

2) Inputting of crude oil laboratory analytical data into oil characterization method

3) HYSYS crude oil characterization; creation of defined hypocomponents; adjustment to crude oil characterization (if necessary)

4) Selection of dynamic modeling boundary conditions

5) Dynamic modeling
6) Data generation and analysis; includes plots of time versus temperature, pressure, fill level, composition, etc.
7) Review of selected thermodynamics property package suitability

To realistically predict the physical behaviour of crude oil in a rail car, possible reactions must be considered. Under conditions of heat exposure through fire, thermal cracking reactions are likely to occur, and these were added to the dynamic model. The following steps were conducted in the process of implementing reactions:

1) Reaction model selection from literature
2) Lumped crude oil characterization definition
3) Kinetic parameters determined from experimental testing
4) Creation of a combined VLE and reaction model
5) Dynamic modeling using combined VLE and reaction model
6) Data generation and analysis; includes plots of time versus temperature, pressure, fill level, composition, etc.
7) Review of selected thermodynamics property package suitability

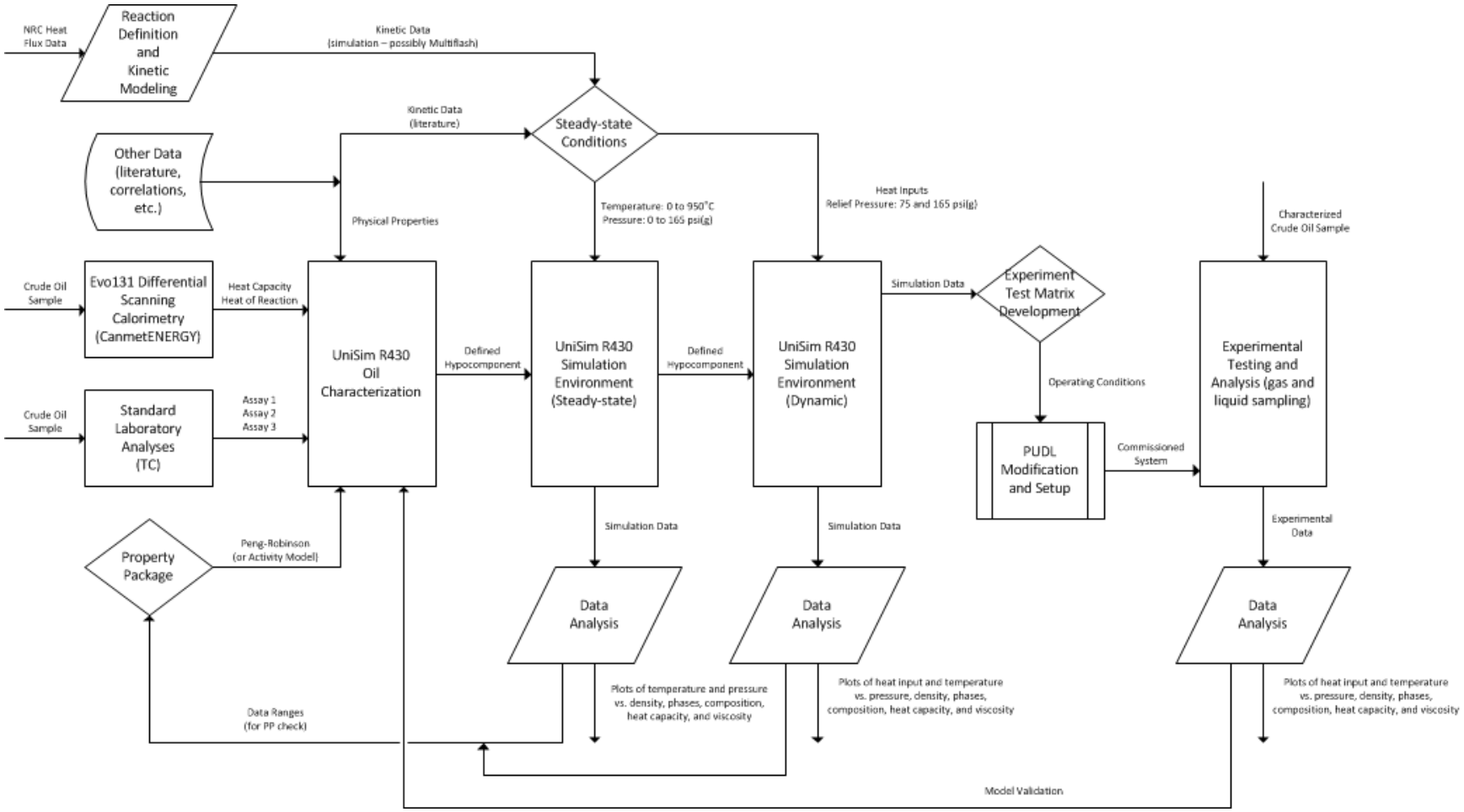

Figure 5.2.1: Crude oil EOS modeling - Overall approach.

As it was expected that continuous venting would be the most likely scenario during fire conditions, a fully dynamic model was developed. Figure 5.2.2 shows a screenshot of the process flow diagram utilized for this model. The characterized crude oil (labelled as Feed1 in this case), is used to initialize the conditions within the tank car (Vessel). These initial conditions include temperature, pressure, and composition (see Section 5.1).

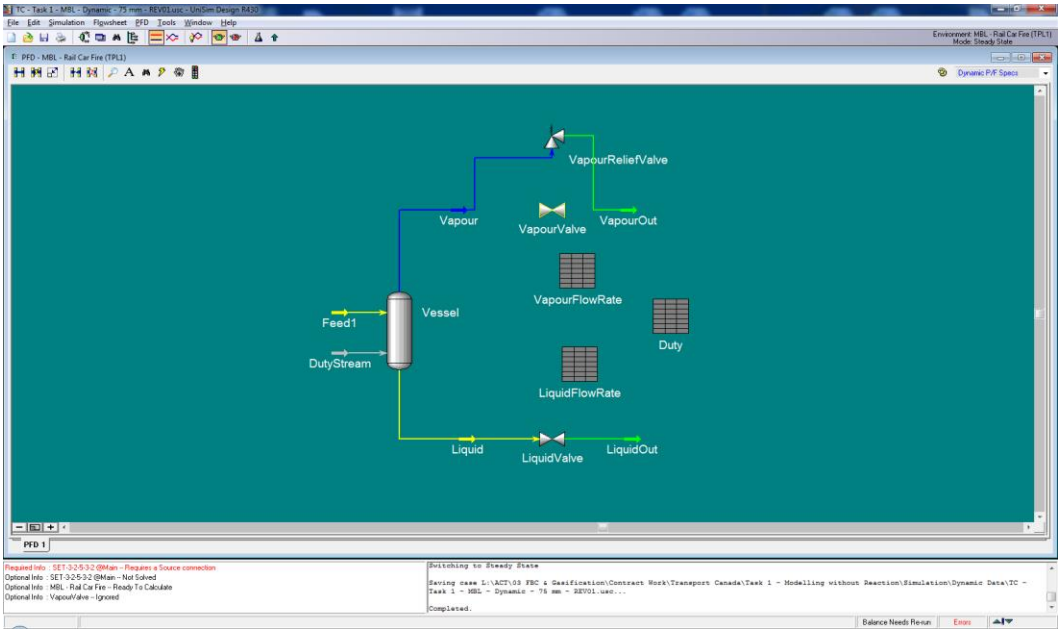

Figure 5.2.2: Process flow diagram for dynamic crude oil modeling.

Detailed rail car geometry can be inputted into the model to ensure the total initial crude oil volume is as similar as possible to an actual tank car transporting crude oil. A screenshot of the tank car geometry interface can be seen in Figure 5.2.3. Several key variables can be inputted into the tank car model including orientation (either horizontal or vertical), diameter, length (or height), and initial liquid percentage or volume.

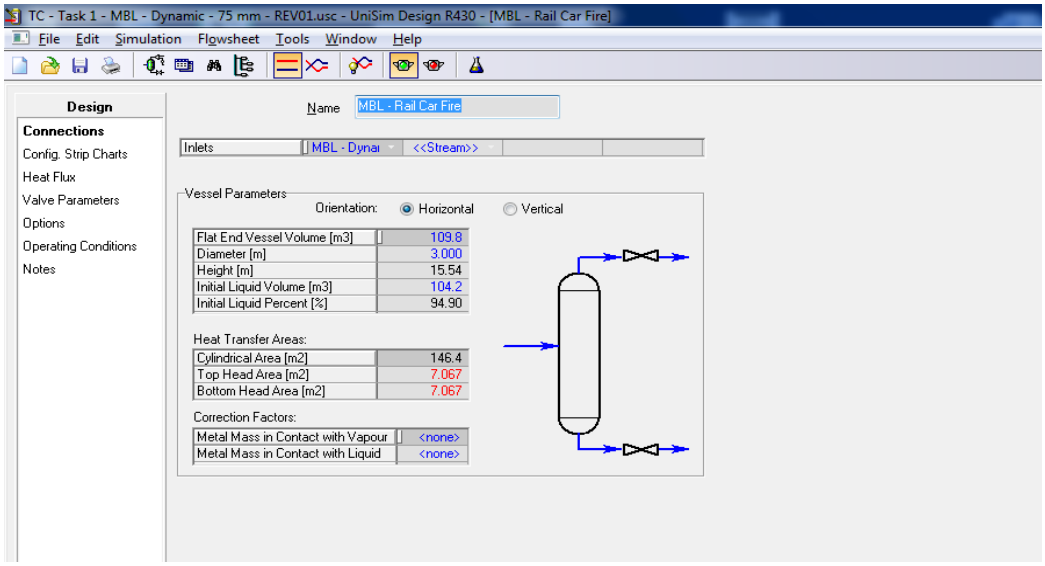

Figure 5.2.3: Tank car geometry interface for dynamic crude oil modeling.

To model tank cars under fire conditions, the primary objective of this work, information about the rate of heat transfer to the vessel is required. Once this is known, there are a variety of heat flux modes that can be modelled in HYSYS. As mentioned above, some examples include fire mode, adiabatic mode, and radiative mode. For the work contained in this report, the most critical heat flux modes utilized were fire and radiative. For fire mode (Figure 5.2.4), heat transfer to the lading is direct (kJ/h) and can be approximated *via* several different methods such as constant, time based, temperature based, liquid volume percentage based, and any combination of the latter. Radiative mode uses more detailed information about the fire and the tank car to calculate the heat flux to the lading. This includes flame and ambient temperature, flame and tank car emissivities, and tank car metal and insulation properties (i.e., thickness, heat capacity, density, and conductivity).

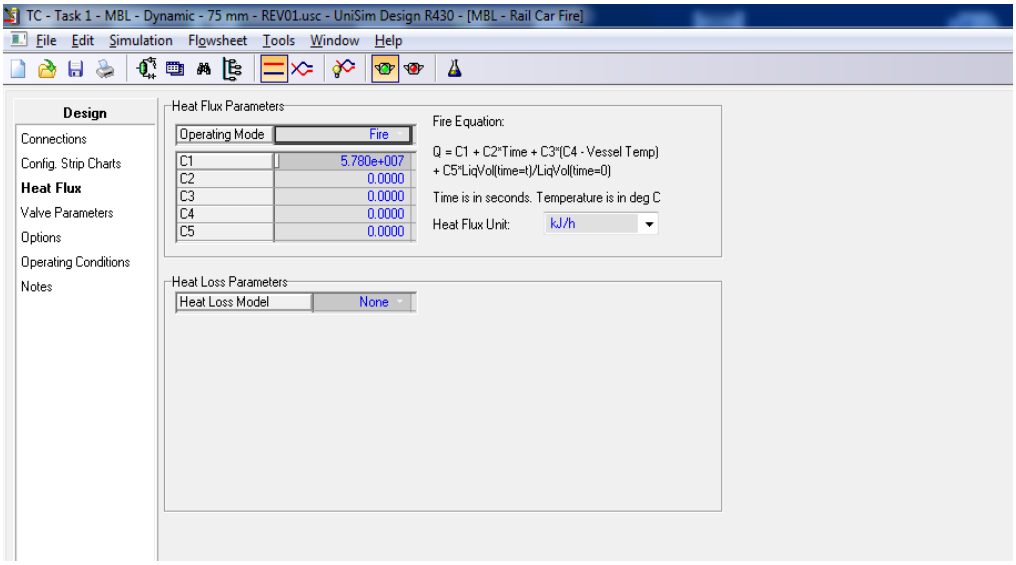

Figure 5.2.4: Tank car heat flux interface for dynamic crude oil modeling.

The tank car model is designed to allow for venting of contents through a pressure relief valve (PRV) (see Figure 5.2.2). Depending on the relative position of the PRV either vapour or liquid can be vented from the system at any given time and it generally depends on the liquid level. The position of the PRV can be adjusted to simulate various 'rollover' events ranging from a 0 degree position (perfectly upright, standard position) to a 180 degree position (upside down). Several key parameters are required to fully model a given PRV (Figure 5.2.5). These parameters include orifice area or diameter, discharge coefficient, set pressure, and full open pressure, where each of these parameter are determined *via* CFD PRV modeling (see Section 7). The determination of the discharge coefficient with liquid flow through PRV is also provided using CFD modeling, as the PRV performance is dramatically different under liquid conditions. It should be noted that the PRV can be artificially blocked to simulate scenarios where a given PRV has been damaged or restricted by the accumulation of carbon/coke *via* thermal cracking on the lading. In these cases the orifice area is proportionally reduced by the percentage of blockage (e.g., 50% blockage equates to 50% reduction in total orifice area). This approach to represent blockage differs slightly compared to the CFD approach (refer to Section 8.4 for a detailed analysis).

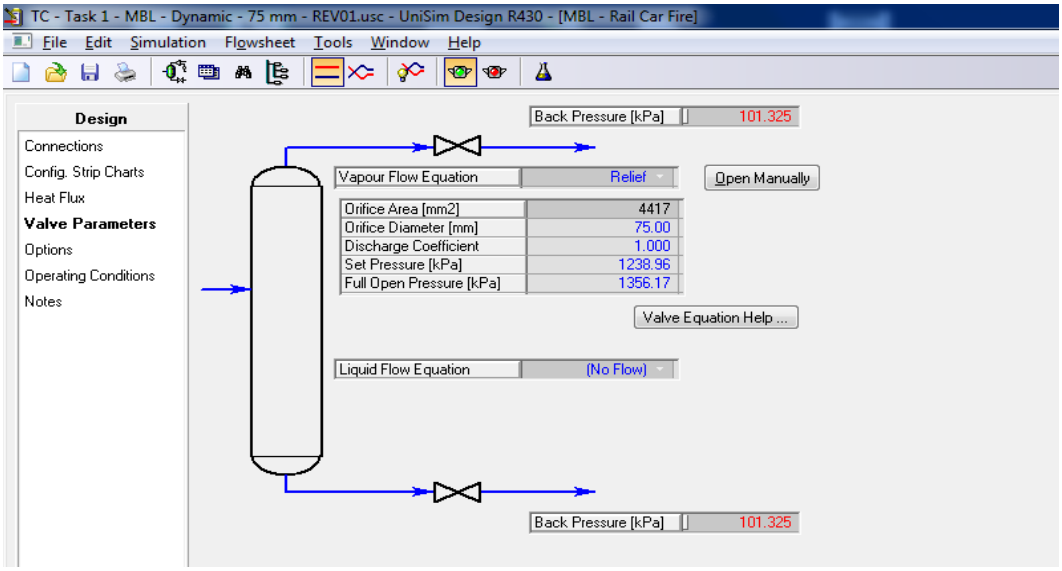

Figure 5.2.5: Tank car PRV parameters interface for dynamic crude oil modeling.

5.3 Combined VLE and Reaction Model

The objective of the combined vapour-liquid equilibria (VLE)-reaction model is to more accurately model the crude oil system when thermal cracking reactions are expected to occur. The VLE component allows for the tank car model to determine the proportion of the system found in the liquid phase, determine its composition, and apply the thermal cracking reactions that occur in the liquid phase. Using Matlab code, the combined model takes initial (or current) system conditions and parameter inputs to determine how to change the system conditions over time. The model inputs include temperature, temperature increment with time, pressure, and pressure increment with time. During the solution of the combined VLE-reaction model, it iterates through steps in time (typically 1 minute steps). In each step, the following set of tasks are accomplished using the Matlab code:

1) Access the HYSYS file to define/update the thermodynamic state (temperature and pressure) of the crude assay
2) Extract the chemical composition (component mass fractions) of the crude assay in both the vapour and liquid phases
3) Convert the liquid phase mass composition of the assay to liquid lump mass concentrations
4) Use the reaction mass balances to the calculated new liquid lump mass concentrations
5) Determine percentage change in lump mass concentration and update the HYSYS assay composition based on this percentage mass change
6) Extract the calculated physical properties of the system from HYSYS at the defined state (temperature, pressure, and new composition) in both the vapour and liquid phases

The reaction model coded in Matlab uses component object model (COM) connections to automate commands in HYSYS from the Matlab program. Matlab is a computing environment developed by Mathworks that allows for custom program development. Programs can use Matlab's numerous utilities and toolboxes to perform complex tasks and algorithms.

The reaction mass balances modeled in Matlab complement the HYSYS process shown in Figure 5.3.1. Since the reactions are assumed to only occur in the liquid phase (see Section 4), the VLE separates the vapour and liquid phases and allows Matlab to use the liquid composition for the solution of the reaction network. The dashed lines in Figure 5.3.2 represent the MATLAB connection with the HYSYS system from Figure 5.3.1.

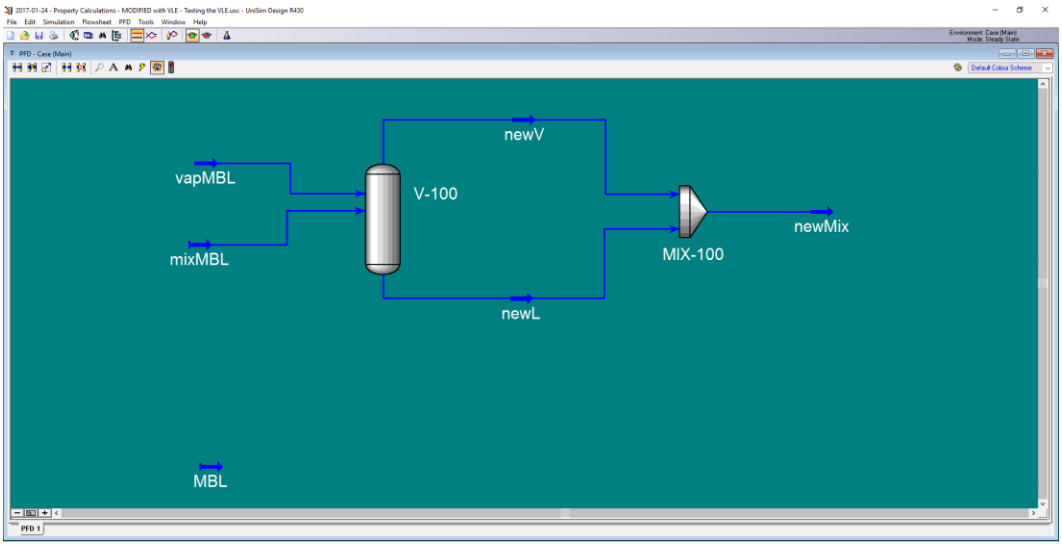

Figure 5.3.1: Example HYSYS process model used in reactive modeling.

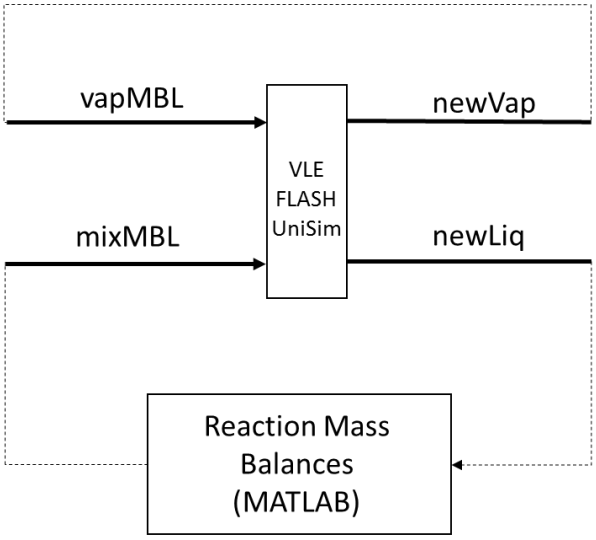

Figure 5.3.2: Representation of the connection between Matlab and HYSYS in the combined VLE-reaction model – Example for MBL crude oil.

The lumps presented in Section 4 have wide temperature range definition (up to 200°C wide), while the HYSYS assay 'hypocomponents' are defined by more narrow 10-20°C intervals. The use of discrete lump kinetics has the unfavourable attribute of forcing both the composition and physical properties to averaged values. To prevent the loss of information by setting the composition of the components of the HYSYS assay to an average mass fraction value, each composition is updated based on the calculated percentage mass change of each lump. This ensures that each component in the HYSYS assay (in a given lump) changes in mass composition by the same relative amount as the reaction mass balances predict. Table 5.3.1 lists the hypocomponents used in HYSYS and how they are grouped into lumps based on boiling point.

Table 5.3.1: Aspen HYSYS component list and associated lump definition – IBP stands for initial boiling point defined as 36°C.

Lump Name	Lump Abbreviation	Boiling point definition
Gas	G	<IBP
Gasoline	GLN	IBP-150°C
Light Gas Oil	LGO	150-350°C
Vacuum Gas Oil	VGO	350-500°C
Residue	R	>500°C

5.4 Thermal Cracking Performance Modeling

The objective of the thermal cracking performance modeling work is to compare results of modeling with and without reactions for different crude oil types (namely MBL, AHS, and CDB) at elevated temperatures to determine if a discernable difference is present for those crude oil types,. If differences are found, this

would require incorporation of a reactive model for future fire scenario modeling work. In contrast to previous thermal cracking performance modeling, the combined VLE-reaction model is integrated with the tank car model developed in HYSYS process simulation software (see Section 5.3 for details).

The specifications for these runs were established by Transport Canada for a potential tank car fire scenario. The initial goal was to set up the HYSYS tank car model with a 95% initial fill, 900°C fire temperature, and a fully engulfing fire (i.e., even heat flux around the circumference of the tank car). At the time these runs were performed, heat transfer versus time profiles were not available, so instead a constant heat flux of 100 kW/m^2 was used for all runs regardless of crude oil type or tank car geometry. Although this does not necessarily represent a true tank car fire scenario, it does allow for meaningful comparisons between cases with and without thermal cracking and the assessment of relative differences between crude oil types. Along with the specifications noted above, Tables 5.4.1 to 5.4.3 summarize all relevant inputs to the tank car model used for this phase of work (see Section 5.2 for details on tank car model inputs). Some important considerations/assumptions include:

1) Thermal cracking reactions only take place in the liquid phase as defined in Section 4
2) Tank car geometry is based on previous information provided by Transport Canada and does not exactly match any specific particular tank car used in the field
3) Constant heat flux to lading from external source (e.g., fire)
4) Valve geometry and discharge coefficient are determined *via* CFD modeling (see Section 7)
5) Full open pressure is ~10% higher than set pressure for the PRV
6) All fluid discharge is through top mounted vapour PRV (0 degree position)
7) 100% recycle efficiency (i.e., liquid and vapour contents are always in equilibrium)
8) Negligible hydrostatic pressure
9) Contents relieve to atmospheric pressure (101.325 kPa)
10) Initial tank car pressure is 150 kPa – although this is unlikely to be the case it does not impact the comparative results
11) 75% initial fill (to be discussed in further detail in Section 8.2)
12) No air in vapour headspace, only light-ends
13) Bare tank (i.e., no insulation or thermal protection)

Table 5.4.1: Tank car specifications for thermal cracking performance modeling – Connections and geometry.

Run #	Notes	Crude Name	Crude Type	Reactions	Connections													
					Orientation	Flat End Vessel Volume	Inner Diameter	Thickness		Outer Diameter	Height / Length	Initial Liquid Volume	Initial Liquid Percent	Cylindrical Area	Head Area	Total Area	Max Crude Loading	Standard Liquid Density
						(m3)	(m)	(m)	(in)	(m)	(m)	(m3)	(%)	(m2)	(m2)	(m2)	(kg)	(kg/m3)
R1	-	MBL	Medium Sour	Yes	Horizontal	109.8	3.000	N/A	N/A	N/A	15.53	82.35	75	146.4	14.138	160.54	N/A	869.30
R2	-			No														869.30
R3	-	AHS	Heavy Synthetic	Yes														959.80
R4	-			No														959.80
R5	-	CDB	Dilbit Blend	Yes														954.65
R6	-			No														954.65

Table 5.4.2: Tank car specifications for thermal cracking performance modeling – Heat transfer and valve parameters.

Run #	Notes	Crude Name	Crude Type	Reactions	Heat Transfer						Valve Parameters										
					Applied Duty					Heat Transfer Model	Orifice Area	Orifice Diameter		Discharge Coefficient	Set Pressure		Full Open Pressure		Back Pressure	Vapour Flow	Liquid Flow
					C1 (kJ/h)	C2	C3	C4	C5	(-)	(mm2)	(mm)	(in)	(-)	(kPa)	(psig)	(kPa)	(psig)	(kPa)	(-)	(-)
R1	-	MBL	Medium Sour	Yes	57800000	0	0	0	0	None	5562	84.15	3.312994	0.72	1239	165	1356	182	101	Yes	No
R2	-			No																	
R3	-	AHS	Heavy Synthetic	Yes																	
R4	-			No																	
R5	-	CDB	Dilbit Blend	Yes																	
R6	-			No																	

Table 5.4.3: Tank car specifications for thermal cracking performance modeling – Options and operating conditions.

Run #	Notes	Crude Name	Crude Type	Reactions	Options		Operating Conditions				
					PV Work	Recycle Efficiency	Time Step	Depressurizing Time Step	Total Depressurizing Time	Initial Temperature	Initial Pressure
					(%)	(%)	(s)	(s)	(min)	(oC)	(kPa)
R1	-	MBL	Medium Sour	Yes	93	100	0.1	20	100	25	150
R2	-			No							
R3	-	AHS	Heavy Synthetic	Yes							
R4	-			No							
R5	-	CDB	Dilbit Blend	Yes							
R6	-			No							

5.5 Fire Scenario Performance Modeling

The objective of this portion of the work is to combine CFD modeling results related to heat transfer and PRV performance with the tank car VLE-reaction model to determine tank car performance under fire scenarios. In contrast to the work described above and in previous reports, the updated HYSYS tank car model uses crude oil specific heat flux versus time data and radiative heat transfer parameters, and CFD-generated discharge coefficients for the PRV. The specifications for cases were set out by Transport Canada for a series of potential tank car fire scenarios, with the ultimate goal of better understanding the significance of several key variables such as crude oil type, volatility, and PRV performance. In addition to these variables, a series of calibration runs were required to ensure the HYSYS tank car model outputs were in alignment with those generated *via* CFD. This will be discussed in further detail in Section 8.5 of the report.

Figure 5.5.1 shows the general arrangement of the horizontally-oriented tank car used in this modeling work, which is loosely based on TC-117 specifications. The values for A, B, and C are 55'-3/4", 49'-7/8", and 10', respectively. The tank car is made of TC128-B (metal) with a vessel thickness of 9/16" and a maximum gross rail load of 88850 kg. It should be noted that, since the tank car model has not been designed to accommodate hemi-spherical ends, a small adjustment was made to the tank car geometry, where the total vessel volume is maintained (115.60 m^3) assuming flat ends.

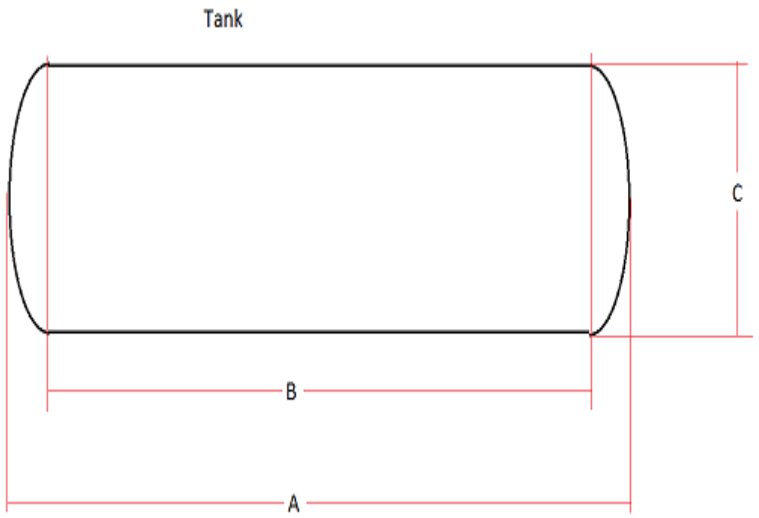

Figure 5.5.1: Transport Canada supplied tank car geometry

Based on previous work, it was expected that crude oil type and volatility would play a significant role in tank car performance and for this reason runs using light (baseline), medium, heavy, condensate, and dilbit oil samples have been explored. The impact of initial crude oil light-ends was assessed by manipulating the composition of a light crude oil to replicate three potential cases: (1) a sample that has off-gassed at atmospheric conditions, (2) a sample with all C1 to C5 removed, and (3) a sample that is spiked with additional C1 to C5. A comparison is made to a case where reactions are not considered. The baseline case considers the use of thermal protection (Fyrewrap® – 0.5", 0.035 to 0.238 W/m·K conductivity from 25 to 900°C) with a comparison to a case without any level of protection (bare shell). The impact of the PRV on overall performance was expected to be important, so multiple cases

considering level of blockage (0, 50, 80, 99.8, and 100%), tank orientation (45 and 120 degrees), and set pressure (75 and 165 psig) were modeled. Fill levels lower than the maximum allowable based on total mass were also considered (80 and 87.5%). When exploring the use of the radiative heat transfer boundary conditions, fire temperatures (815.6, 900, 950, and 1204.4°C) and tank emissivities (0.80, 0.90, 0.92, and 1.00) were varied. Finally, as a part of initial calibration to CFD results, recycle efficiencies lower than 100% were assessed. Along with the specifications noted above, Tables 5.5.1 to 5.5.3 summarize all relevant inputs to the tank car model used for this phase of work (see Section 5.2 for details on tank car model inputs). Some important considerations/assumptions include:

1) Thermal cracking reactions only take place in the liquid phase as defined in Section 4
2) Heat flux versus time data was provided by CFD modeling (see Section 6) in cases where radiative is not used
3) Valve geometry and discharge coefficient was provided by CFD modeling (see Section 7)
4) Full open pressure is ~10% higher than set pressure
5) Negligible hydrostatic pressure
6) Contents relieve to atmospheric pressure (101.325 kPa)
7) Initial tank car pressure is 105 kPa
8) Unless otherwise specified, fill level calculated to maximize crude oil lading without exceeding gross rail load of 88850 kg
9) Unless otherwise specified, vapour head space is assumed to be air (as in normal filling of a tank car)
10) Jacket thickness and resistance to heat transfer excluded
11) Initial lading temperature is 46.1°C
12) Low recycle efficiency used in all cases (initial calibration excluded)

Table 5.5.1: Tank car specifications for fire scenario performance modeling – Connections and geometry.

Run #	Notes	Crude Name	Crude Type	Reactions	Connections												
					Orientation	Flat End Vessel Volume	Inner Diameter	Thickness		Outer Diameter	Height / Length	Initial Liquid Volume	Initial Liquid Percent	Cylindrical Area	Head Area	Total Area	Max Crude Loading	Liquid Bulk Density (at initial condition)
						(m3)	(m)	(m)	(in)	(m)	(m)	(m3)	(%)	(m2)	(m2)	(m2)	(kg)	(kg/m3)
E1	Baseline - Light crude, filled to max weight limit, Fyrewrap, 75/85 psig, CFD fire, 815.6oC	FL178	Light	Yes								107.00	92.56					830.4
E2	Medium Crude	MBL	Medium Crude	Yes								99.96	86.47					888.9
E3	Heavy Crude	AHS	Heavy Synthetic	Yes								94.94	82.12					935.9
E4	Condensate	FL126	Condensate	Yes								109.82	95.00					689.1
E5	Dilbit	CDB	Dilbit Blend	Yes								94.07	81.38					944.5
E6	Without Reactions	FL178	Light	No								107.00	92.56					944.5
E7	Light crude, 45 degrees	FL178	Light	Yes								107.00	92.56					830.4
E8	Light crude, 120 degrees	FL178	Light	Yes								107.00	92.56					830.4
E9	PRV Blockage 50%	FL178	Light	Yes								107.00	92.56					830.4
E10	PRV Blockage 80%	FL178	Light	Yes								107.00	92.56					830.4
E10B	PRV Blockage 99.8%	FL178	Light	Yes								107.00	92.56					830.4
E11	PRV Blockage 100%	FL178	Light	Yes								107.00	92.56					830.4
E12	Bareshell	FL178	Light	Yes								107.00	92.56					830.4
E13	High C1-C5	FL178	Light	Yes								109.29	94.54					*813.0*
E14	Zero C1-C5	FL178	Light	Yes								107.15	92.69					*829.2*
E15	Off-gased/Dead	FL178	Light	Yes								106.98	92.55					*830.5*
E16	Fire temperature (900oC), tank emissivity (0.90)	FL178	Light	Yes	Horizontal	115.6	3.019	0.0143	0.5625	3.048	16.14	107.00	92.56	153.14	14.321	167.46	88850	830.4
E17	Fire temperature (950oC), tank emissivity (0.90)	FL178	Light	Yes								107.00	92.56					830.4
E18X	Fire temperature (815.6oC), tank emissivity (0.90)	FL178	Light	Yes								107.00	92.56					830.4
E18	Fire temperature (1000oC), tank emissivity (0.90)	FL178	Light	Yes								107.00	92.56					830.4
E19	Fire temperature (1204.4oC), tank emissivity (0.90)	FL178	Light	Yes								107.00	92.56					830.4
E20	Fire temperature (815.6oC), tank emissivity (0.92)	FL178	Light	Yes								107.00	92.56					830.4
E21	Fire temperature (815.6oC), tank emissivity (0.80)	FL178	Light	Yes								107.00	92.56					830.4
E22	Fire temperature (815.6oC), tank emissivity (1.00)	FL178	Light	Yes								107.00	92.56					830.4
E23	PRV set pressure 165 psig	FL178	Light	Yes								107.00	92.56					830.4
E24	Fill level 87.5%	FL178	Light	Yes								101.15	87.50					830.4
E25	Fill level 80%	FL178	Light	Yes								92.48	80.00					830.4

Table 5.5.2: Tank car specifications for fire scenario performance modeling – Heat transfer and valve parameters.

Run #	Notes	Crude Name	Crude Type	Reactions	Heat Transfer						Valve Parameters															
					Applied Duty					Heat Transfer Model	Orifice Area	Orifice Diameter		Discharge Coefficient	Set Pressure		Full Open Pressure		Back Pressure	Air Flowrate at Full Open Pressure		Water Flowrate at Full Open Pressure		Designed for Vapour Flow	Designed for Liquid Flow
					C1 (kJ/h)	C2	C3	C4	C5	(-)	(mm2)	(mm)	(in)	(-)	(kPa)	(psig)	(kPa)	(psig)	(kPa)	(Sm3/h)	(SCFM)	(Sm3/h)	(SCFM)	(-)	(-)
E1	Baseline - Light crude, filled to max weight limit, Fyrewrap, 75/85 psig, CFD fire, 815.6oC	FL178	Light	Yes	3014326					Detailed	13314	130.2	5.126	0.828	618	75	687	85	101	52480	30888	1347	793	Yes	No
E2	Medium Crude	MBL	Medium Crude	Yes	Radiation Model						13314	130.2	5.126	0.828	618	75	687	85	101	52480	30888	1347	793	Yes	No
E3	Heavy Crude	AHS	Heavy Synthetic	Yes	3014326						13314	130.2	5.126	0.828	618	75	687	85	101	52480	30888	1347	793	Yes	No
E4	Condensate	FL126	Condensate	Yes	3014326						13314	130.2	5.126	0.828	618	75	687	85	101	52480	30888	1347	793	Yes	No
E5	Dilbit	CDB	Dilbit Blend	Yes	3014326						13314	130.2	5.126	0.828	618	75	687	85	101	52480	30888	1347	793	Yes	No
E6	Without Reactions	FL178	Light	No	Radiation Model						13314	130.2	5.126	0.828	618	75	687	85	101	52480	30888	1347	793	Yes	No
E7	Light crude, 45 degrees	FL178	Light	Yes	3014326						13314	130.2	5.126	0.610	618	75	687	85	101	38666	22758	990	583	No	Yes
E8	Light crude, 120 degrees	FL178	Light	Yes	3014326						13314	130.2	5.126	0.610	618	75	687	85	101	38666	22758	990	583	No	Yes
E9	PRV Blockage 50%	FL178	Light	Yes	3014326						6657	92.07	3.625	0.828	618	75	687	85	101	26084	15352	673	396	Yes	No
E10	PRV Blockage 80%	FL178	Light	Yes	3014326						2663	58.23	2.292	0.828	618	75	687	85	101	10434	6141	269	158	Yes	No
E10B	PRV Blockage 99.8%	FL178	Light	Yes	3014326						20	5.00	0.197	0.828	618	75	687	85	101	0	0	0	0	Yes	No
E11	PRV Blockage 100%	FL178	Light	Yes	3014326						0	0	0	0.828	618	75	687	85	101	0	0	0	0	Yes	No
E12	Bareshell	FL178	Light	Yes	Radiation Model						13314	130.2	5.126	0.828	618	75	687	85	101	52480	30888	1347	793	Yes	No
E13	High C1-C5	FL178	Light	Yes	Radiation Model						13314	130.2	5.126	0.828	618	75	687	85	101	10434	6141	269	158	Yes	No
E14	Zero C1-C5	FL178	Light	Yes	Radiation Model						13314	130.2	5.126	0.828	618	75	687	85	101	52480	30888	1347	793	Yes	No
E15	Off-gased/Dead	FL178	Light	Yes	Radiation Model						13314	130.2	5.126	0.828	618	75	687	85	101	52480	30888	1347	793	Yes	No
E16	Fire temperature (900oC), tank emissivity (0.90)	FL178	Light	Yes	Radiation Model						13314	130.2	5.126	0.828	618	75	687	85	101	52480	30888	1347	793	Yes	No
E17	Fire temperature (950oC), tank emissivity (0.90)	FL178	Light	Yes	Radiation Model						13314	130.2	5.126	0.828	618	75	687	85	101	52480	30888	1347	793	Yes	No
E18X	Fire temperature (815.6oC), tank emissivity (0.90)	FL178	Light	Yes	Radiation Model						13314	130.2	5.126	0.828	618	75	687	85	101	52480	30888	1347	793	Yes	No
E18	Fire temperature (1000oC), tank emissivity (0.90)	FL178	Light	Yes	Radiation Model						13314	130.2	5.126	0.828	618	75	687	85	101	52480	30888	1347	793	Yes	No
E19	Fire temperature (1204.4oC), tank emissivity (0.90)	FL178	Light	Yes	Radiation Model						13314	130.2	5.126	0.828	618	75	687	85	101	52480	30888	1347	793	Yes	No
E20	Fire temperature (815.6oC), tank emissivity (0.92)	FL178	Light	Yes	Radiation Model						13314	130.2	5.126	0.828	618	75	687	85	101	52480	30888	1347	793	Yes	No
E21	Fire temperature (815.6oC), tank emissivity (0.80)	FL178	Light	Yes	Radiation Model						13314	130.2	5.126	0.828	618	75	687	85	101	52480	30888	1347	793	Yes	No
E22	Fire temperature (815.6oC), tank emissivity (1.00)	FL178	Light	Yes	Radiation Model						13314	130.2	5.126	0.828	618	75	687	85	101	52480	30888	1347	793	Yes	No
E23	PRV set pressure 165 psig	FL178	Light	Yes	Radiation Model						13314	130.2	5.126	0.828	1239	165	1356	182	101	104048	61239	1982	1166	Yes	No
E24	Fill level 87.5%	FL178	Light	Yes	Radiation Model						13314	130.2	5.126	0.828	618	75	687	85	101	52480	30888	1347	793	Yes	No
E25	Fill level 80%	FL178	Light	Yes	Radiation Model						13314	130.2	5.126	0.828	618	75	687	85	101	52480	30888	1347	793	Yes	No

Table 5.5.3: Tank car specifications for fire scenario performance modeling – Options and operating conditions.

Run #	Notes	Crude Name	Crude Type	Reactions	Operating Conditions				
					Time Step	Depressurizing Time Step	Total Depressurizing Time	Initial Temperature	Initial Pressure
					(s)	(s)	(min)	(oC)	(kPa)
E1	Baseline - Light crude, filled to max weight limit, Fyrewrap, 75/85 psig, CFD fire, 815.6oC	FL178	Light	Yes		43200	720		
E2	Medium Crude	MBL	Medium Crude	Yes		43200	720		
E3	Heavy Crude	AHS	Heavy Synthetic	Yes		43200	720		
E4	Condensate	FL126	Condensate	Yes		43200	720		
E5	Dilbit	CDB	Dilbit Blend	Yes		43200	720		
E6	Without Reactions	FL178	Light	No		86400	1440		
E7	Light crude, 45 degrees	FL178	Light	Yes		86400	1440		
E8	Light crude, 120 degrees	FL178	Light	Yes		43200	720		
E9	PRV Blockage 50%	FL178	Light	Yes		43200	720		
E10	PRV Blockage 80%	FL178	Light	Yes		43200	720		
E10B	PRV Blockage 99.8%	FL178	Light	Yes		43200	720		
E11	PRV Blockage 100%	FL178	Light	Yes		43200	720		
E12	Bareshell	FL178	Light	Yes		43200	720		
E13	High C1-C5	FL178	Light	Yes		43200	720		
E14	Zero C1-C5	FL178	Light	Yes		43200	720		
E15	Off-gased/Dead	FL178	Light	Yes		43200	720		
E16	Fire temperature (900oC), tank emissivity (0.90)	FL178	Light	Yes	0.1	43200	720	46.1	105
E17	Fire temperature (950oC), tank emissivity (0.90)	FL178	Light	Yes		43200	720		
E18X	Fire temperature (815.6oC), tank emissivity (0.90)	FL178	Light	Yes		43200	720		
E18	Fire temperature (1000oC), tank emissivity (0.90)	FL178	Light	Yes		43200	720		
E19	Fire temperature (1204.4oC), tank emissivity (0.90)	FL178	Light	Yes		43200	720		
E20	Fire temperature (815.6oC), tank emissivity (0.92)	FL178	Light	Yes		43200	720		
E21	Fire temperature (815.6oC), tank emissivity (0.80)	FL178	Light	Yes		43200	720		
E22	Fire temperature (815.6oC), tank emissivity (1.00)	FL178	Light	Yes		43200	720		
E23	PRV set pressure 165 psig	FL178	Light	Yes		43200	720		
E24	Fill level 87.5%	FL178	Light	Yes		43200	720		
E25	Fill level 80%	FL178	Light	Yes		43200	720		

6. 2-D CFD Tank Model

The two-dimensionality of the CFD model implies that an infinitely long cylindrical geometry can represent the tank in an engulfing fire. The 2-D model is sufficiently complex to account for the key phenomena, notably the free convection of liquid that is the dominant heat transfer mechanism from the shell to the lading, while being computationally tractable. Whereas a 3-D calculation would be able to capture the effect of the tank ends (being exposed to fire or not), three-dimensional liquid flow patterns inside the tank, and variable heating along its length, it would be too computationally expensive to justify this additional benefit, especially given the high variability of accident scenarios. The 2-D CFD model should be regarded primarily as a means to establish the key mechanisms involved in heating the tank and lading, the importance of parameters such as fire temperature, crude oil type, and thermal protection, and the relative timelines for various outcomes.

The model was created using the software ANSYS-CFX Version 19. The geometry and mesh are shown in Figure 6.1. The mesh resolution is finer close to the wall (in the direction perpendicular to the wall) because liquid convection is the dominant mode of heat transfer to the lading and the wall boundary layer is important for capturing this effect.

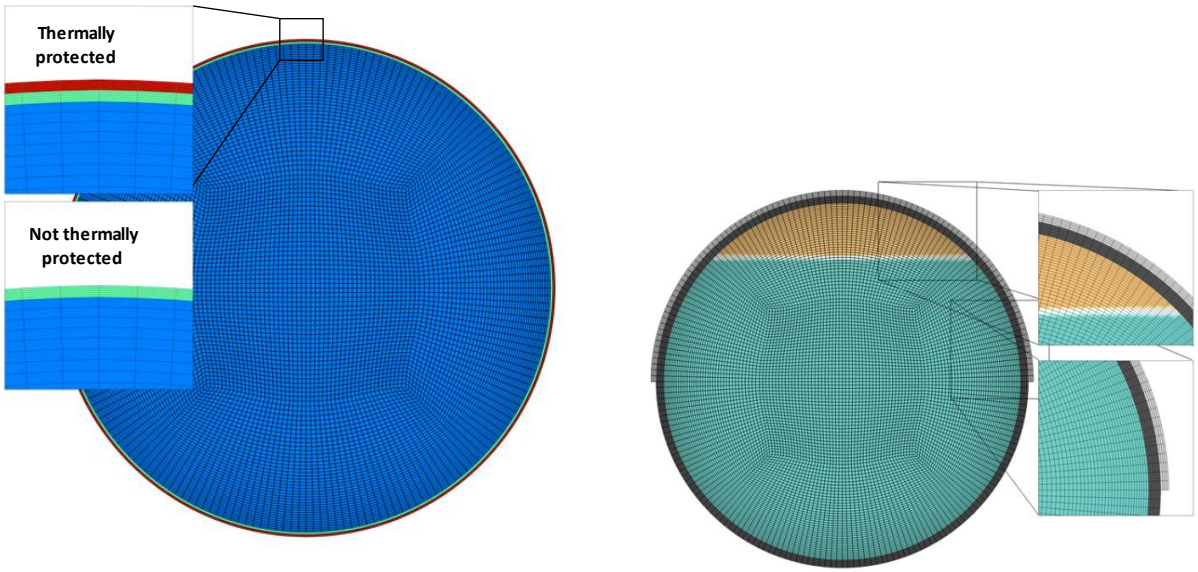

(a) (b)

Figure 6.1: The 2-D CFD model (not to scale). It includes the thermal protection (if present), the steel shell, and the liquid and gas inside. (a) Full size tank (b) 1/3-scale (1/27-volume) experimental tank

The tank contained two continuum phases—liquid and air—so the Eulerian-Eulerian model with standard free surface interface tracking was used. Air was treated as an ideal gas and it participated in conductive and convective heat transfer, although its ability to remove heat from the shell is very small compared to that of the liquid. Radiation inside the tank was investigated using this 2-D CFD model for one case through a newly available beta feature in ANSYS-CFX. The effect this has on the lading heat-up will be discussed when examining this case.

The CFD model calculates detailed flow and heat transfer inside the tank. These are used to determine quantities of interest versus time, such as the heat transfer rate, temperature (distribution), and pressure. Thermal expansion drives convective flow of the liquid in the tank through buoyancy effects. It also increases the volume occupied by the liquid, which then compresses the gas space, increasing the pressure in the tank. In addition to convection, the model accounts for the simultaneous conduction of heat by the liquid.

Note that the Boussinesq approximation was not used for this buoyancy-driven flow. The Boussinesq approximation assumes that the differences in density between warmer and cooler fluids are negligible in the momentum equation, except in the terms that are responsible for generating the buoyancy force. When the Boussinesq approximation is invoked, the resulting momentum equation has a buoyancy force term containing the thermal expansion coefficient of the liquid multiplied by a temperature difference (with respect to a reference temperature). Instead, in the approach used here, the momentum equation was solved directly, using the density versus temperature curves for the fluid that were calculated using HYSYS (which will be shown in Section 8.1). This method brings added computational expense but has the advantages of accurately representing the density variation over a large temperature range and of tracking the liquid expansion, which plays a major if not dominant role in pressurizing the tank at high fill levels.

In the current study, the pressurization caused by liquid thermal expansion was tracked in both the HYSYS simulations and the CFD simulations. The HYSYS simulations, however, also accounted for any liquid evaporation that might have occurred. Consequently, the CFD is relied upon mainly to provide liquid convection heat flux rates and the resulting pressurization is provided by HYSYS.

The heat-transfer-versus-time profile from shell to liquid provided by the CFD simulations would be applicable to any high fill-level scenario because heat transfer is dominated by the free convection flow of the liquid. The convection of liquid is not sensitive to pressure and, therefore, it is not sensitive to initial fill level. On the other hand, the time to reach venting pressure is sensitive to initial fill level, and the HYSYS simulations account for this behavior.

The present 2-D CFD tank model does not account for the pressure relief valve so the analysis ends when the relief pressure is reached. As mentioned, the CFD analysis does not include evaporation or boiling, which would cause further pressurization of the tank, because the numerical time step required to account for the details of boiling was so small that it severely slowed down the simulation. The CFD results will indicate when evaporation conditions have been reached, after which the HYSYS model results, which include both thermal expansion and evaporation, should be used to obtain a more representative prediction of the pressure inside the tank.

The viscosity of the liquid resists its flow. Further resistance is caused by turbulence, which also augments convective heat transfer. The k-epsilon turbulence model with scalable wall functions was used because the speeds generated by this buoyancy-driven flow will result in turbulence and the developing boundary layer will not separate from the wall. The Shear Stress Transport k-omega model was also run and found to differ from the k-epsilon heat transfer result by only 1%.

The radiant exchange described by Equation (3.1) was used to represent the fire as a boundary condition, where the fire temperature, T_f, is specified and the tank outside surface temperature, T_s, is part of the solution. This was found to be the correct representation, even for a fire in intimate contact with the tank, through the validation exercise described in Appendix A.

The typical lading response is shown in Figure 6.2. In addition to the motion and temperature of the liquid lading, the plot also illustrates that liquid thermal expansion reduces the volume for gas and vapour at the top and contributes to pressurizing the tank. The thermally protected tank heats more slowly, causing a slower thermal expansion of the liquid.

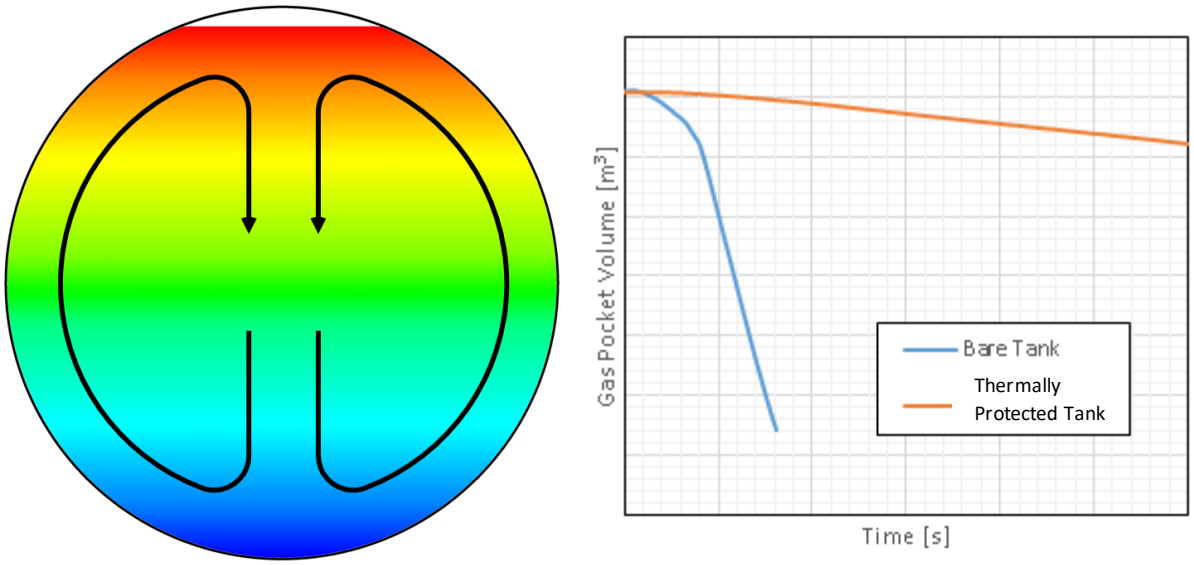

(a) (b)

Figure 6.2: (a) Liquid flow direction and temperature distribution when heated. (b) Volume of the gas/vapour head space reduces as the liquid expands when heated.

7. 3-D Pressure Release Valve Model

A pressure release valve was modeled by CFD to study gas *versus* liquid flow, discharge coefficients, and the start-to-discharge *versus* full open pressures. Initial CFD studies found that pressure relief valves do not necessarily reach full open and, therefore, multiple simulations with different openings were necessary to establish the percentage opening that provides the manufacturer-specified flow rate at a

given pressure. Multiple piston placements were modeled representing from 100% open (full open) to 35% open. A 64% opening was found to match the performance reported by the manufacturer of 10,730-scfm airflow at 85 psig tank pressure. In addition, partially blocked valves were simulated to examine the behavior of valves whose flow path has been restricted by solids accumulation such as by coking of the crude oil.

The computational mesh, a portion of which is shown in Figure 7.1, contained 4,836,483 elements. Figure 7.1 shows that the calculation domain was extended beyond the valve exit face to account for downstream effects. This outer ring contained 787,740 elements in the gas discharge simulations to capture the transition to supersonic speed and 111,989 elements for the liquid discharge simulations. The extension of the calculation domain beyond the valve outlet is necessary for the gas flow calculations because the valve outlet is effectively the throat of a converging-diverging nozzle and effects downstream of the throat are important. Calculations of the crude oil liquid flows gave nearly the same result regardless of whether the computational outlet was placed at the valve outlet or downstream.

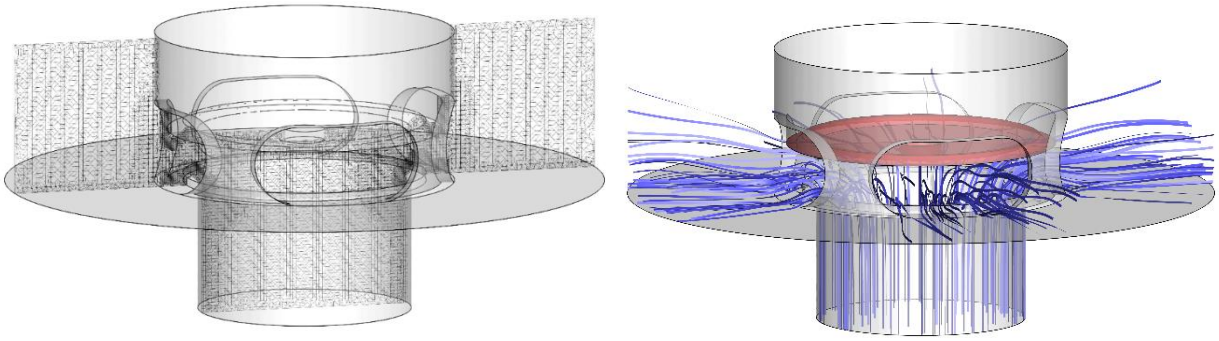

(a) (b)

Figure 7.1: Pressure relief valve. (a) The computational mesh (b) The flow path

The standard k-epsilon model with scalable wall functions was used to account for turbulence effects. All walls were specified as smooth with the no-slip condition (zero velocity at the wall). Constant heat capacity, viscosity, and thermal conductivity at nominal temperature and pressure were assigned for each of the crude oils and the gases. The density for gases was calculated from ideal gas law whereas the density for each liquid was constant. The inlet condition for the valve was a specified total temperature and total pressure representing the pressure and temperature inside the tank.

To calculate the discharge coefficient, the CFD-calculated mass flowrate is compared to the ideal flowrate for the same size hole in the shell, as depicted in Figure 7.2. The ideal flowrate is the flowrate for the given hole-size if there were no losses. The ratio of actual-to-ideal flowrate defines the discharge coefficient, C_D. The hole size in the shell is the measure of valve performance, not the outlet area of the valve. If the valve restricts the flow more than the size of hole in the shell, this restriction is considered the fault of the valve. The hole in the shell for this valve is 3.313 inch-diameter.

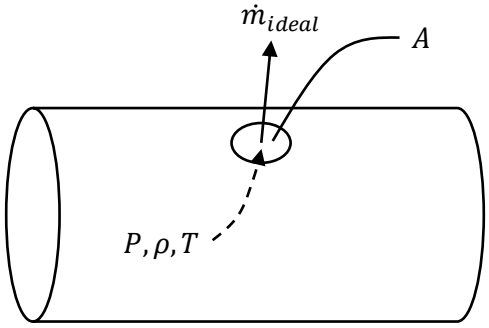

Figure 7.2: The ideal flow rate, $\dot{m}_{ideal}$, is defined by the size (area, A) of hole in the shell and the conditions (pressure, P, temperature, T, and density, ρ) in the tank

The discharge coefficient, C_D, for incompressible (liquid) flow, $\dot{m}$, is derived from the Bernoulli equation and is given by:

$$\frac{\dot{m}}{A} = C_D\sqrt{2P\rho} \tag{7.1}$$

The discharge coefficient, C_D, for compressible (gas) flow, $\dot{m}$, is derived from the isentropic flow equations and is given by:

$$\frac{\dot{m}}{A} = C_D\, P\sqrt{\frac{\gamma}{RT}\left(\frac{\gamma+1}{2}\right)^{\frac{\gamma+1}{2(1-\gamma)}}} \tag{7.2}$$

where $\gamma = c_p/c_V$ is the ratio of specific heats for the gas at constant pressure and constant volume and $R = \mathcal{R}/\widehat{M}$, where $\mathcal{R}$ is the universal gas constant and $\widehat{M}$ is the molecular weight of the gas (mixture). This formula assumes choked flow at the throat, which in this case is the hole in the shell. Choked flow occurs for the discharge pressure level in this study and the CFD simulations corroborated this.

8. Results

8.1 HYSYS Lading Properties

The vapour-liquid equilibrium diagrams and physical properties of different crude oils generated by HYSYS calculations provided an opportunity to compare these lading properties and examine differences between crude oil types.

Figures 8.1.1 and 8.1.2 show sample saturation temperature and pressure plots for ladings considered in this report. Figure 8.1.1 shows how the narrow range of boiling points in condensates could cause a BLEVE to occur even when the pressure relief valve is functioning. An initially 87% full tank with condensate (C1)

has been heated from 27°C to 87°C and, simply by liquid and gas thermal expansion, *i.e.*, without requiring evaporation, the tank has pressurized to 549360 Pa absolute (65 psig). Upon loss of containment, the tank suddenly depressurizes to atmospheric pressure, at which point all the liquid in the tank is suddenly at a temperature and pressure at which it would normally be vapour. In this case, an instantaneous depressurization could lead to a BLEVE.

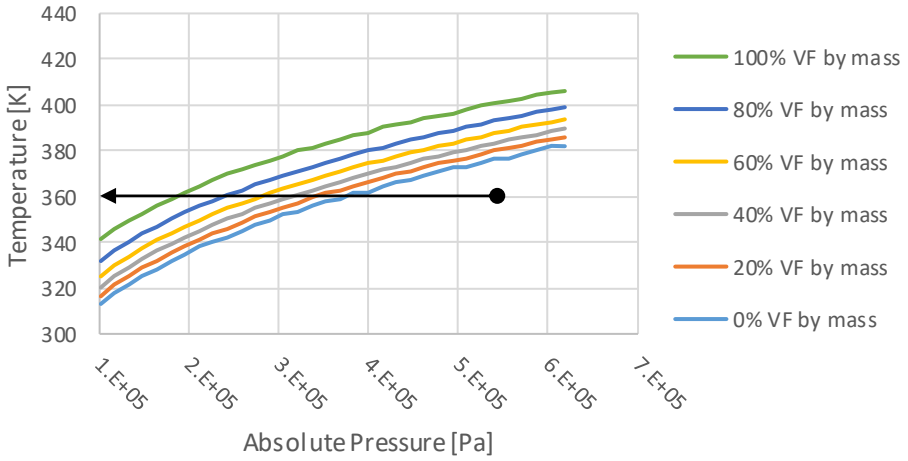

Figure 8.1.1: Saturation temperature and pressure for condensate C1. "VF" stands for "vapour fraction." The filled circle indicates a tank at pressure, 549360 Pa absolute (65 psig). The arrow represents sudden loss of containment and depressurization to atmospheric pressure.

The saturation temperature and pressure plot for the condensate is repeated in Figure 8.1.2, but this time with the same y-axis scale as for the crude oils to aid in visual comparison. It is apparent that even the light crude oil has a significantly larger range of boiling temperatures, some of which are much higher than that of the condensate, thereby reducing the propensity to BLEVE. Moreover, the heavier the crude, the larger the range of boiling temperatures, which further reduces the chance and severity of BLEVE. From this comparison it can be concluded that a tank car carrying condensates, if exposed to a fire, has a higher risk of severe BLEVE than crude oils.

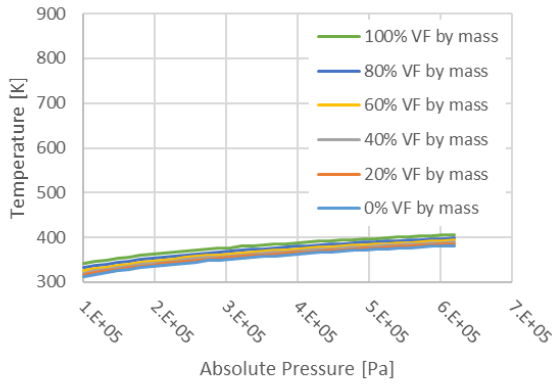

(a)

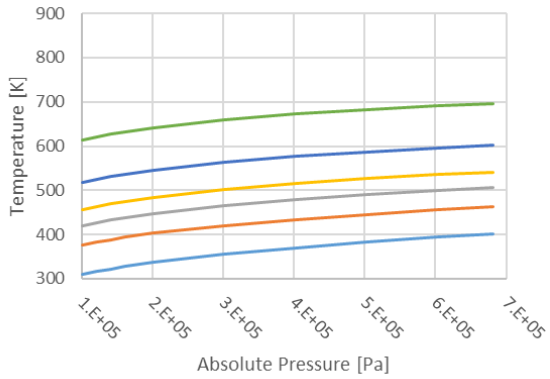

(b)

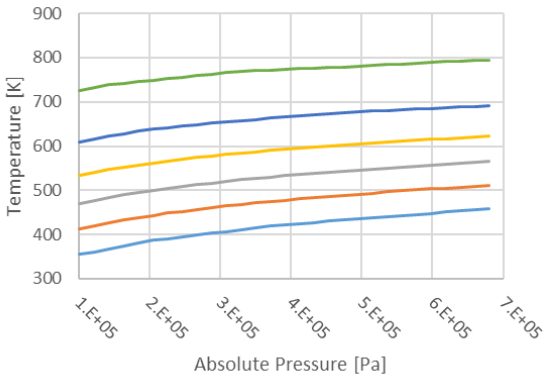

(c)

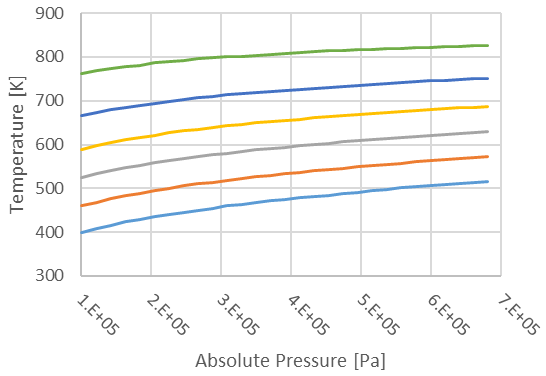

(d)

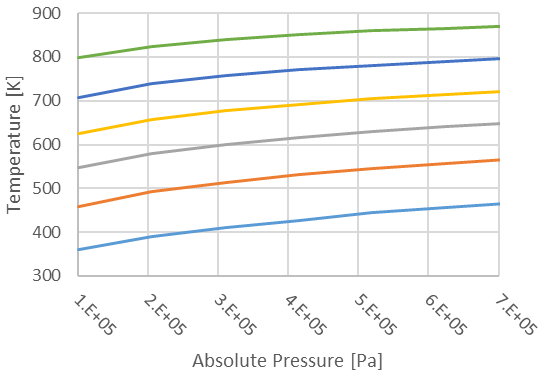

(e)

Figure 8.1.2: Saturation temperature and pressure. “VF” stands for “vapour fraction”. (a) condensate C1 (b) light crude L1 (c) light medium crude LM1 (d) light medium crude LM2 (e) medium sour crude MS1

Figure 8.1.3 provides the density, viscosity, heat capacity, and thermal conductivity of the ladings studied. The lighter crude oils and especially the condensate are less dense. The maximum gross rail load of 286000 lbs (129705 kg) limits the combined weight of the tank and lading. The tare weight of the tank car is assumed to be 90085 lbs (40855 kg) based on a DOT 117 tank car. Based on a maximum lading mass (maximum total mass minus the mass of the tank car itself) of 88850 kg and a tank volume of 115.6 m^3 (30540 US gallons), the light medium crude, LM1, could be filled to 95% by volume, the light crude, L1, could be filled to 97%, and the condensate could be filled to 100%. Very high fill levels result in very rapid pressurization of the tank when heated and a higher likelihood of liquid being vented through the pressure relief valve.

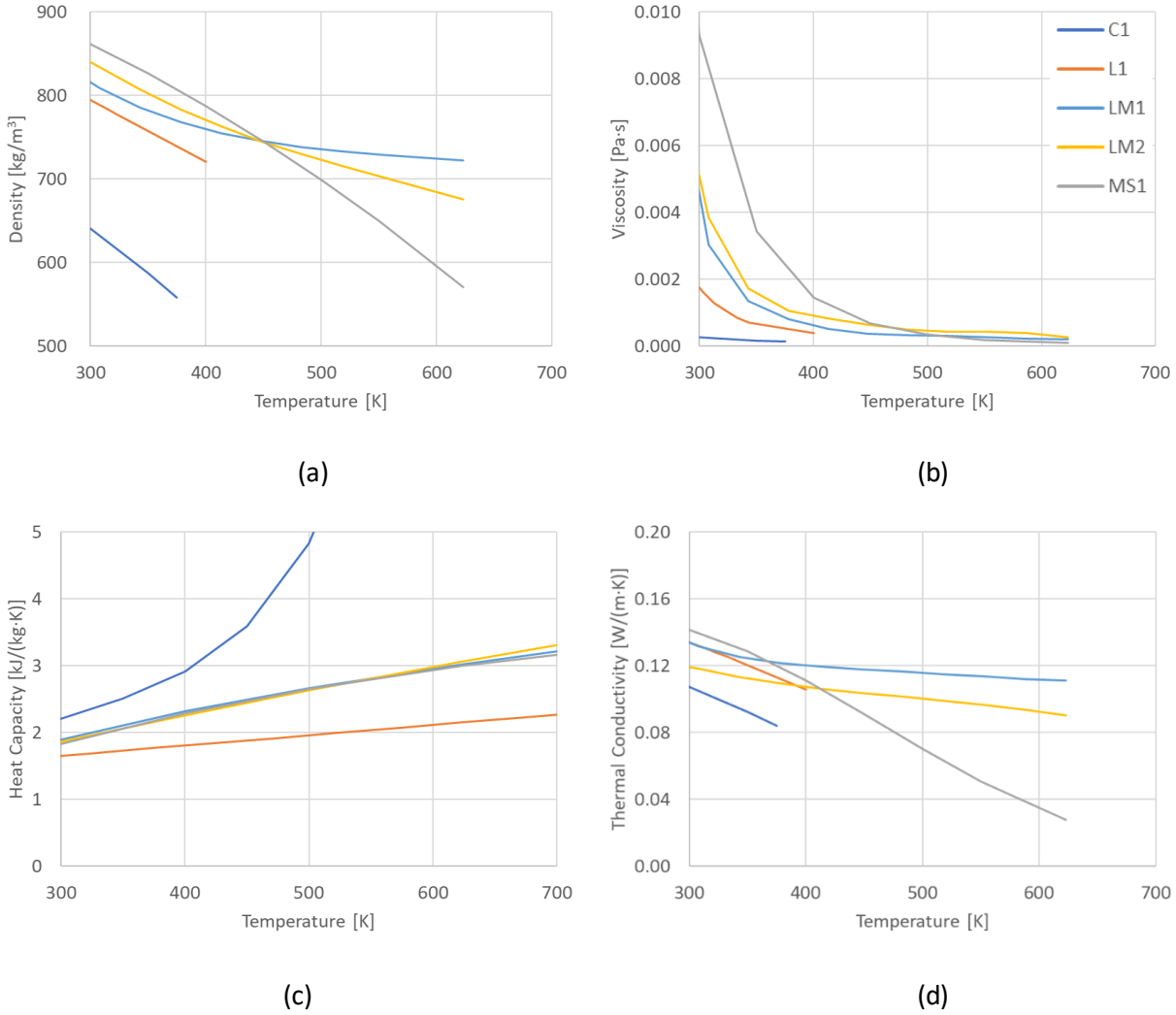

Figure 8.1.3: Liquid properties as a function of temperature (a) Density (b) Dynamic viscosity (c) Heat capacity (d) Thermal conductivity

There is a very large range of viscosities among the different ladings at ambient temperature. The low-viscosity condensate and light crude oil will begin moving and transferring heat by convective heat transfer quickly compared to the medium crude oil. Once heated, though, the viscosity reduces significantly for all the crude oils. Less viscous crudes (typically the lighter ones), will heat up faster in a fire than more viscous crudes, but at higher temperatures (around 400 K or 127°C, referring to Figure 8.1.3 (b)), the convective flow will become less dependent on crude oil type.

8.2 HYSYS/Matlab Lading Reactions

The following section summarizes the modeling results for tank car fire scenarios with and without the inclusion of thermal cracking reactions, as specified in Sections 4 or 5. A series of calibration runs were first conducted to (1) ensure proper communication between and Aspen HYSYS and coded VLE-reaction model (VBA code in Microsoft Excel), (2) ensure all parameters were initialized correctly, and (3) ensure the model provides stable and physically significant results (i.e., results that are in line with real systems).

Based on these initial calibration runs, it appeared as though the combined tank car model performed as expected with one caveat - an initial fill level of 95% would not allow for stable operation. Although the specific details of these runs are not shown here, the thermal expansion of the liquid resulted in elimination of the vapour headspace and subsequent unstable discharge of liquid through the PRV. As the PRV is specifically designed for vapour discharge, this caused a discontinuity in phase equilibria and the inability for the VLE-reaction model to describe the vapour-liquid breakdown of the system. Therefore, the initial fill level was systematically reduced until stable VLE was achieved at 75%.

As stated previously, kinetic rate expressions and data were determined for three crudes, namely: a medium crude (MBL), a heavy synthetic (AHS), and a dilbit (CDB). In order to determine if there was a discernable difference between scenarios with (Run #R1) and without (Run #R2) the presence of reactions, several key lading system properties were examined as a function of time under fire conditions (see Sections 4 and 5 for details). These included:

1) Temperature
2) Pressure
3) Total mass
4) Liquid level

In each case, bare tanks (i.e., no insulation or thermal protection) were considered and it should be noted that this does not take away from the results, as we were studying the effects of a particular variable (reactions), not modeling a real life scenario.

Figures 8.2.1 to 8.2.4 below present these key lading system properties versus time with and without the presence of thermal cracking reactions for a medium crude oil (MBL). From these figures, it is clear that the system reacts as expected to heat input. From time zero, the temperature of the lading starts to increase (Figure 8.2.1), which results in an increase in liquid level due to the lowering in crude oil density (Figure 8.2.2). The system pressure begins to increase up to the PRV relief pressure (1239 kPa, in this case), where it is maintained *via* venting of vapour from the system (Figure 8.2.3). This increase in pressure is

caused by (1) a reduction in available vapour headspace, (2) a decrease in vapour density from heating, and (3) vapourization of hydrocarbons *via* VLE. The combination of these three factors results in a non-linear, exponential pressure increase. Figure 8.2.4 shows the total mass of system over the heating period. As expected, the system mass is constant (closed system) up until the initial relief event at ~29 minutes when the PRV opens and remains open for the duration of the run.

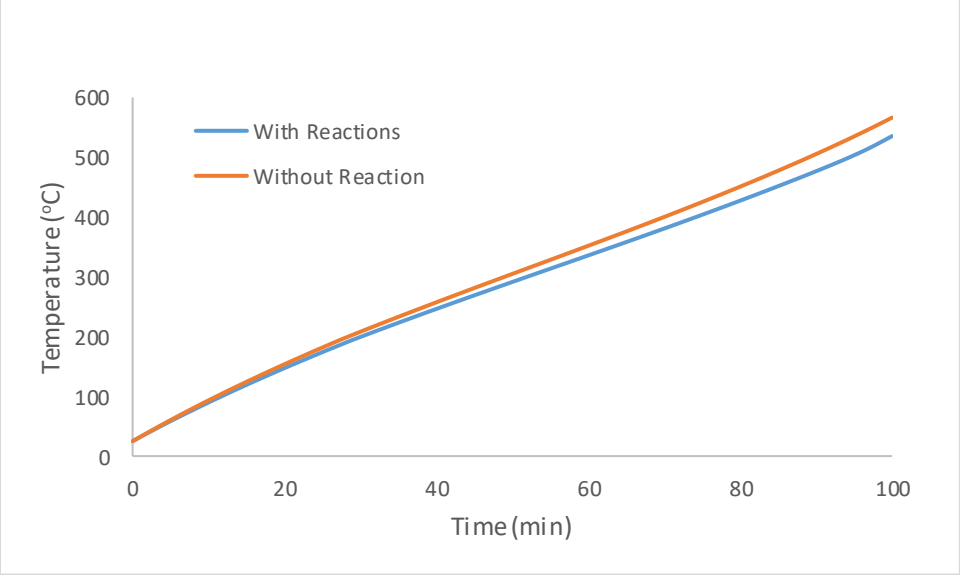

Figure 8.2.1: System temperature versus time with and without thermal cracking reactions – Medium crude sample (MBL).

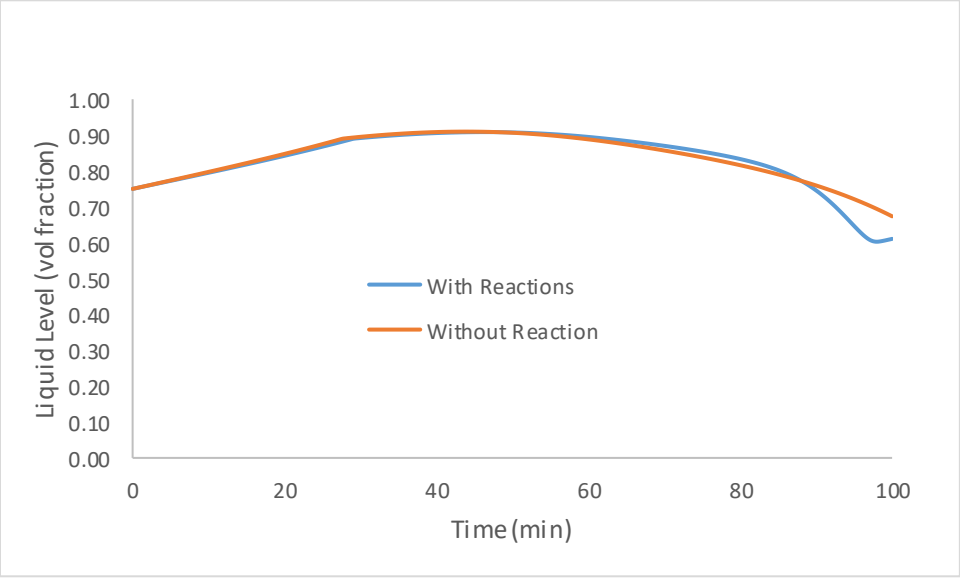

Figure 8.2.2: System liquid level versus time with and without thermal cracking reactions – Medium crude sample (MBL).

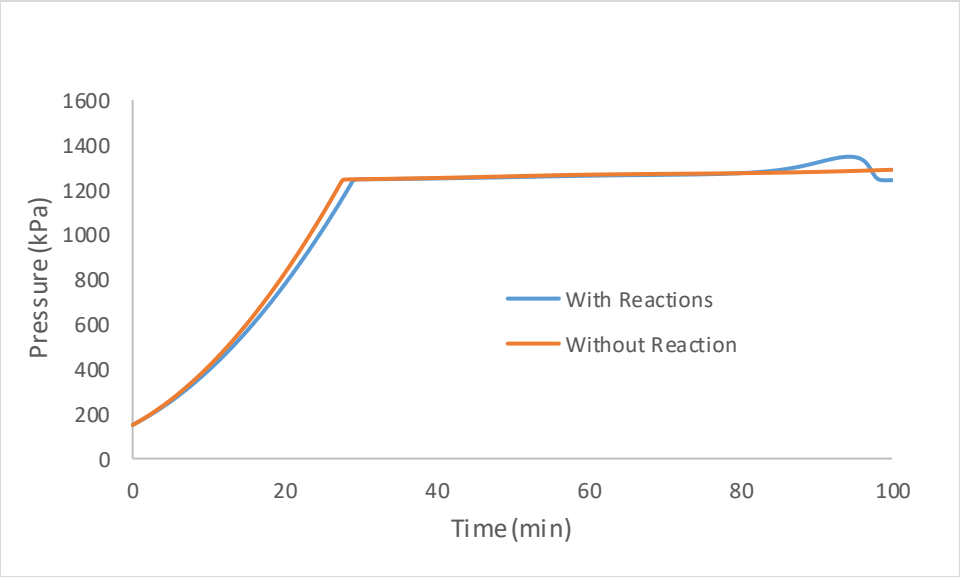

Figure 8.2.3: System pressure versus time with and without thermal cracking reactions – Medium crude sample (MBL).

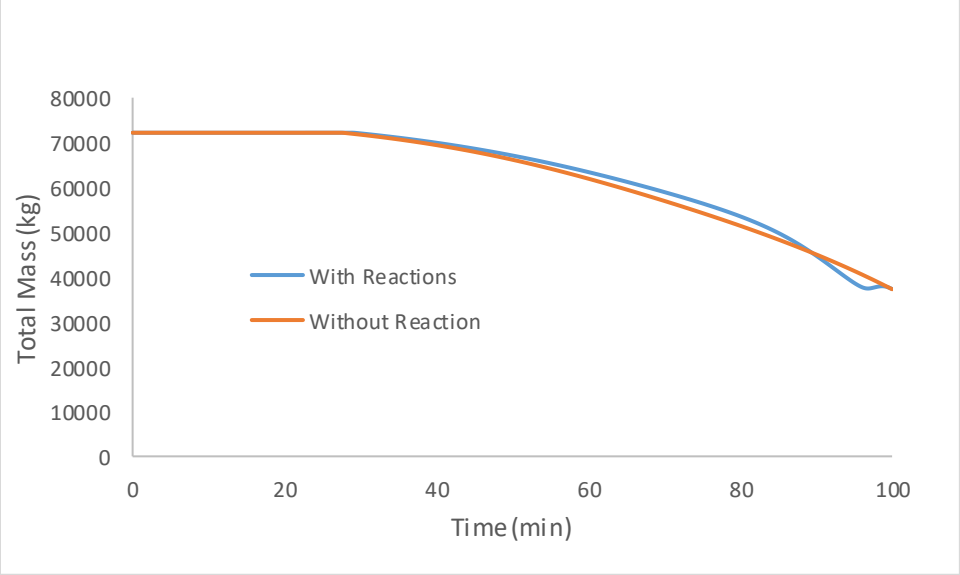

Figure 8.2.4: System total mass versus time with and without thermal cracking reactions – Medium crude sample (MBL).

Figures 8.2.1 to 8.2.4 also present a comparison between tank car fire scenarios with and without the inclusion of thermal cracking reactions for the medium crude oil (MBL). From Figure 8.2.1, it can be observed that system temperature increases more slowly when thermal cracking reactions are considered. The primary driver for this phenomenon is the endothermic (requires heat) nature of thermal cracking reactions, and small differences in thermal heat capacities of the resulting changes in phase

compositions (see Figures 8.2.5 to 8.2.9). This will be discussed in more detail below. As a result of the slower temperature ramp, it takes slightly longer to reach the initial relief event (~29 versus ~28 minutes) and the total system mass without reaction starts to decrease slightly ahead of the case where reactions are considered (Figure 8.2.3 and 8.2.4, respectively). The liquid level for both cases follow a similar trend (Figure 8.2.2) until the onset of thermal cracking at a temperature of ~400°C. At this point, there are significant changes in system behaviour that require particular attention and discussion.

Figure 8.2.3 depicts a situation where the PRV is incapable of controlling the system pressure at the ~80-minute mark when reactions are considered – the system pressure is above the set pressure of the PRV (1239 kPa). To try to understand why this occurred, a detailed examination of the system composition is required. Figures 8.2.5 to 8.2.9 present the liquid phase lump 'Residue', 'VGO', 'LGO', 'GLN', and 'Gas' mass fractions, respectively, versus time with and without the presence of thermal cracking reactions for the medium crude oil sample (MBL). Definitions for each lump can be found in Table 5.3.1, with additional information about crude oil lumping practices located in previous works – "Crude Oil Equation of State Modeling and Experimental Test Validation - Tasks 1 to 4 Year-end Progress Report."

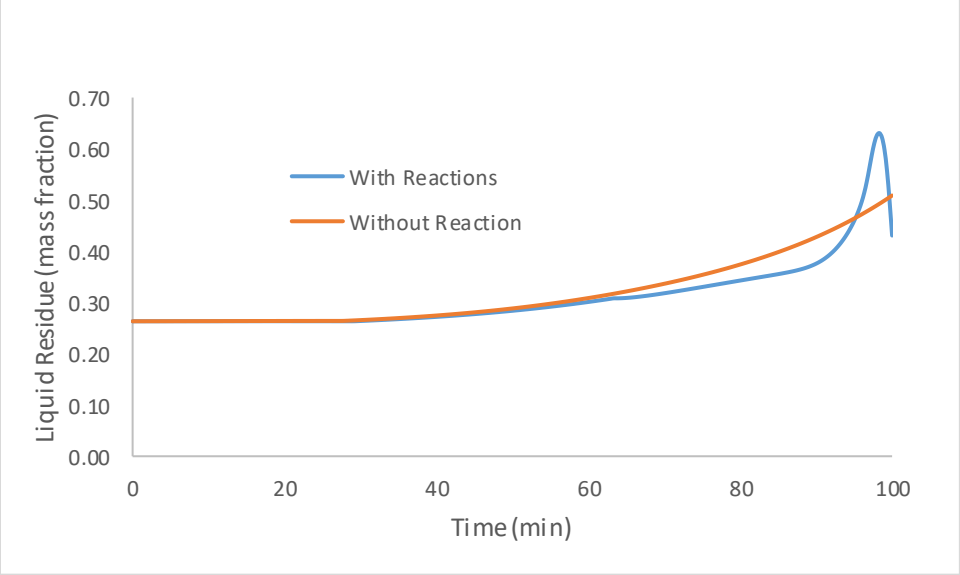

Figure 8.2.5: Liquid phase Residue mass fraction versus time with and without thermal cracking reactions – Medium crude sample (MBL).

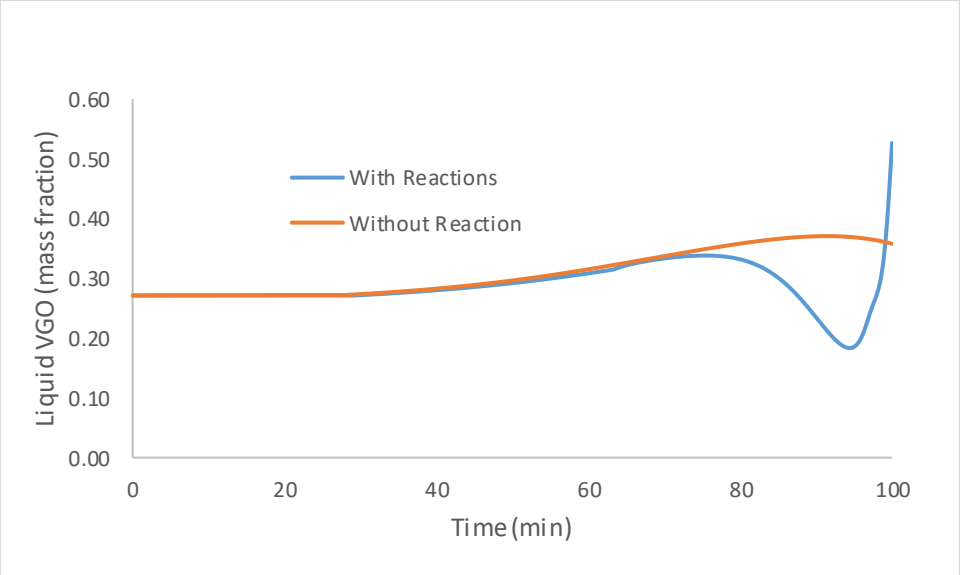

Figure 8.2.6: Liquid phase VGO mass fraction versus time with and without thermal cracking reactions – Medium crude sample (MBL).

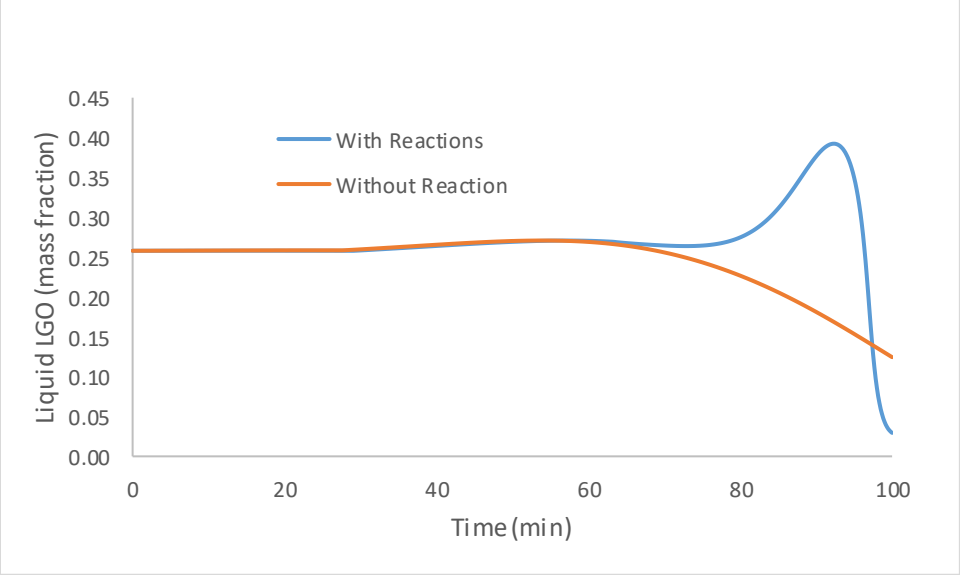

Figure 8.2.7: Liquid phase LGO mass fraction versus time with and without thermal cracking reactions – Medium crude sample (MBL).

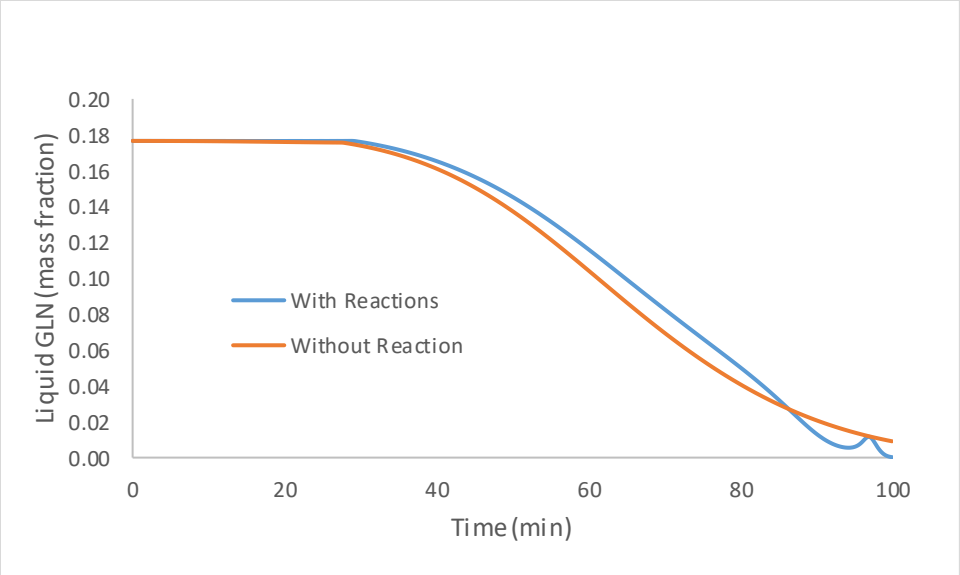

Figure 8.2.8: Liquid phase GLN mass fraction versus time with and without thermal cracking reactions – Medium crude sample (MBL).

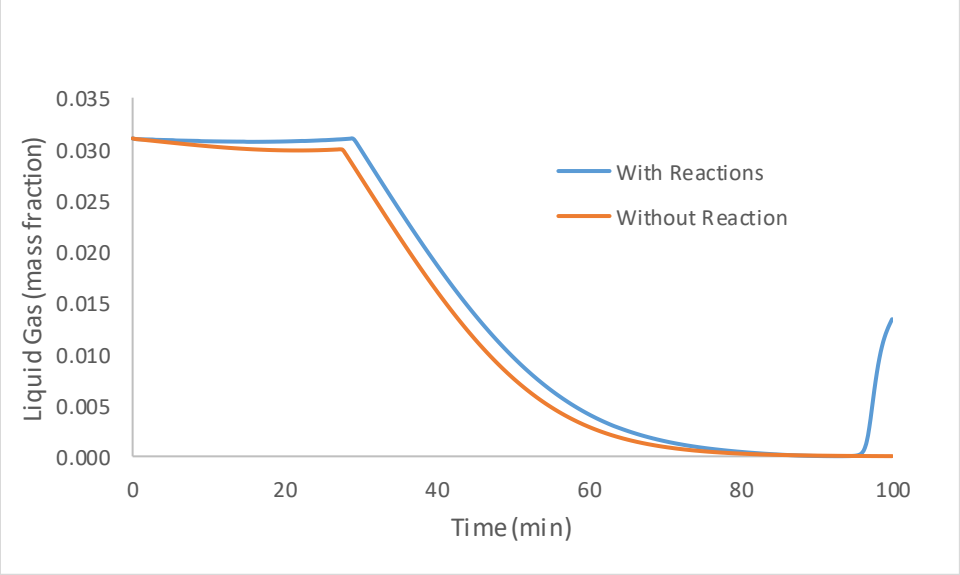

Figure 8.2.9: Liquid phase Gas mass fraction versus time with and without thermal cracking reactions – Medium crude sample (MBL).

As the temperature is raised above ~400°C, mild thermal cracking reactions begin to become significant and influence the overall performance of the system, primarily *via* changes in the pressure profile. When not considering cracking reactions, the liquid mass fraction of the heavier lumps 'Residue' and 'VGO' increase over time as the lighter lumps are transferred to the vapour phase, as seen in Figures 8.2.5 and

8.2.6. In contrast, when reactions are considered this increase is initially limited due to the consumption of 'Residue' and 'VGO," but eventually results in an overall increase in the heavier lumps as the lighter components are vapourized and vented from the system. The combined VLE-reaction model is relatively complex as the thermal cracking kinetic parameters differ between lumps and are temperature/phase dependant. This means it can be difficult to directly relate changes in system liquid composition to overall system performance (e.g., pressure), particularly under the dynamic and changing system mass (*via* venting) conditions seen in this work. However, some general trends can be observed, namely:

1) For the medium crude, 'Residue', 'VGO', and 'LGO' are the lumps of interest when it comes to overall system performance.
    a. The initial quantities of liquid phase 'GLN' and 'Gas' are relatively small, start to drop as soon as the PRV opens, and therefore, effectively do not participate in the reaction.
    b. It should be noted, however, that these lumps are being generated *via* thermal cracking of the heavier lumps, but because they are only generated at elevated temperature, they are immediately vapourized (see Table 8.2.1) and vented from the system.
2) Once a temperature of greater than 425°C is reached there is a large increase in the quantity of 'LGO', coinciding with the over-pressure event.
    a. This pressure increase can only be caused when the rate of vapourization is greater than the maximum PRV throughput – this is determined using the set pressure, the orifice area, and the fluid passing through a given PRV (discharge coefficient).
    b. It is likely that the production of 'LGO' from the cracking of 'Residue' and 'VGO', and the subsequent vapourization of 'LGO', caused the over-pressurization.
    c. After the majority of the 'LGO' has been vapourized (98-minute mark) and discharged the pressure stabilizes at the set pressure.
3) The 'Residue' continues to thermally crack to the end of the operating period (100 minutes).
    a. The cracking of 'Residue' primarily forms 'VGO' and 'Gas' (see Figures 8.2.6 and 8.2.9, respectively).
    b. Even at these elevated temperatures, the rate of 'Residue' cracking is sufficient low enough to avoid any serious system performance issues such as continued system over-pressurization.

It was of interest to extend the operating period beyond 100 minutes to get a 'fuller' picture of system performance up until the point where steady-state conditions were reached (e.g., no change in temperature, liquid level, mass, etc.). However, this was not fundamentally achieveable given the limitation with the current thermal cracking reaction model for two reasons: (1) the thermal cracking reaction kinetics were only experimental measured and validated up to ~450°C and (2) gas phase reactions and coking are expected to be significant above ~500°C. Therefore, the maximum operating period was not increase to beyond 100 minutes and system performance results above ~500 or 550°C should be used with caution.

A similar set of tank car fire scenarios cases with and without the inclusion of thermal cracking reactions were performed for a heavy synthetic oil (AHS – Run# R3 and R4) and a dilbit (CDB – Run# R5 and R6). The reason for running these cases was to examine how crude oils with different thermo-physical properties

and compositions perform relative to each other under elevated temperatures – i.e., do some crude oils perform better/worse than others from a safety perspective?

Figures 8.2.10 to 8.2.13 present the system temperature, liquid level, pressure, and total mass, respectively, versus time with and without the presence of thermal cracking reactions for the AHS crude oil; Figures 8.2.14 to 8.2.17 present the same parameters for the CDB. As was the case for the MBL, the system reacted as expected to heat input, with a couple of notable differences. There is a more gradual decrease in total system mass up until a point where thermal cracking becomes significant (>400°C). This difference in system performance is caused by the significantly higher initial liquid mass fraction of the heavier species ('Residue' and 'VGO' lumps), which require higher temperatures for vapourization. The liquid level continues to increase over the operating period even as the PRV has started discharging material from the system. This indicates that the rate of liquid thermal expansion outweighs the rate of vapourization in terms of influence on system liquid level. However, system performance is quite varied once thermal cracking temperatures are reached and requires carefully examination of liquid phase lump compositions to describe.

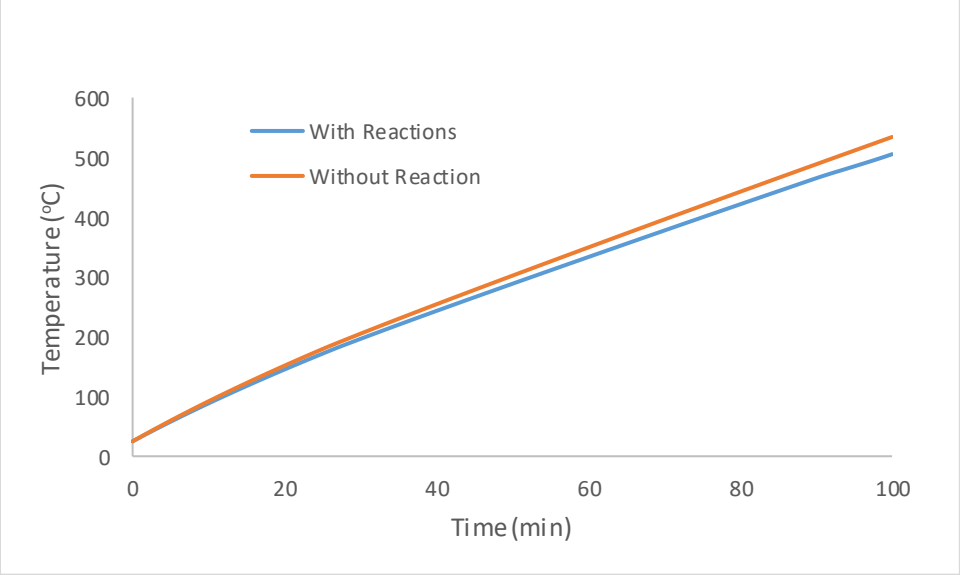

Figure 8.2.10: System temperature versus time with and without thermal cracking reactions – Heavy synthetic crude sample (AHS).

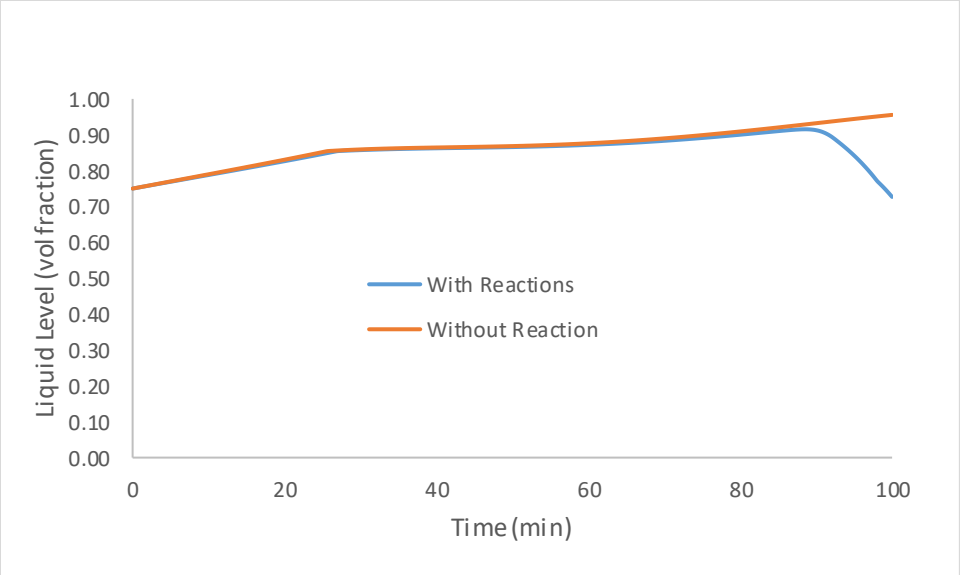

Figure 8.2.11: System liquid level versus time with and without thermal cracking reactions – Heavy synthetic crude sample (AHS).

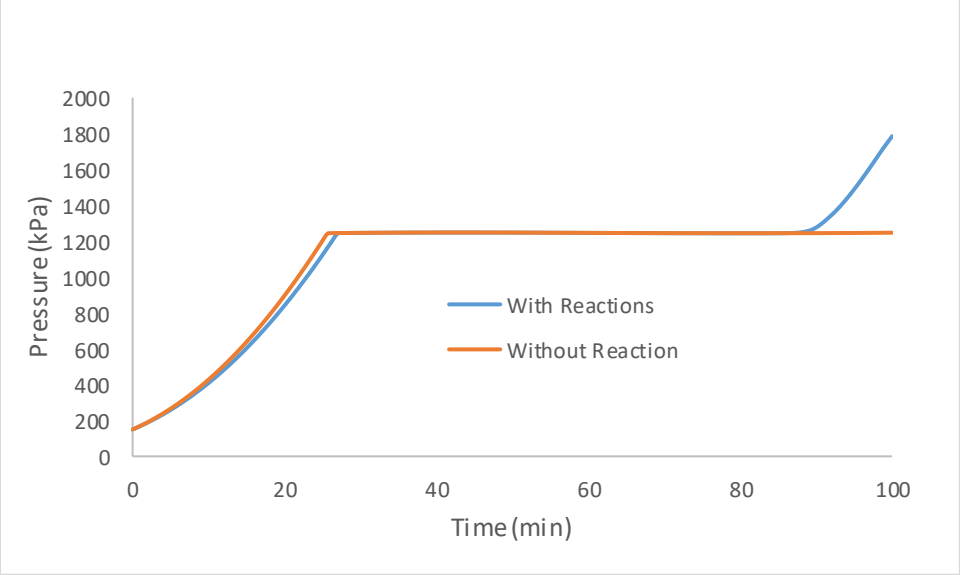

Figure 8.2.12: System pressure versus time with and without thermal cracking reactions – Heavy synthetic crude sample (AHS).

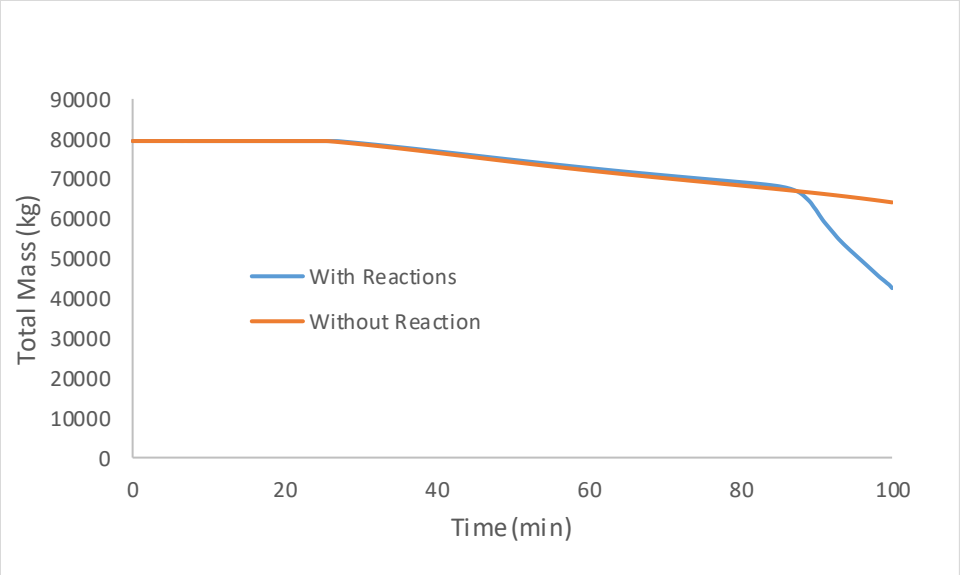

Figure 8.2.13: System total mass versus time with and without thermal cracking reactions – Heavy synthetic crude sample (AHS).

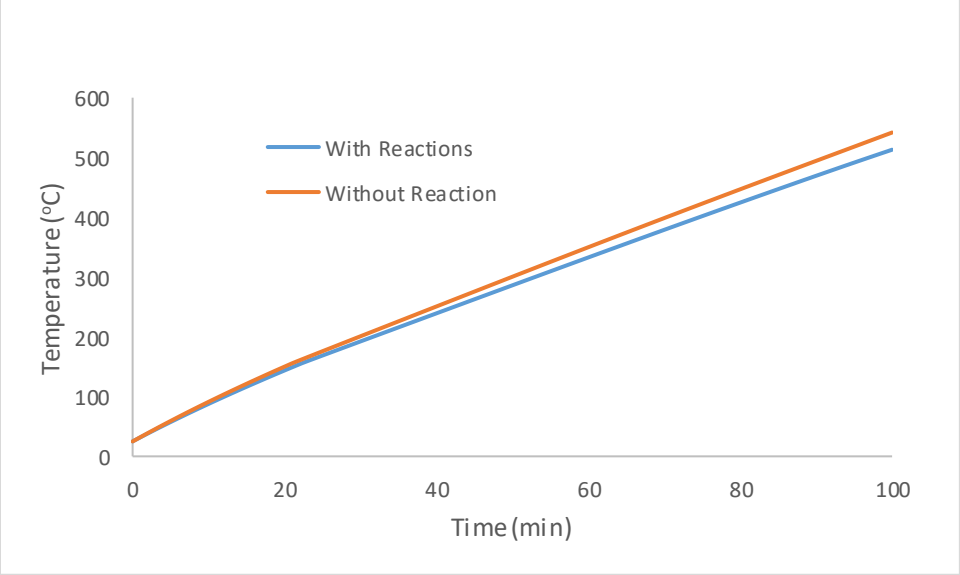

Figure 8.2.14: System temperature versus time with and without thermal cracking reactions – Dilbit sample (CDB).

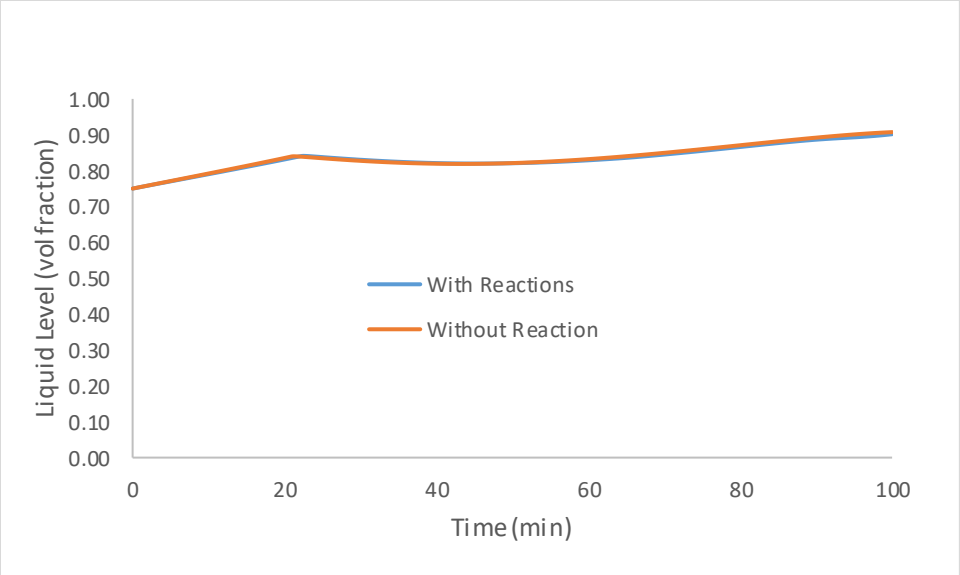

Figure 8.2.15: System liquid level versus time with and without thermal cracking reactions – Dilbit sample (CDB).

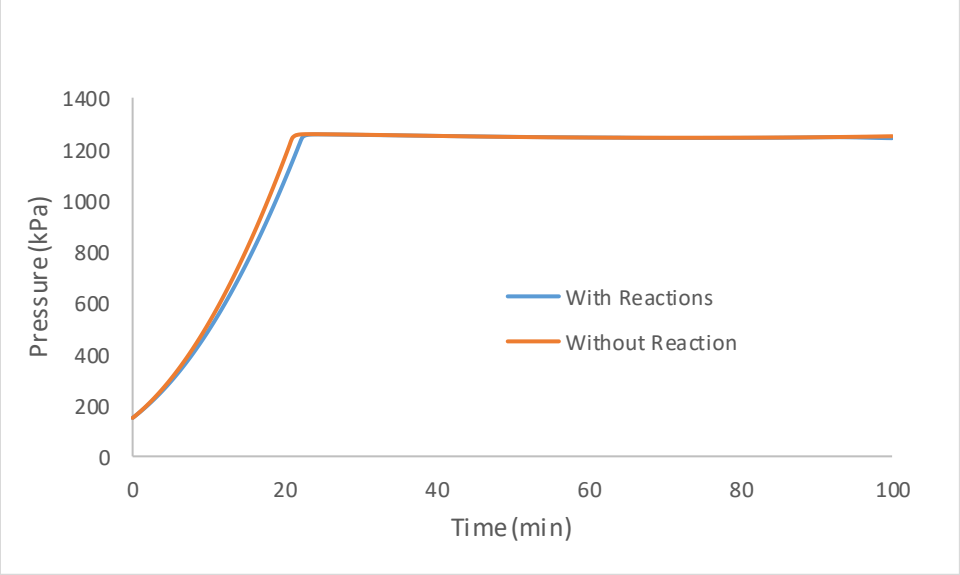

Figure 8.2.16: System pressure versus time with and without thermal cracking reactions – Dilbit sample (CDB).

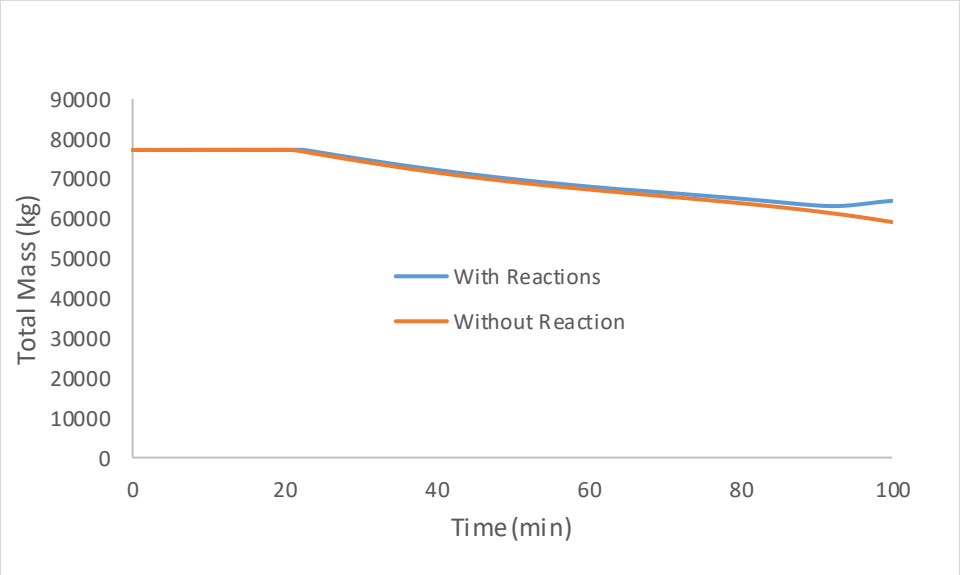

Figure 8.2.17: System total mass versus time with and without thermal cracking reactions – Dilbit sample (CDB).

As was the case for the MBL, the above figures present comparisons with and without the inclusion of thermal cracking reactions (AHS and CDB). Interestingly, both the heavy synthetic and dilbit systems behave differently than the medium crude with reactions – the heavy synthetic system starts to over-pressure at the 90 minute-mark and does not recover (Figure 8.2.12) and the dilbit system pressure never exceeds the PRV set pressure (Figure 8.2.16). This is caused by differences in overall vapour production versus time as the heavier components are cracked into lighter species and subsequently vapourized.

Figures 8.2.18 to 8.2.22 depict the liquid phase 'Residue', 'VGO', 'LGO', 'GLN', and 'Gas' mass fractions, respectively, versus time with and without the presence of thermal cracking reactions for AHS; Figures 8.2.23 to 8.2.27 present the same plots for CDB. Although, it is difficult to directly pinpoint how changes in any given lump at any given time impact system performance, the following general behaviour for the heavy synthetic (AHS) has been noted:

1) Unlike the MBL, the heavy synthetic liquid phase composition is relatively stable up to the ~82 minute-mark.
    a. There are only small changes due to venting of lower boiling point 'GLN' and 'Gas" after the PRV opens (~20 minute-mark) and the temperature is essentially never high enough during the period to vapourize the heavier lumps.
    b. This indicates that the contribution of thermal cracking to system performance is essential insignificant below ~425°C.
2) Above ~425°C, the rate of 'Residue' and 'VGO' consumption to form 'LGO' is substantial.
    a. Near complete conversion is achieved by the end of the 100 minute operating period.
    b. The produced 'LGO' is rapidly vapourized at these elevated temperatures and is vented through the PRV.
    c. There is a rapid decrease in liquid level (Figure 8.2.11) and total system mass (Figure 8.2.13) at the ~82 minute-mark.

3) Under these conditions, the PRV is undersized and the system pressure is driven above the set and full open pressures (Figure 8.2.12), reaching ~1765 kPa at the end of the 100 minute period.
    a. Based on the rate of pressure increase, it is expected that the pressure would climb significantly higher if the run length was extended beyond 100 minutes.
    b. The pressure would only drop down to the PRV set pressure once the majority of the remaining liquid phase 'LGO' has be vapourized and vented from the system.

The results for AHS were generally expected. The system was relatively stable due to the large proportion of heavy components and only started to deviate when the rate of thermal cracking was sufficient. However, the dilbit (CDB) behaved quite differently. The rate of thermal cracking is slower and is really only substantial for 'VGO" at approximately 400°C. The production of liquid phase 'LGO,' and subsequent vapourization, is observed at a rate lower than the maximum attainable flow rate through the PRV. This results in a less severe rate of system mass loss *via* venting and a situation where over-pressurization of the system did not occur (see Figure 8.2.16).

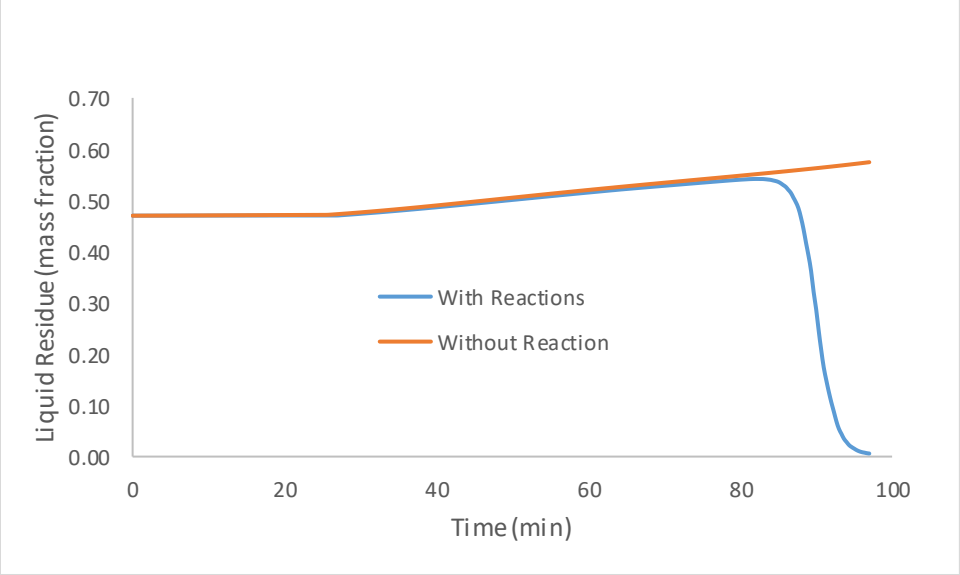

Figure 8.2.18: Liquid phase Residue mass fraction versus time with and without thermal cracking reactions – Heavy synthetic crude sample (AHS).

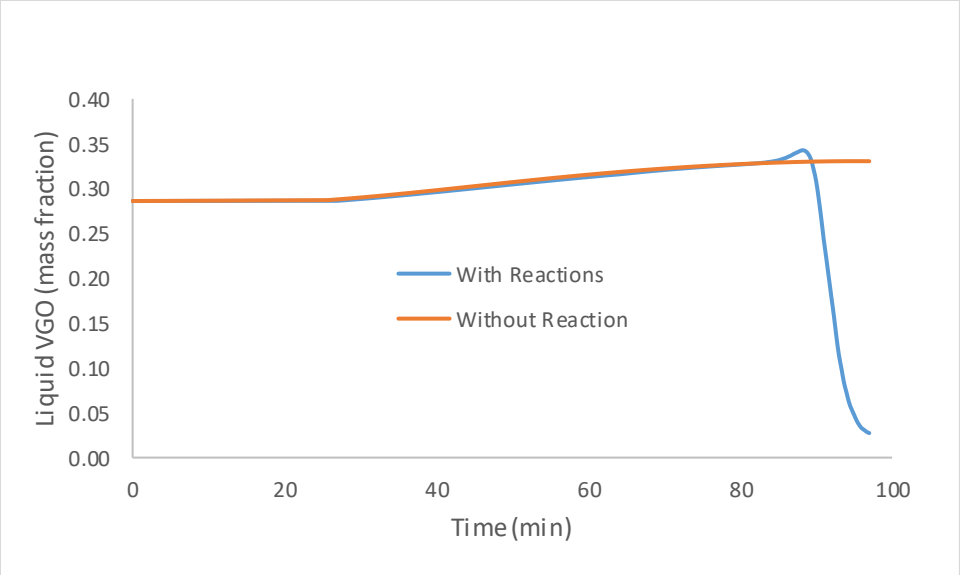

Figure 8.2.19: Liquid phase VGO mass fraction versus time with and without thermal cracking reactions – Heavy synthetic crude sample (AHS).

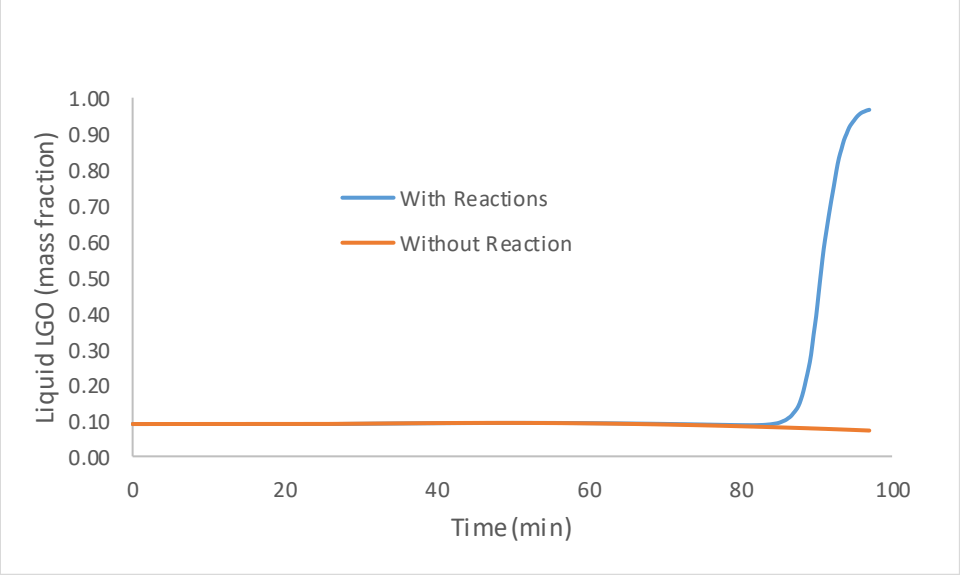

Figure 8.2.20: Liquid phase LGO mass fraction versus time with and without thermal cracking reactions – Heavy synthetic crude sample (AHS).

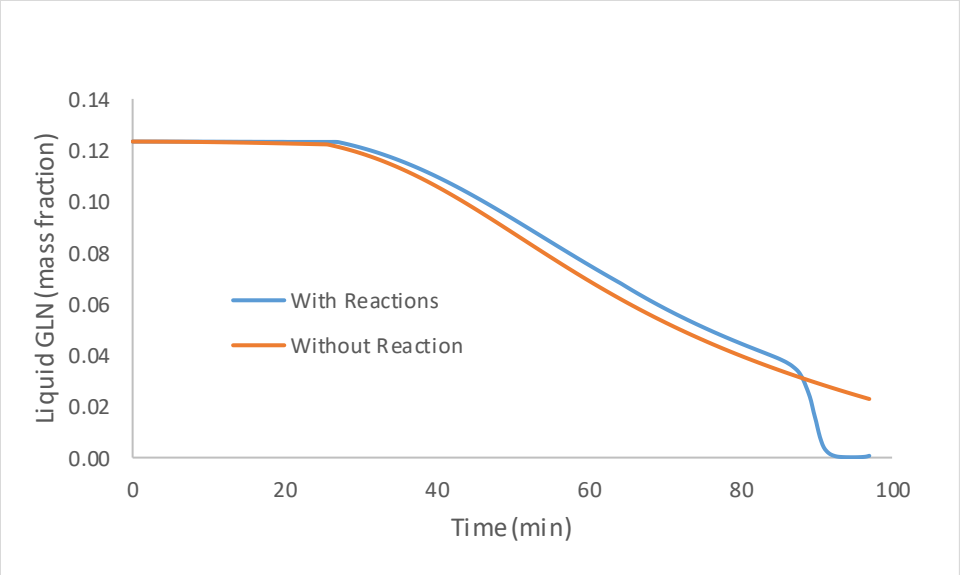

Figure 8.2.21: Liquid phase GLN mass fraction versus time with and without thermal cracking reactions – Heavy synthetic crude sample (AHS).

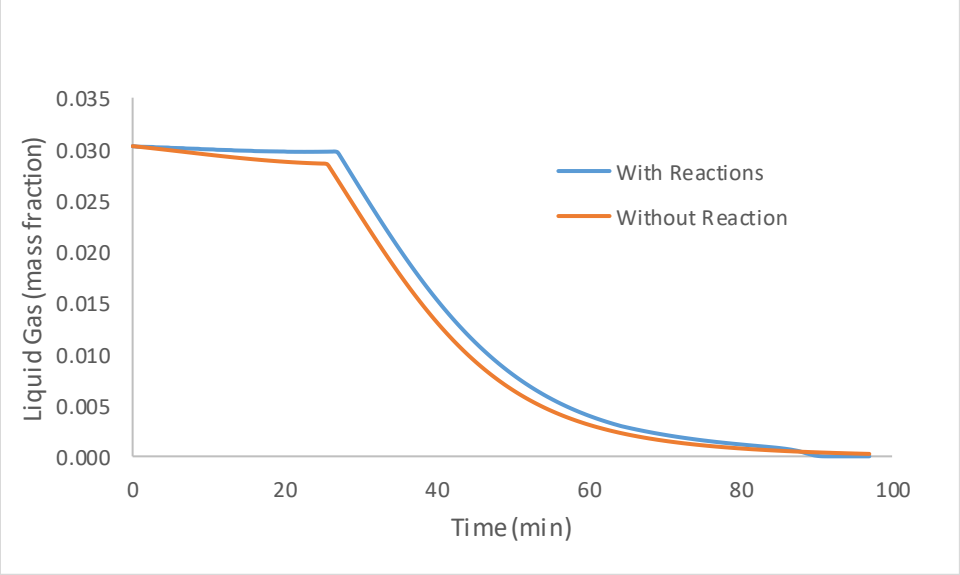

Figure 8.2.22: Liquid phase Gas mass fraction versus time with and without thermal cracking reactions – Heavy synthetic crude sample (AHS).

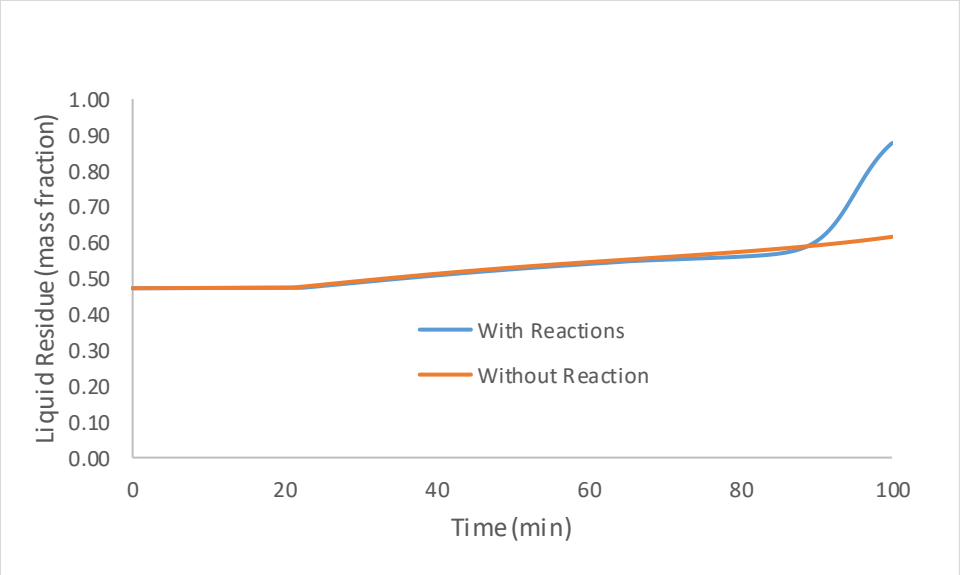

Figure 8.2.23: Liquid phase Residue mass fraction versus time with and without thermal cracking reactions – Dilbit sample (CDB).

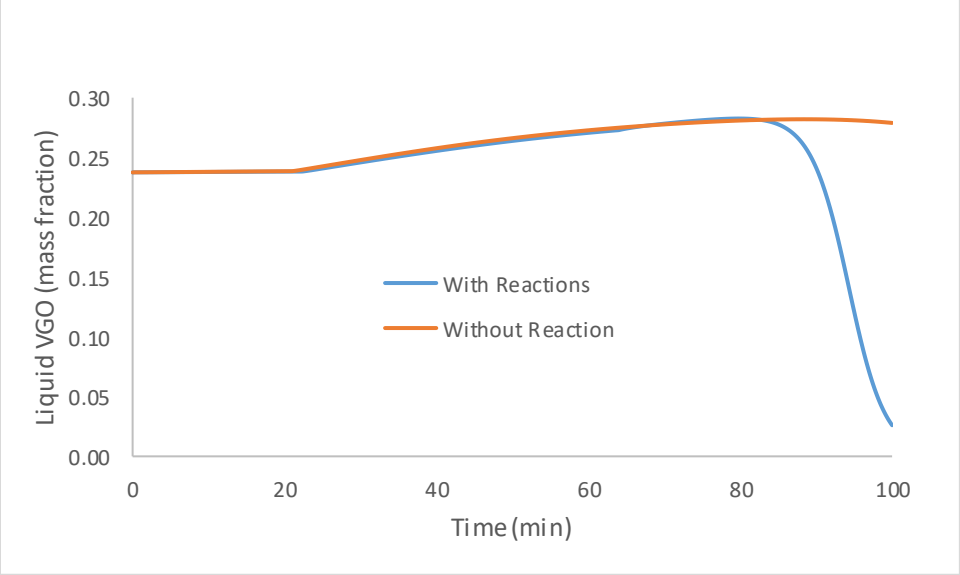

Figure 8.2.24: Liquid phase VGO mass fraction versus time with and without thermal cracking reactions – Dilbit sample (CDB).

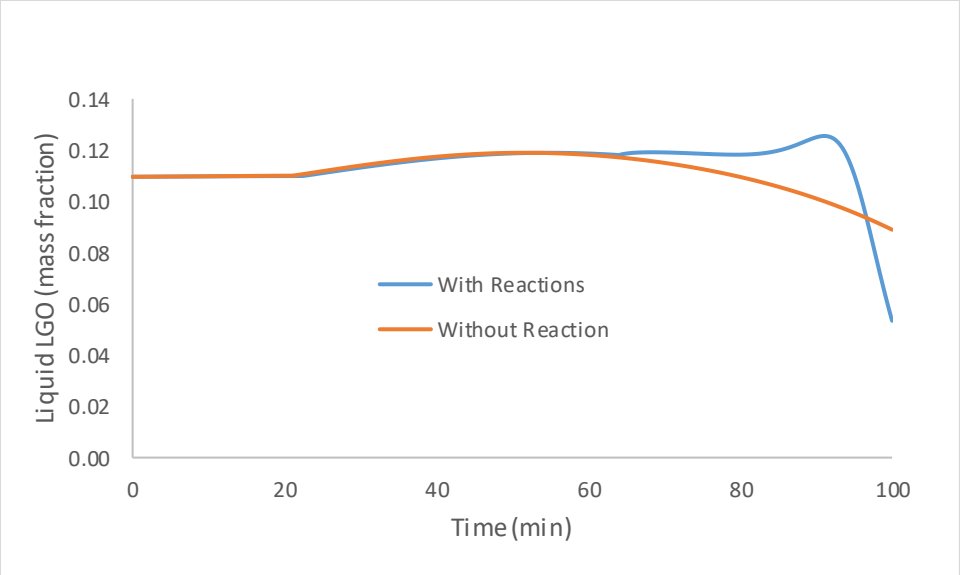

Figure 8.2.25: Liquid phase LGO mass fraction versus time with and without thermal cracking reactions – Dilbit sample (CDB).

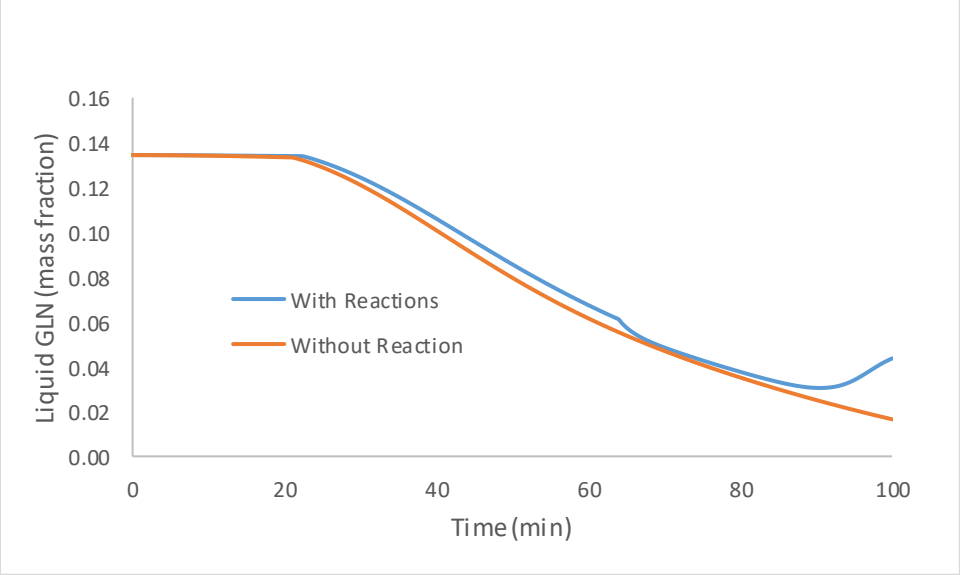

Figure 8.2.26: Liquid phase GLN mass fraction versus time with and without thermal cracking reactions – Dilbit sample (CDB).

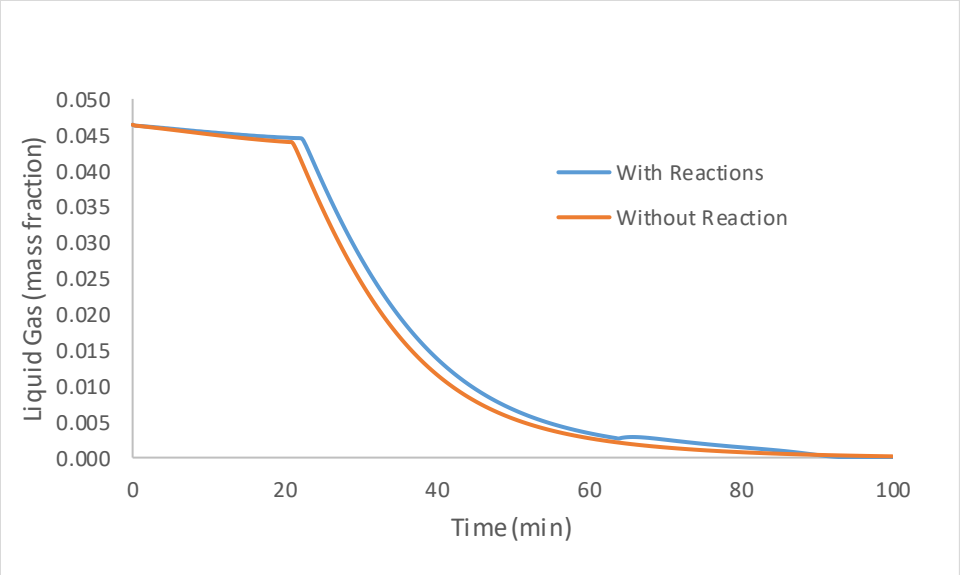

Figure 8.2.27: Liquid phase Gas mass fraction versus time with and without thermal cracking reactions – Dilbit sample (CDB).

The primary objective for this phase of work was to (1) generate the necessary comparative modeling results under conditions with and without the inclusion of thermal cracking reactions and (2) use these results to determine whether reactions significantly impact tank car performance under typical fire conditions. Although there were certain limitations on the initial tank car model conditions, along with upper bounds on applicable temperature for reactions, it is believed that these objectives have been adequately addressed. Key conclusions include:

1) Thermal cracking is somewhat insignificant below tank car lading temperatures of ~425°C and could largely be excluded from analyses where this temperature is not exceeded.
    a. This result is based on rates of thermal cracking for a medium crude, a heavy synthetic, and a dilbit. Special attention should be paid when applying this 'rule of thumb' to other crudes.
    b. Based on previous work, tank car temperatures above 425°C are only expected to occur when adequate insulation is not present (e.g., bare tank or uninsulated areas) and will be further discussed in Section 8.5.
2) Depending on the type of crude oil, bare shell tank scenarios are possible where the PRVs are undersized leading to system over-pressurization.
    a. Generally, it was observed that crude oils with higher liquid phase 'Residue' and 'VGO' lumps resulted in more stable system performance, particularly below thermal cracking temperatures
    b. The rate of 'Residue' and 'VGO' cracking to lighter lumps (primarily 'LGO') versus the rate of vapourization of these lighter lumps dictates whether over-pressurization will occur – e.g., if the rate of 'LGO' production is greater than the maximum possible rate of PRV venting at a temperature where 'LGO' in the vapour phase is favoured *via* VLE, over-pressurization will occur.

8.3 2-D CFD Tank

The CFD results for average heat flux (total heat flow divided by inside surface area of the shell) transferred to the lading versus time are shown in Figure 8.3.1 for the light crude oil, L1. In this case, the fire is perfectly emitting and its temperature is 815.6°C, the tank external surface emissivity is 0.9, and the initial lading temperature is 46.1°C. These conditions correspond to the Transport Canada standard TP14877, "Containers for Transport of Dangerous Goods by Rail", Section 8.2.7.2 – System Survivability and Thermal Analysis, where the fire temperature is that specified for pool fires. The initial liquid fill was set to 95% by volume (although, as discussed in Section 8.1, the light crude oil, L1, could be filled to 97% based on total mass).

The two extreme cases of a bare tank and a tank with ½-inch thermal protection are shown. Although bare tanks are no longer allowed in flammable lading service, this case is useful in studying and illustrating this extreme. Similarly, the thermally protected case presumes that no damage or degradation of the thermal protection occurs for the entirety of the simulation, which may not be true in real accident scenarios.

The bare tank heat transfer rate reaches 60 kW/m^2 within ten minutes for this light crude oil. For comparison, the maximum fire output at 815.6°C is approximately 80 kW/m^2 (the highest value of the y-axis in Figure 8.3.1), so the lading is very effective at absorbing heat from the fire. The thermally protected tank, on the hand, reaches only 5 kW/m^2 within 20 minutes. Recall, from Section 3, that this heat transfer rate is governed by the ½-inch thermal protection. Indeed, the heat flux allowed by a ½-inch thermal protection layer with thermal conductivity 0.08 W/(m·K) is 5 kW/m^2. Thus, Figure 8.3.1 illustrates the dramatic difference in heating rate between bare and thermally-protected tanks. It is clear that the thermal protection should be effective when present, intact, and functioning correctly and, if not, this light crude oil, L1, is capable of absorbing most of the heat flux emitted by the fire.

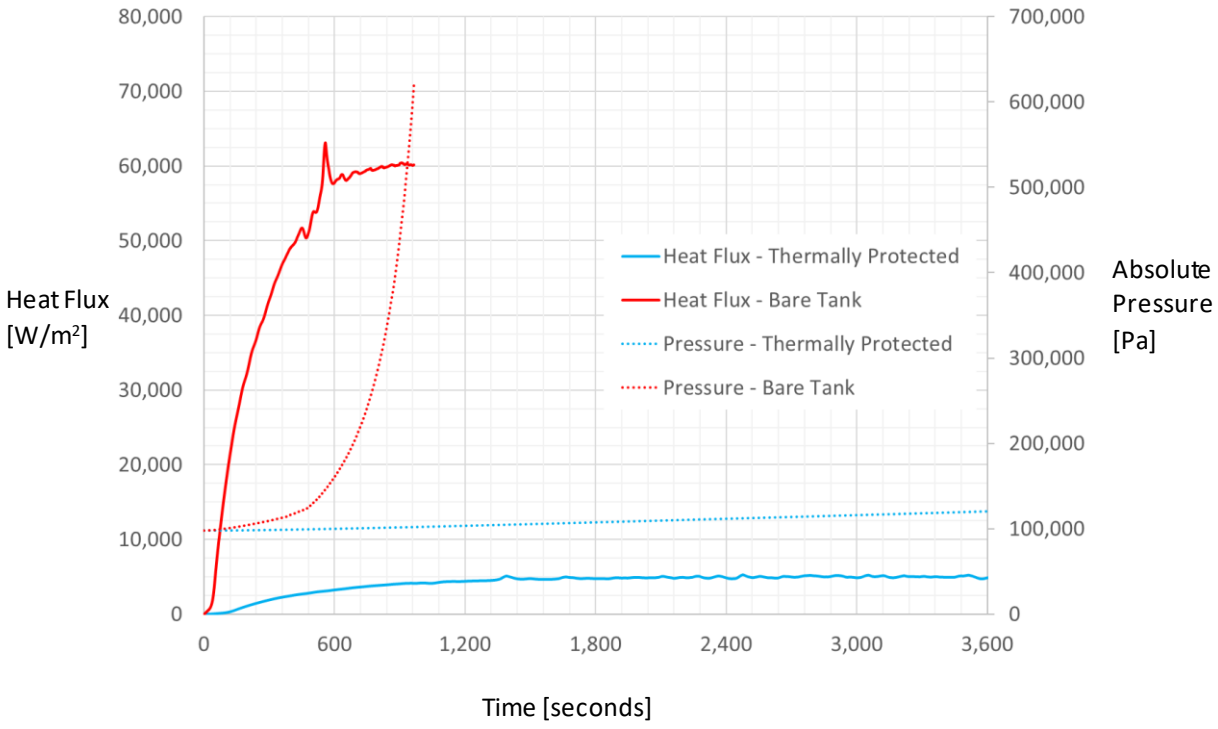

Figure 8.3.1: Average heat flux to the lading and tank pressure versus time for the light crude oil, L1.

Figure 8.3.1 also provides the tank pressure as calculated by the CFD simulation, showing the dramatic difference in pressurization rate between the bare tank case and the thermally protected case. The bare tank reaches the relief pressure (85 psig) within about 15 minutes (900 s) whereas the thermally protected tank has not even come close to the relief pressure after one hour (3600 s). Note that the pressurization occurs in the 2-D CFD simulation solely because of the thermal expansion of the oil. Examination of the oil saturation curves (Figure 8.1.2), for the peak temperature in the tank when the relief pressure was reached, revealed that very little to no evaporation would have occurred prior to first pressure relief for the cases studied.

Figure 8.3.2 provides the flow speed and temperature distribution inside the bare tank near the time the relief pressure was reached. Free convection causes the oil temperature to be highest near the top of the tank, adjacent to the gas head space.

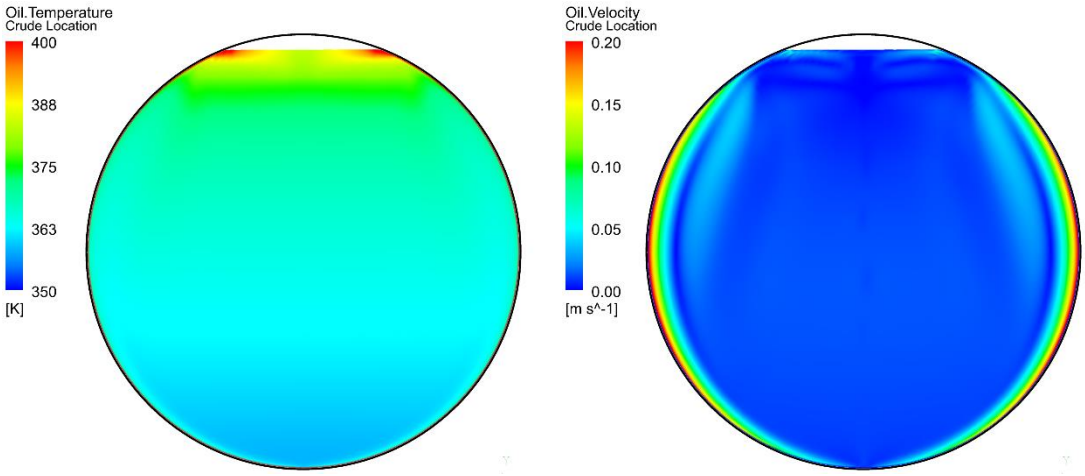

(a) (b)

Figure 8.3.2: (a) Temperature [K] and (b) flow speed [m/s] inside the bare tank for the light crude oil, L1, near the time the relief pressure was reached

The temperature versus time of the steel shell is provided in Figure 8.3.3, showing the average as well as indicating the temperature range with vertical bars, for the light crude oil, L1. Again, the fire is perfectly emitting and its temperature is 815.6°C, the tank external surface emissivity is 0.9, and the initial lading temperature is 46.1°C. The average steel temperature of the bare tank reaches a plateau that is approximately 250°C higher than that of the thermally protected tank. The peak steel temperature of the bare tank reaches close to that of the fire within about ten minutes, whereas the peak steel temperature of the protected tank takes an hour to reach approximately 350°C, although it is continuing to rise.

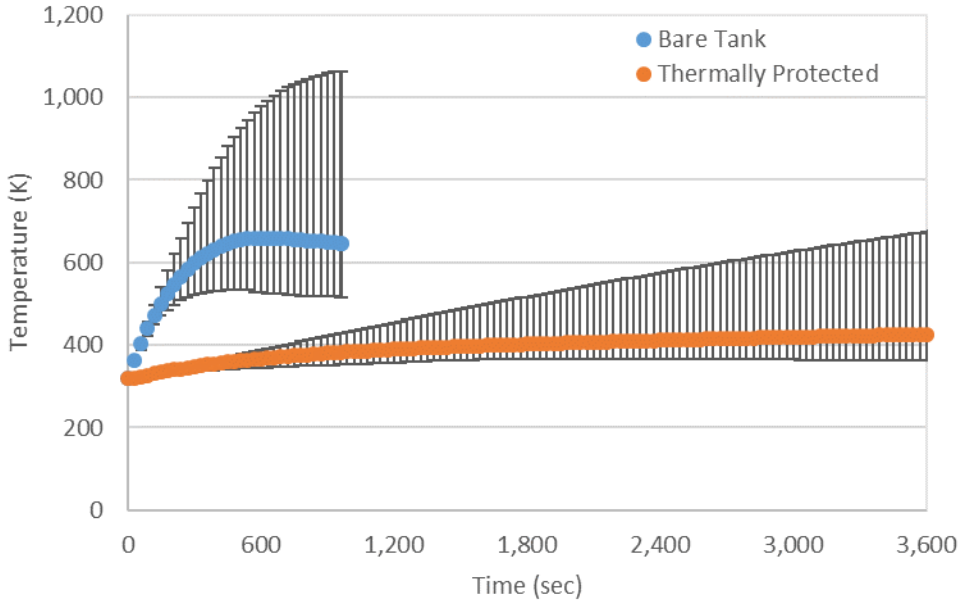

Figure 8.3.3 Steel temperature versus time for the light crude oil, L1. The points indicate the average temperature and the vertical bars indicate the temperature range.

Figure 8.3.4 explains the large steel temperature range, in this case for the thermally protected tank, by revealing that the high steel temperatures are found at the top of the tank, where the tank is in contact with the headspace. The adjacent gas or vapour space is not capable of providing significant convective cooling, and the cross section of the steel is too thin to conduct heat away effectively. Therefore, despite the thermal protection slowing heat transfer significantly, the steel adjacent to the gas headspace can, over the period of an hour or more, rise to hundreds of degrees Celsius. The highest steel temperatures for the bare tank are also found at the top of the tank adjacent to the gas headspace.

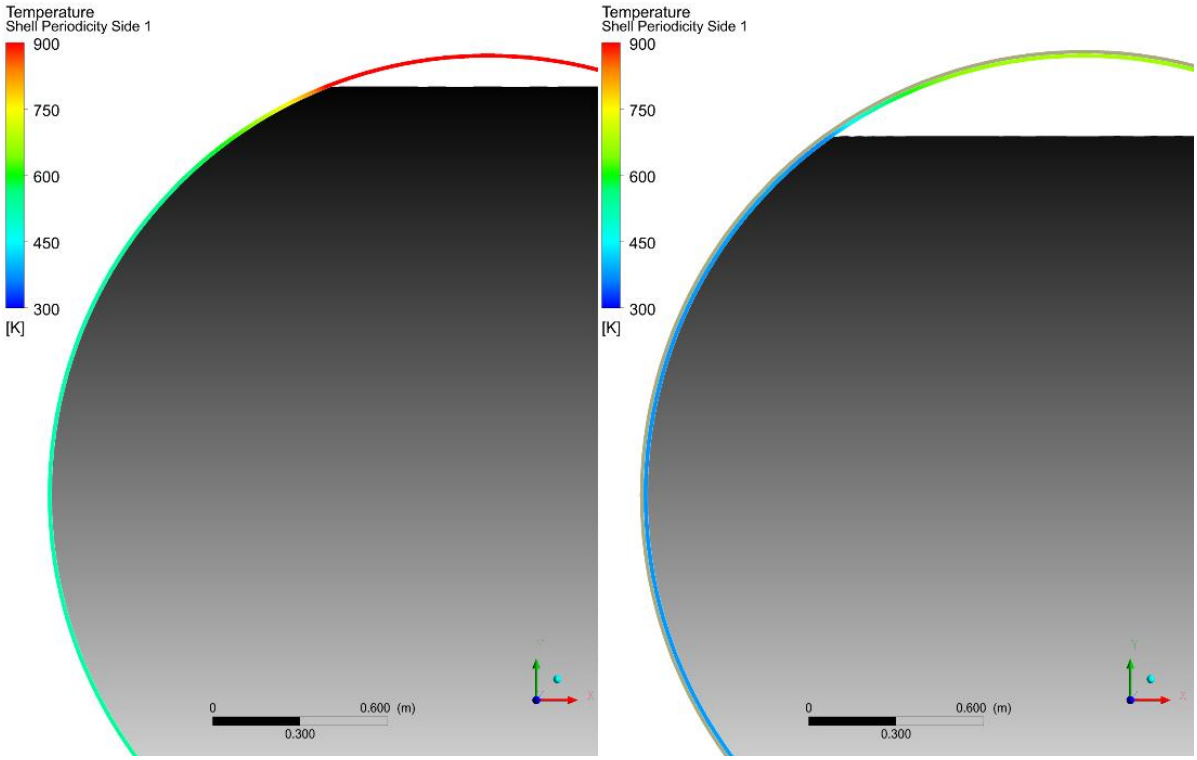

(a) (b)

Figure 8.3.4.: The steel temperature [K] for the light crude, L1, case. The liquid in the tank is indicated by the grey/black colour. (a) Bare tank at first pressure release (Time: 965 s) (b) Thermally protected tank at 1 hour.

The peak steel temperature is likely somewhat overestimated here since radiation was not included in this calculation and radiation would enable the inside surface of the shell to transfer additional heat to the somewhat cooler liquid surface. However, the effectiveness of this pathway would be limited because the headspace is small. In addition, heat transfer through the gas space to the top of the liquid would not drive further convection because this liquid is already at the top. Free convection is driven by warmer, less dense fluid being lower in the tank. Therefore, the radiant heating effect would be localized to the top layer of the liquid.

Figure 8.3.5 provides the heat flux to the lading versus time for two additional, thermally protected cases, one with the light medium crude, LM2, and the other with the condensate, C1. The fire temperature in this case is 900°C (for which the maximum fire output is approximately 100 kW/m^2) and the initial lading temperature is 25°C. The initial fill level is 95%, although the fill level does not come into play, as the tank does not pressurize significantly because of the thermal protection. The heat flux rate reaches approximately 7 kW/m^2, governed by the thermal protection as expected. The light medium crude takes about 40 minutes to reach this heat flux plateau whereas the condensate only takes about 15 minutes. The higher viscosity of the light-medium crude impedes free convection more. (Although not directly comparable because of the different fire conditions, recall that the light crude oil, L1, reached 5 kW/m^2 in

approximately 20 minutes.) Naturally, the same type of behavior in terms of ramp-up time has been found to occur for bare tank cases, with the additional characteristic that the plateau heat transfer rate for bare tanks depends on the lading type, less viscous crudes reaching a higher plateau.

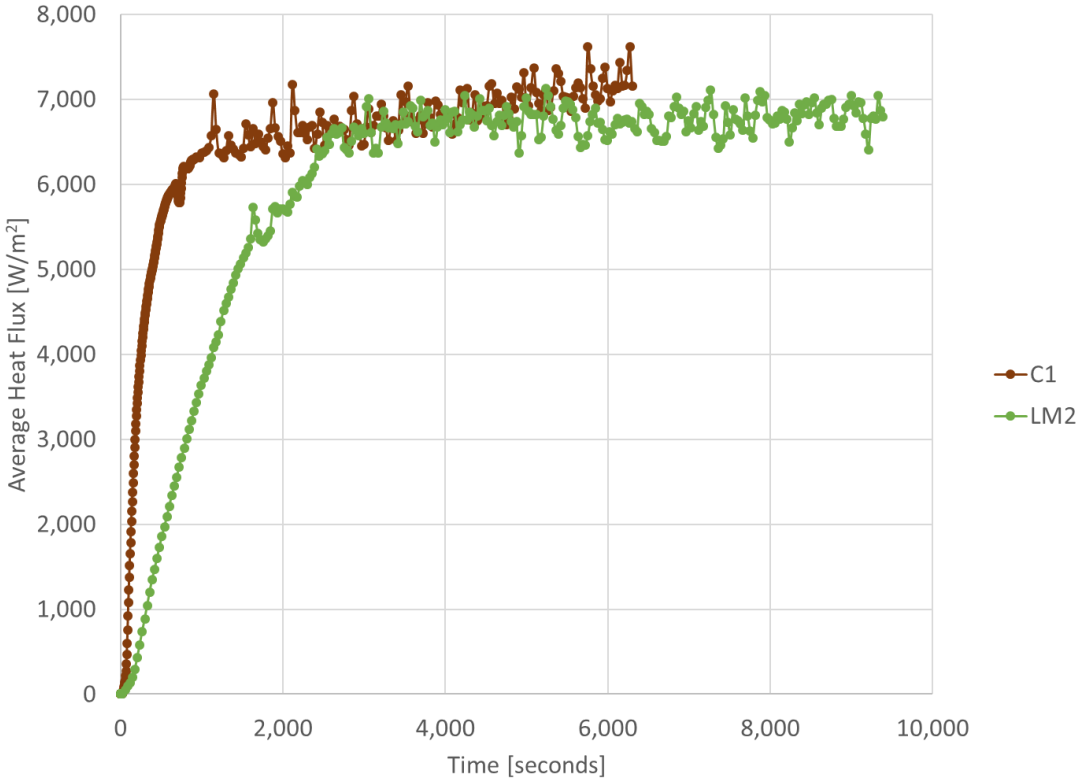

Figure 8.3.5: Average heat flux to the lading versus time for two thermally protected cases involving the condensate, C1, and the light medium crude oil, LM2.

Figure 8.3.6 provides the corresponding average steel temperature and the temperature range versus time for the two thermally protected cases, one with the light medium crude, LM2, and the other with the condensate, C1. Again, the fire temperature is 900°C and the initial lading temperature is 25°C. The average steel temperature depends on the type of lading, the less viscous lading resulting in higher average steel temperature. The peak temperature, however, does not depend on the type of lading, as the temperature-time profile of the peak is the same for the condensate as for the light medium crude. This lack of dependence of peak steel temperature on lading type is a consequence of the steel being adjacent to the gas space, not the liquid.

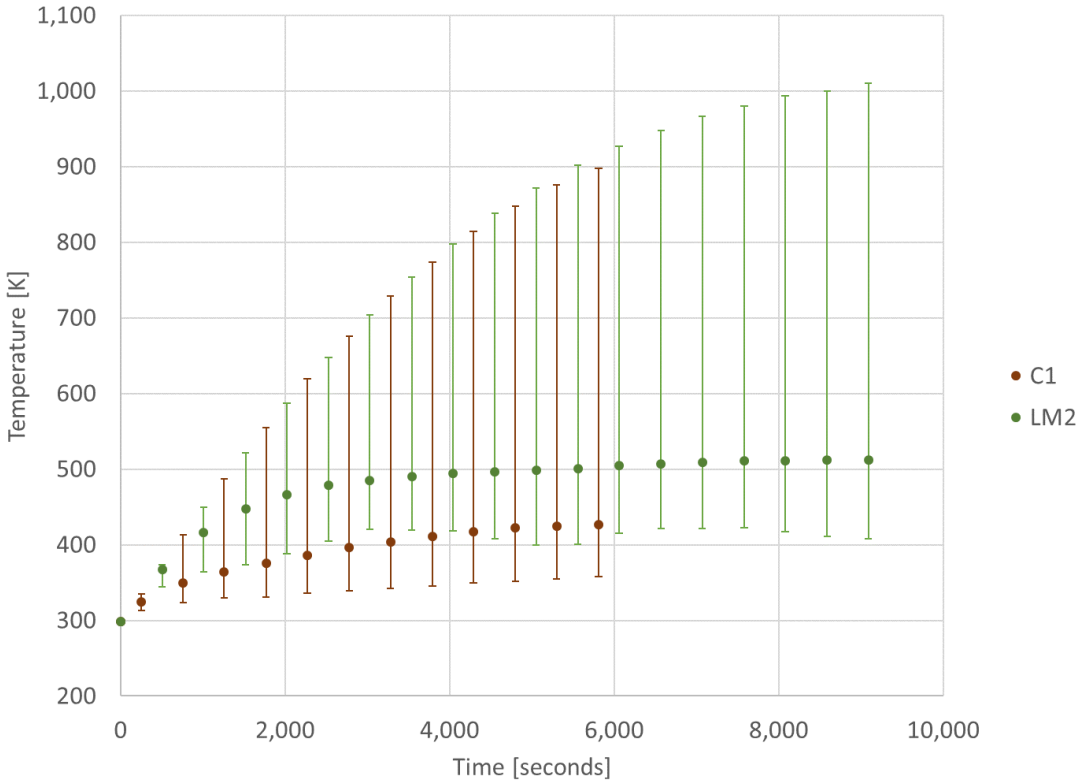

Figure 8.3.6: Steel temperature versus time. The points indicate the average temperature and the vertical bars indicate the temperature range. Both cases are thermally protected.

8.4 3-D CFD Pressure Release Valve

The pressure relief CFD results are provided in Table 8.4.1. For the unblocked valve, the gas discharge coefficient was found to be constant at approximately 0.72 and the liquid discharge coefficient was found to be constant at approximately 0.60. A 20% blockage caused no significant reduction in liquid discharge coefficient. A 50% blockage reduced the liquid discharge coefficient to 0.47 for the two crude oils simulated. An 80% blockage reduced the liquid discharge coefficient to 0.17 for the simulated crude oil.

Unlike in the 2-D CFD tank model, the flow behavior of the liquids through the PRV was not significantly affected by viscosity. This flow is much faster and driven by high pressure whereas the gentler free convection flow inside the tank was slower and driven by thermal expansion.

Table 8.4.1: PRV results. All tank pressures are 85 psig. The Volume Relief Rate is the Mass Flowrate divided by the Density in Tank.

Parameters					CFD Results		Analysis		
Crude Oil	Liquid or Gas	% Blockage	Temp in Tank [°C]	Density in Tank [kg/m^3]	Mass Flowrate [kg/s]	Outlet Velocity [m/s]	Volume Relief Rate [m^3/s]	Ideal Mass Flowrate [kg/s]	C_d [-]
Air	Gas	0	120	6.11	5.61	470.5	0.92	7.80	0.72
L1	Liquid	0	40	784.0	102.8	36.8	0.13	182.5	0.61
L1	Liquid	0	120	721.1	100.1	38.3	0.14	175.1	0.62
L1	Gas	0	120	12.6	7.04	359.0	0.56	9.63	0.73
LM1	Liquid	0	120	742.7	98.4	37.5	0.13	177.7	0.60
LM1	Liquid	50	120	742.7	76.3	32.0	0.10	177.7	0.47
MS1	Liquid	0	40	851.0	105.4	34.9	0.12	190.2	0.60
MS1	Liquid	0	120	790.0	99.8	36.1	0.13	183.3	0.59
MS1	Liquid	20	120	790.0	101.4	36.7	0.13	183.3	0.60
MS1	Liquid	50	120	790.0	78.8	31.1	0.10	183.3	0.47
MS1	Liquid	80	120	790.0	29.6	28.3	0.04	183.3	0.17

Table 8.4.1 also provides a comparison of air and crude oil flowrates and their consequent pressure relief of the tank. Comparing “Mass Flowrate”, the flow of liquid is much more efficient at emptying mass from the tank compared to the flow of gas. On the other hand, comparing “Volume Relief Rate”, volume occupied by gas in the tank is relieved much more rapidly than volume occupied by liquid. Therefore, gas flow through the PRV is more effective at quickly reducing the tank pressure. When liquid is discharged through the PRV, it is expected that the PRV could remain open longer than for gas and a large mass of the lading could be discharged. This conclusion was supported by experimental observations discussed in Appendix A. Because the liquid being discharged is flammable and the tank is engulfed in fire, the possibility of liquid discharge presents a safety hazard.

In Section 5.5 – Fire Scenario Performance Modeling (see Table 5.5.2) – the discharge coefficient was a function only of whether gas or liquid was passing through the PRV and the "orifice diameter" was reduced to effect PRV blockage. On the other hand, in Table 8.4.1, the area of the discharge hole in the tank was kept constant and the effect of the percent blockage (the percent reduction of the valve exit area) was assigned to the valve discharge coefficient. There is a small difference between the two PRV descriptions in that, according to the CFD results for this PRV, the valve exit could be blocked (at least 20% but less than 50%) without reducing the flow, implying that the discharge hole in the tank could be the limiting factor up to a certain blockage, an effect not included in the other description.

8.5 HYSYS Fire Scenarios

Calibration Cases

A series of calibrations runs was required to ensure the HYSYS tank car model outputs were in alignment with those generated *via* CFD tank modeling. Since heat flux versus time and PRV performance data are

inputs to the tank car model, it was important to compare key system outputs, such as heat flux, temperature, and pressure profiles, and note any differences that might require attention.

Preliminary CFD results from three crude oil samples were used during calibration runs with the intention of trying to cover a wide of range of crude oil types that are also required as part of the main fire scenario modeling work. For these reasons a light (FL178), light-medium (FL061), and medium crude (MBL) oil were selected as the most representative samples. It should be noted that the calibration results for the light and light-medium crude samples are not discussed in detail here. It was determined that they follow the same trends and provide the same level of alignment with CFD modeling data as the medium crude sample, which is discussed in detail in this section of the report.

Figure 8.5.1 presents system heat flux versus time profiles for the medium crude (MBL) sample generated using both the CFD and Aspen HYSYS tank models. It can be observed the CFD heat flux profile has an initial rapid increase to ~50,000 W/m^2 followed by a slightly exponential increase up until the initial relief event (~1660 seconds). It should be noted that this calibration run was performed under higher flux conditions that represent non-thermally protected tank car scenarios. While this is not the situation for the majority of the fire scenarios explored in this work (see Table 5.5.1 to 5.5.3), the results of this calibration process can be directly applied to any set of CFD heat flux versus time profiles (when utilized).

To allow for input into the HYSYS tank model, the relatively complex heat flux curve was linearized as shown in Figure 8.5.1. Although the linearization fit is relatively good (R2 = 0.92), it should be noted that it under-predicts the heat flux up to approximately 300 seconds and over-predicts for the most part thereafter.

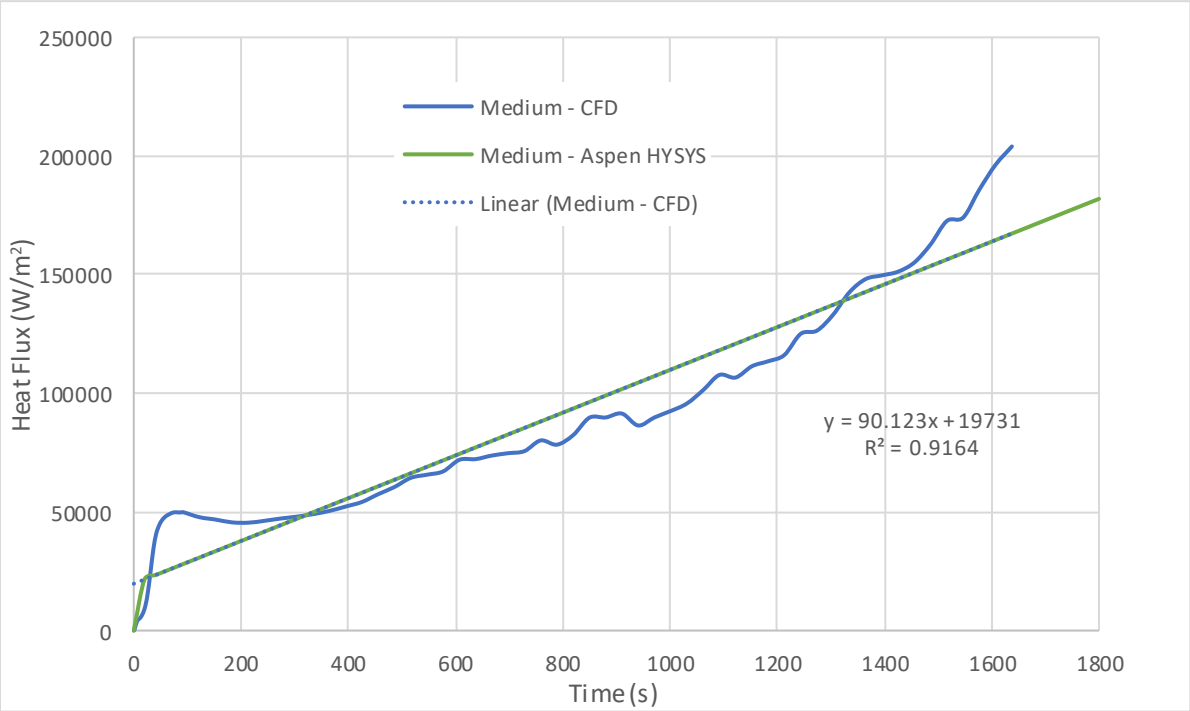

Figure 8.5.1: System heat flux versus time for CFD and HYSYS tank car models – Medium crude sample (MBL).

To determine whether the simplified heat flux profile method is an acceptable option, the average system temperature was examined. Figure 8.5.2 shows that the average system temperature versus time profiles for both CFD and HYSYS cases. Based on the results in this figure, there is a relatively good alignment between the two results, which suggests that the linearization method is acceptable and can be applied to main fire scenario cases. It is likely that the relatively small error between the results is caused by (1) the under- and over-prediction due to linearization and (2) the variance in lading heat transfer resistance between the two methods, where the Aspen HYSYS model assumes uniform heat distribution throughout the total tank car contents (i.e., no resistance to heat transfer).

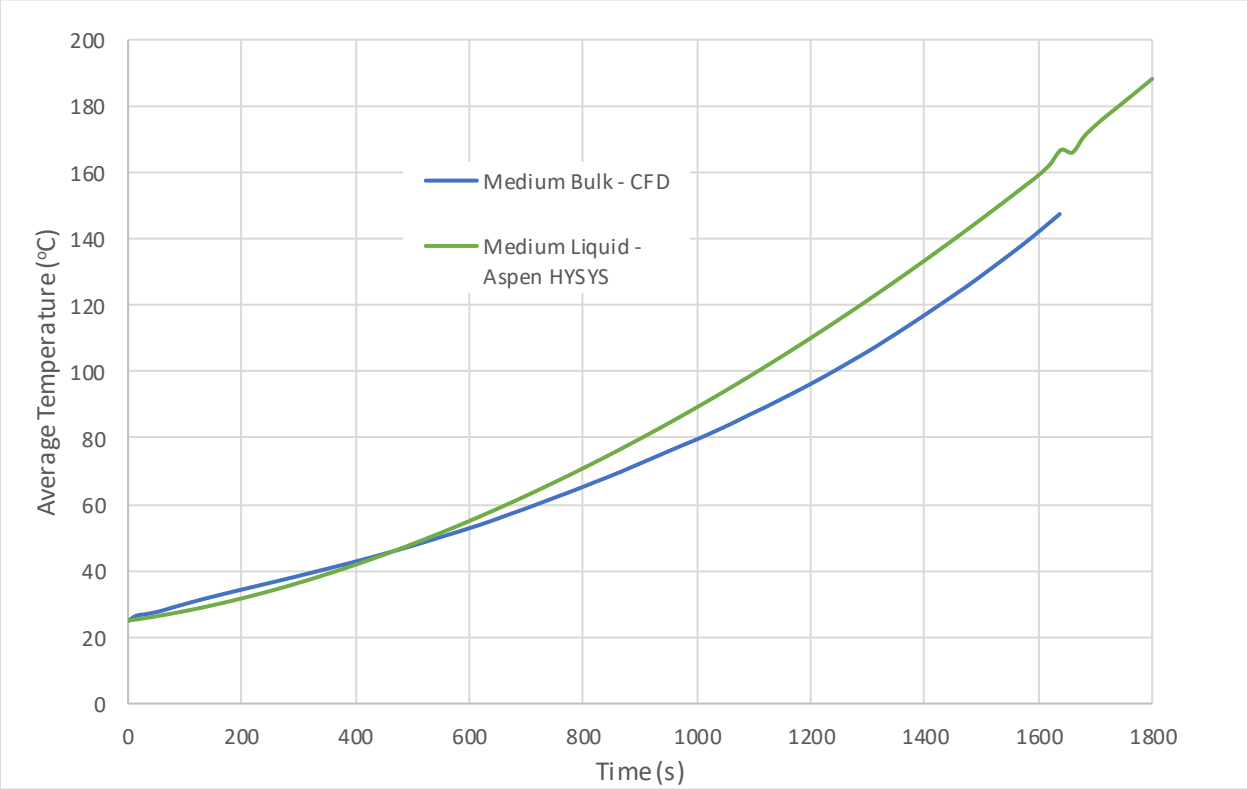

Figure 8.5.2: System average temperature versus time for CFD and HYSYS tank car models – Medium crude sample (MBL).

Knowing that the temperature versus time profiles were generally in agreement, the final calibration check between the two methods was the examination of the time at which the systems reach the first relief event. Figure 8.5.3 displays the system pressure versus time profile for both modeling cases and shows that initial relief event for each are in alignment (940 versus 980 seconds). However, a major inconsistency was observed: the pressure rise in the HYSYS case with a high recycle efficiency (High RE) is relatively linear with a rapid jump to the PRV relief pressure at ~940 seconds.

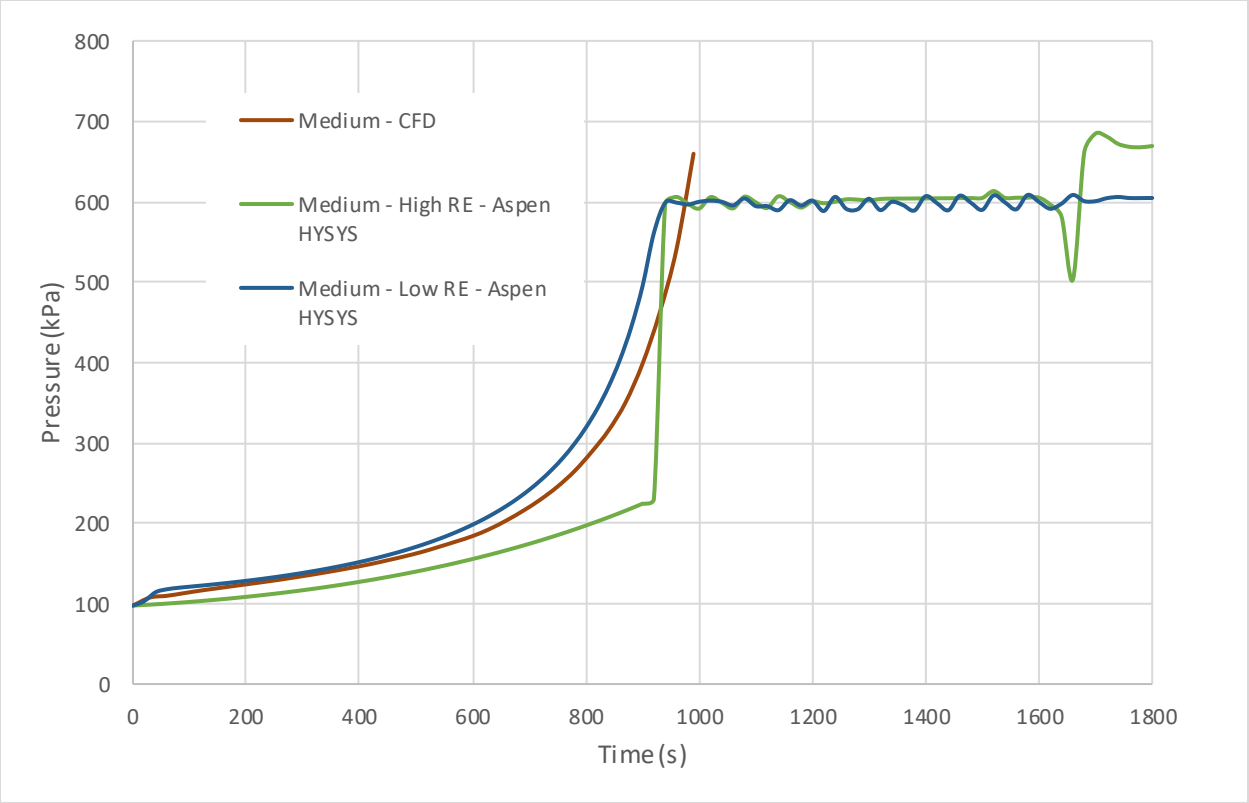

Figure 8.5.3: System pressure versus time for CFD and HYSYS tank car models – Medium crude sample (MBL).

In all cases, it was observed that initial relief event effectively coincided with the time that the system fill level reached 100% due to thermal expansion of the liquid phase (i.e., no vapour headspace remaining). This indicates that at high initial fill levels, thermal expansion is the primary driving force towards system venting, and not vapourization of the lighter hydrocarbons. To understand why the high recycle efficiency (RE) HYSYS case did not match the exponential pressure increase observed for the CFD case, a review of the liquid-vapour equilibria was performed. Although not explicitly shown in this report, it was observed that when considering vapour headspaces composed primarily of air, the light-ends have a drastically higher affinity towards the liquid phase. This explains why the system pressure does not increase as expected, even though the system is at elevated temperatures.

To test this theory, a second case was explored where the recycle efficiency was set to near zero (see Low RE curve on Figure 8.5.3). This represents a scenario where the vapour does not interact with the liquid, as is the case for the CFD modeling work. Under these specific conditions, it was observed that pressure profiles between the two models matched quite closely (940 versus 980 seconds to reach the relief pressure). While these results are promising from a modeling perspective, this brings up the issue of what to set the recycle efficiency to during the main fire scenario modeling runs. The liquid-vapour equilibrium is not only dependent on the thermo-physical properties of the lading, but also time and the available surface area for mass diffusion (i.e., the rate of mass diffusion). It could be argued that based on the relatively small surface area at high fill levels and high heating rates experienced in bare tank scenarios that the system would be far from equilibrium. On the other hand, some level of mass diffusion will

definitely be present, even if only close to the liquid-vapour interface. Therefore, it was decided that all main fire scenario-modeling cases would be run with a low (near 0%) recycle. While this does not fully address the equilibrium, it should provide tank car performance close to what would be expected from a "real-life" fire event.

Fire Performance Cases

The following section examines a series of potential tank car fire scenarios, using calibrated inputs from the tank car (Section 8.3) and PRV (Section 8.4) CFD modeling, to better understand the impact of several key variables, including:

1) Lading type and Reactions (Cases E18X, E2-E6)
2) PRV orientation (Cases E1, E7-E8)
3) PRV blockage (Cases E1, E9-E11)
4) Thermal protection (Cases E18X, E12)
5) Volatility (Cases 18X, E13-E15)
6) Fire temperature and tank emissivity (Cases E18X, E16-E22)
7) PRV set pressure and fill level (Cases E18X, E23-E25)
8) Fill level (Cases E18X, E24-E25)

One of the key steps in the work was the development of a HYSYS tank car model that uses radiative heat transfer boundary conditions (see Section 5 for details). Since there was no readily available experimental data for comparison, it was thought that the best approach for validation would be *via* the use of the highly developed CFD outputs. Figures 8.5.4 to 8.5.10 depict the system heat flux, average liquid and vapour temperature, pressure, liquid fill, and liquid and vapour mass versus time, respectively, for the baseline fire scenario (see Section 5.5) with (E18X) and without (E1) the use of the radiative boundary conditions. From these figures, several key conclusions can be drawn:

- Although there is an initial difference in heat flux profile (Figure 8.5.4), caused by heat transfer through the thermal protection (E18X) versus heat transfer directly to the lading (E1), the average heat flux over the entire case period is very similar.
    - This is further confirmed by noting the nearly identical curves for liquid temperature, liquid fill, liquid mass, and vapour mass (Figures 8.5.5, 8.5.8, 8.5.9, and 8.5.10, respectively).
    - Case E1 heat transfer data was taken from CFD work presented in Figure 8.3.1.
- Based on the results presented in Figure 8.3.4 in Section 8.3, Case E1 is under-predicting the average vapour temperature.
    - While this does not change the time of the initial PRV relief event (~240 minutes), as shown in Figure 8.5.7, it does change the pressure increase behaviour (exponential versus S-shaped).

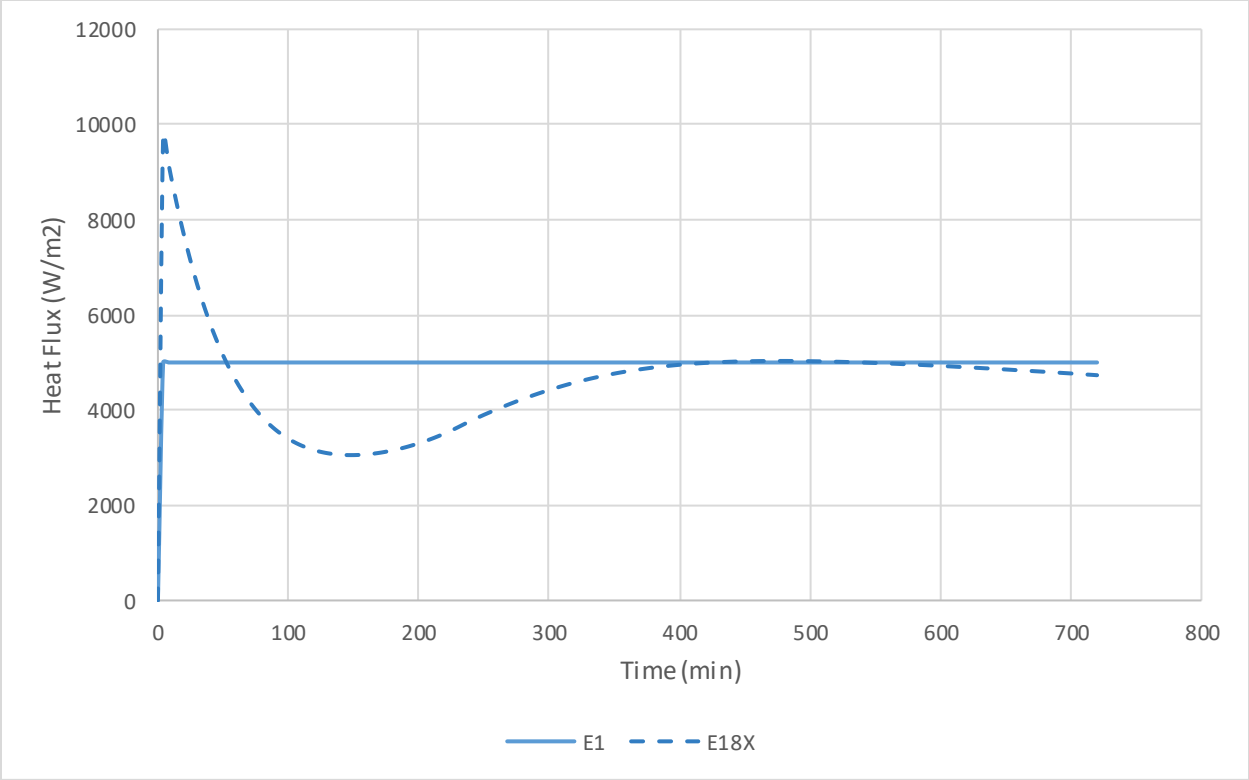

Figure 8.5.4: System heat flux versus time for Cases E1 and E18X.

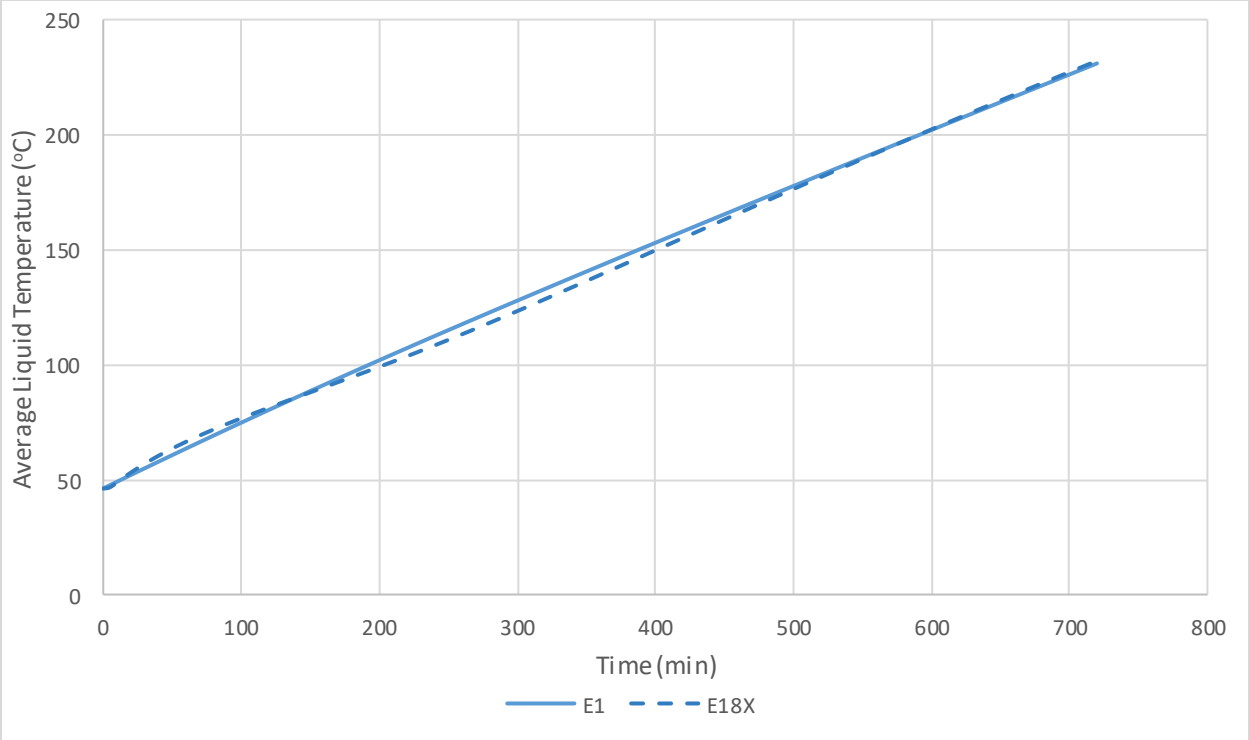

Figure 8.5.5: System average liquid temperature versus time for Cases E1 and E18X.

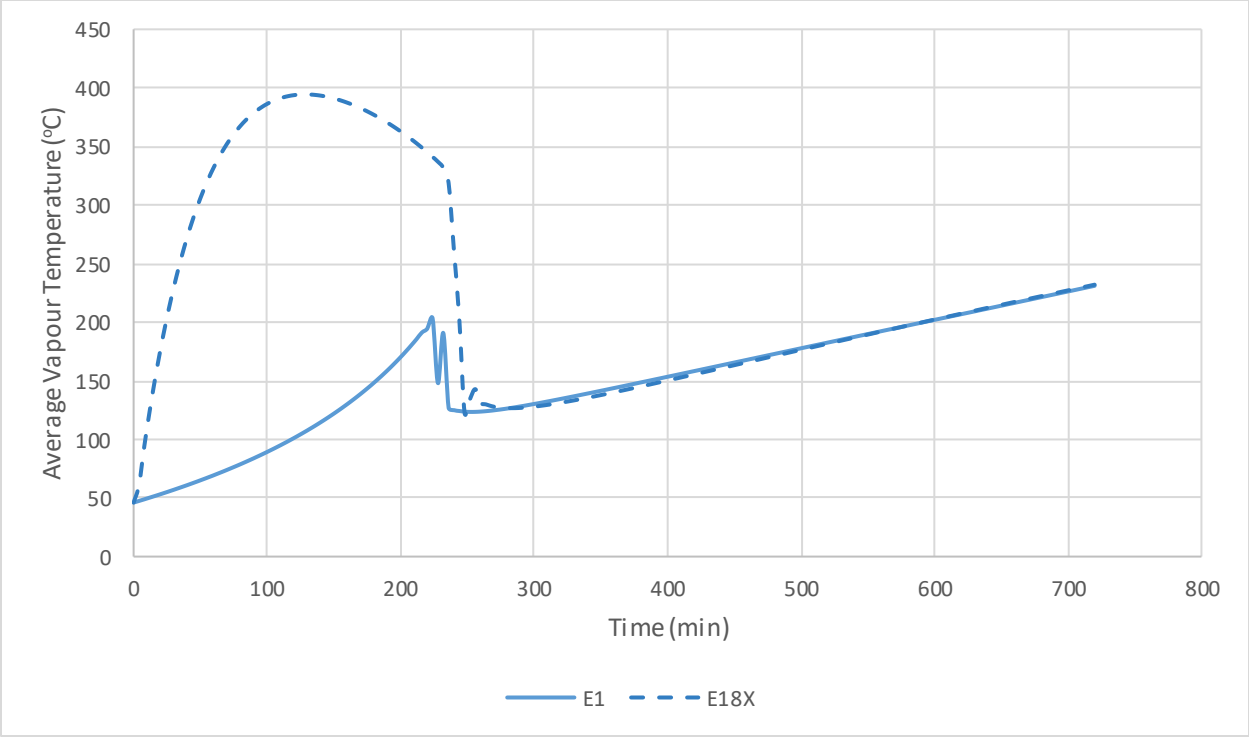

Figure 8.5.6: System average vapour temperature versus time for Cases E1 and E18X.

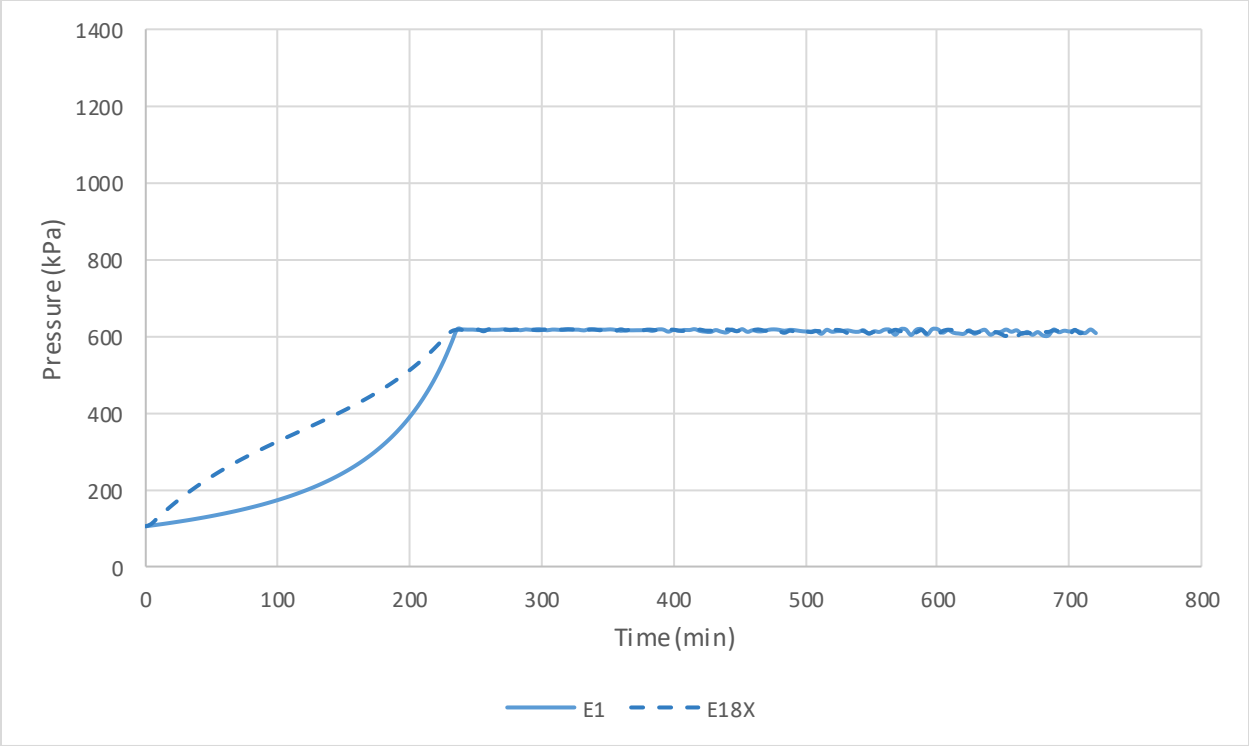

Figure 8.5.7: System pressure versus time for Cases E1 and E18X.

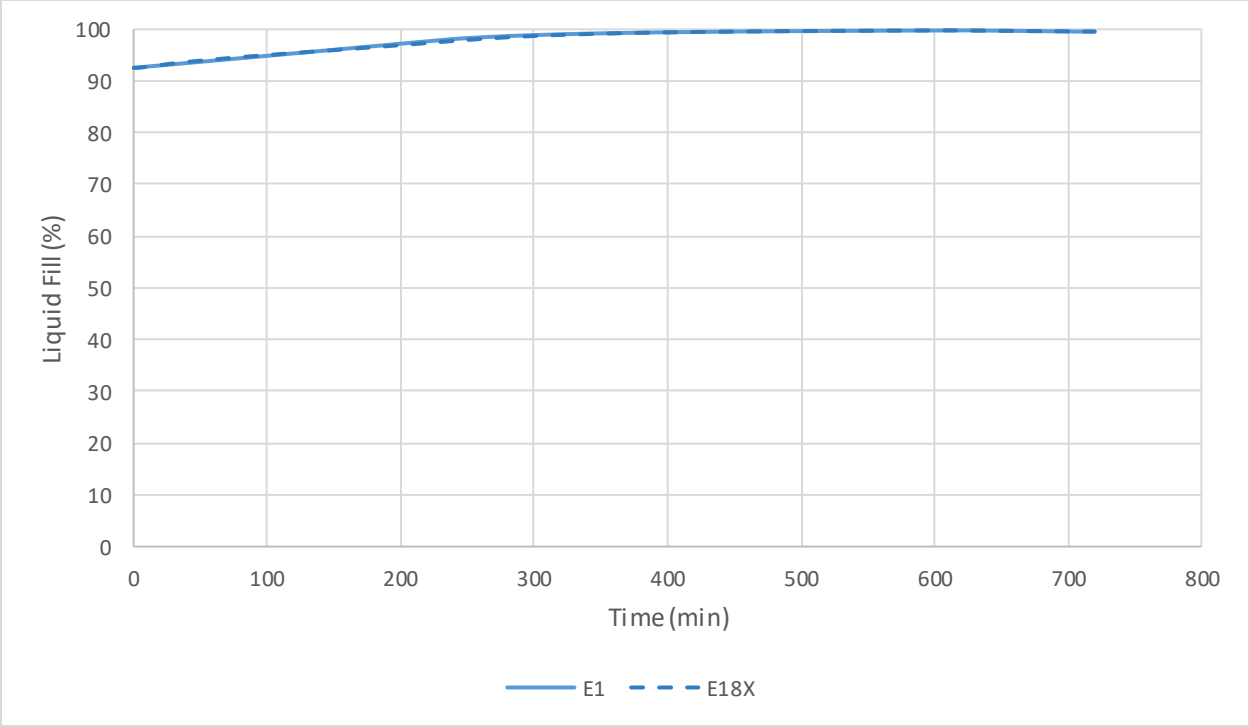

Figure 8.5.8: System liquid fill level versus time for Cases E1 and E18X.

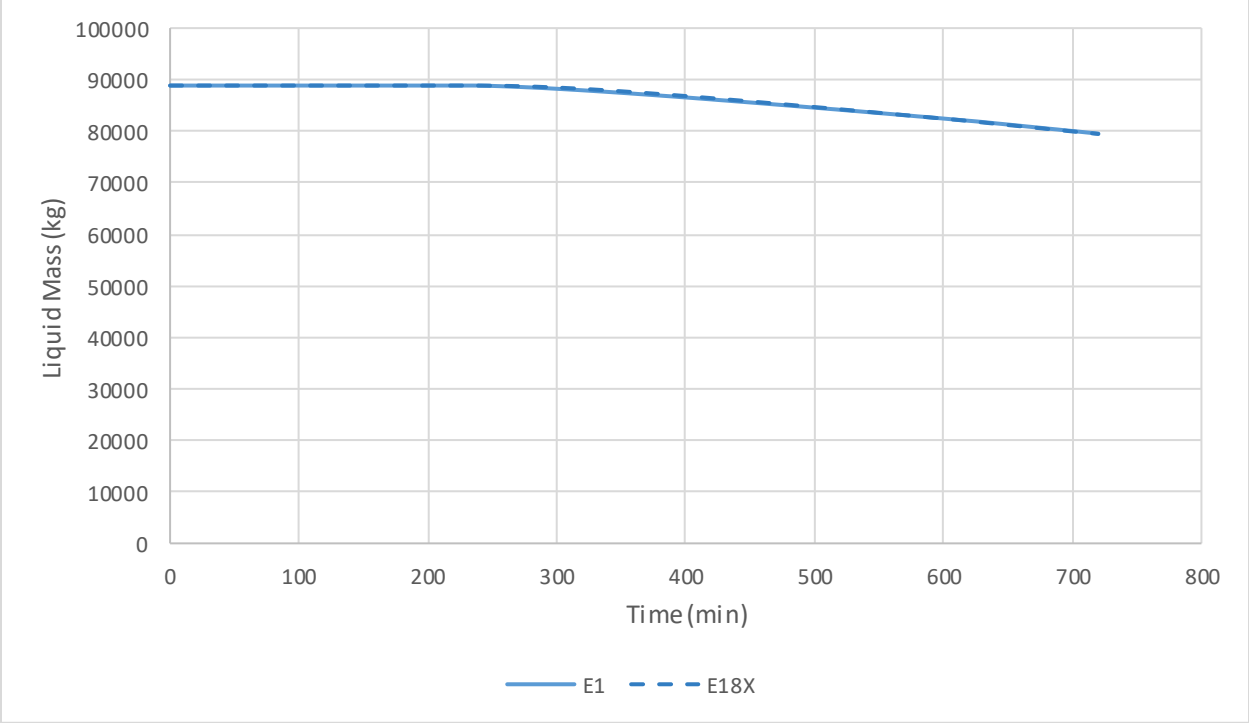

Figure 8.5.9: System liquid mass versus time for Cases E1 and E18X.

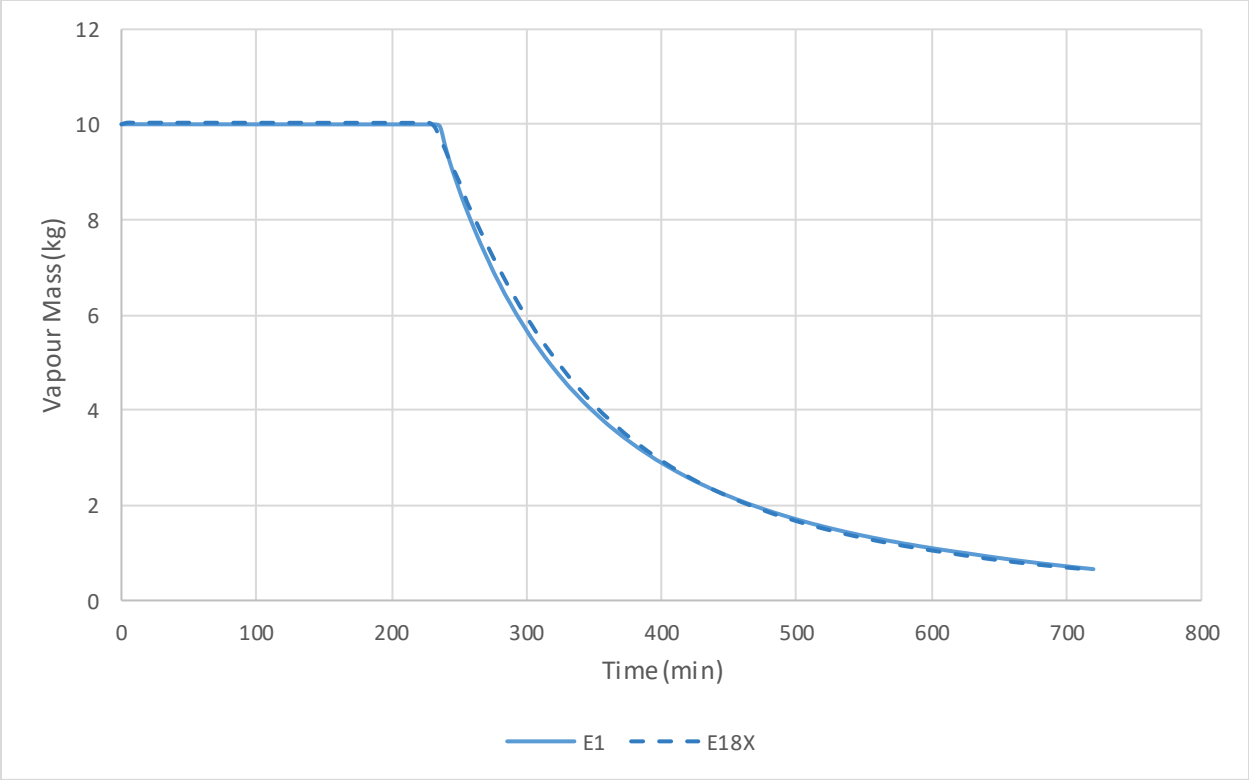

Figure 8.5.10: System vapour mass versus time for Cases E1 and E18X.

Moving forward, further comparisons to the baseline fire scenario are made with Case E18X as it is in the authors' opinion that it better represents a 'real life' scenario and provides more useful tank car integrity (pressure/temperature combination) data. The only exceptions are PRV orientation and blockage key variable comparisons, which ideally would use the radiative boundary condition if reassessed. However, since both these key variable are studied using a comparative method, the conclusions are still representative.

Lading Type and Reactions

Figures 8.5.11 to 8.5.14 present the system average liquid and vapour temperatures, pressure, and liquid fill level, versus time profiles, respectively, for the light (FL178), medium (MBL), heavy synthetic (AHS), condensate (FL126), and dilbit (CDB) samples, along with a case (E6) where thermal cracking reactions have not been considered. In each case, the initial fill level was set at its respective maximum based on gross tank weight guidelines (see Table 5.5.1), the PRV was in the upright position (0 degree), and the tank was thermally protected. It should be noted here that, similar to Section 8.2, scenarios with and without cracking reactions are again being explored. However, in this case, the tank car has thermal protection and will provide more useful performance results. Additional details about the scenario inputs to the HYSYS tank car model can be found in Section 5.5. The following list provides key comparative observations between the five samples and the impact of not considering mild thermal cracking reactions:

- In general, the lighter samples do not reach as high of liquid temperatures as the heavier samples.

- This is because the lighter samples begin to vapourize and vent earlier, thus removing heat from the system.

- The time required to reach the initial relief event varies between ~110 and ~575 minutes and increases for heavier crudes.
  - It appears as though this is a direct function of initial fill level; lighter oils can have higher fill levels without exceeding the maximum car weight.
- Although there are differences in rates of vapourization between the five crudes, the relatively high initial fill levels, combined with the low liquid temperatures, limit their influence on tank performance.
  - In these cases, liquid expansion is the dominant force.
- There are no discernible changes in tank car performance when cracking reactions are not considered (E6)
  - Even after extending the operating period to 1440 minutes (24 hours), the liquid phases are still below the minimum required temperature for reactions to process (~425°C) as discussed above.
  - It should be noted that this conclusion is likely invalid if the operating period was further increased and/or if the level of thermal protection was reduced.

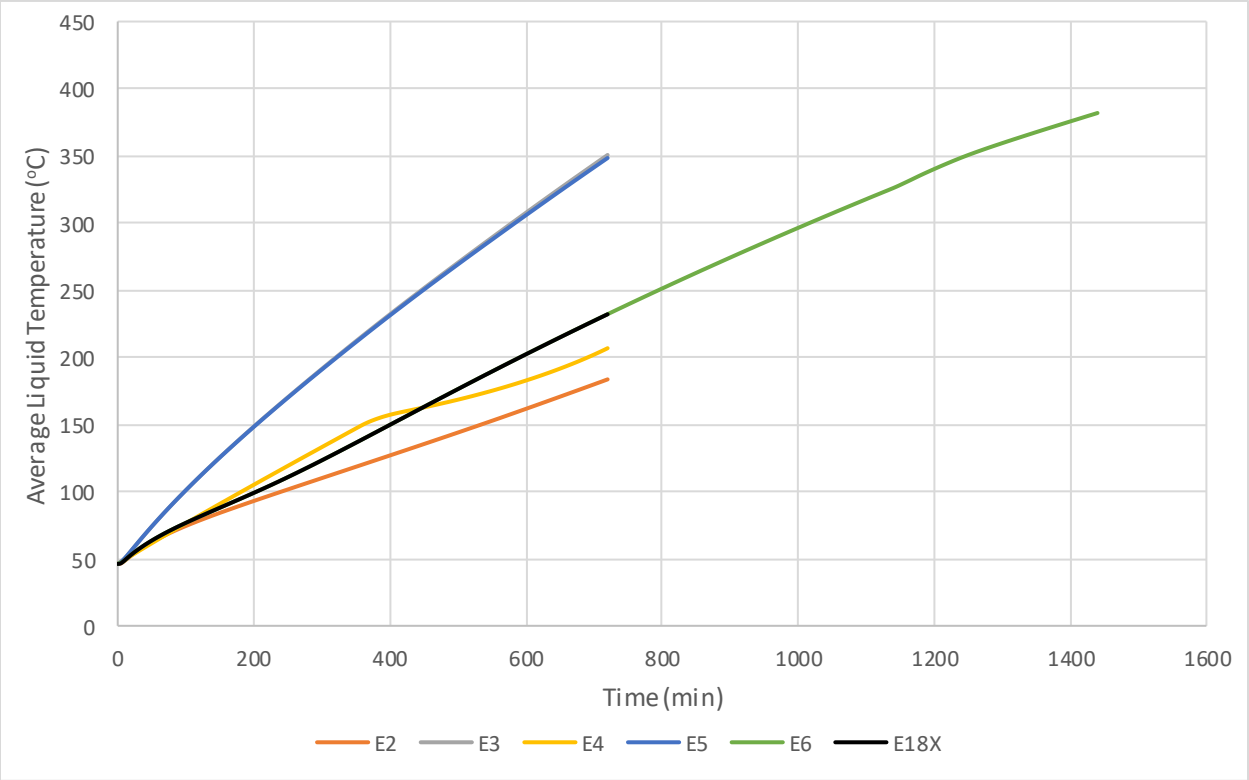

Figure 8.5.11: System average liquid temperature versus time for Cases E18X (base line) and E2-E6.

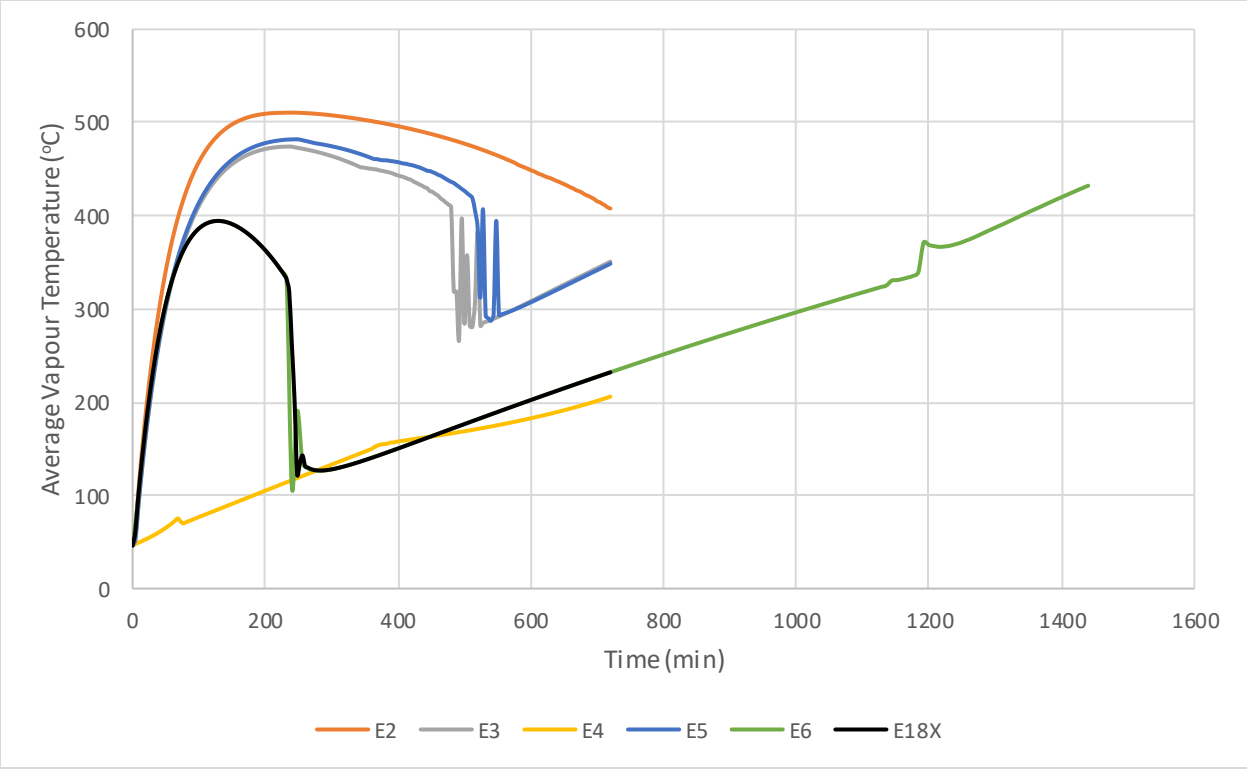

Figure 8.5.12: System average vapour temperature versus time for Cases E18X (base line) and E2-E6.

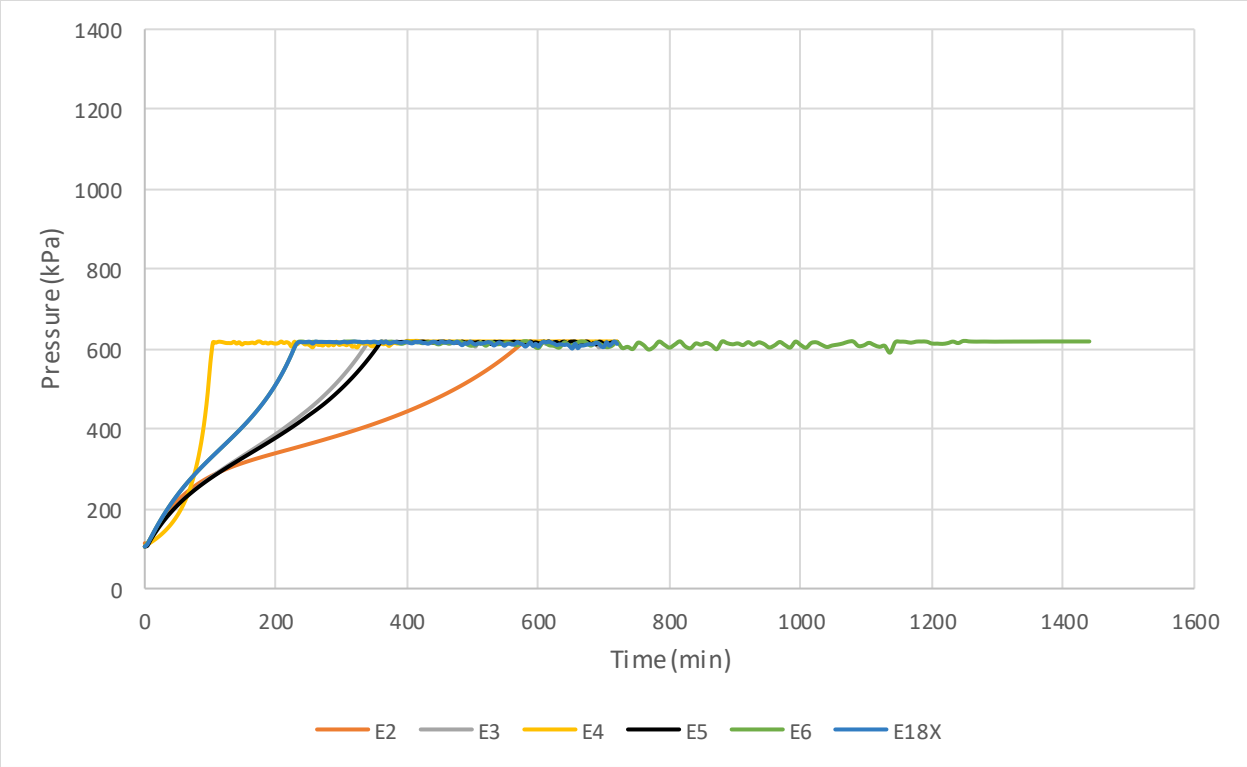

Figure 8.5.13: System pressure versus time for Cases E18X (base line) and E2-E6.

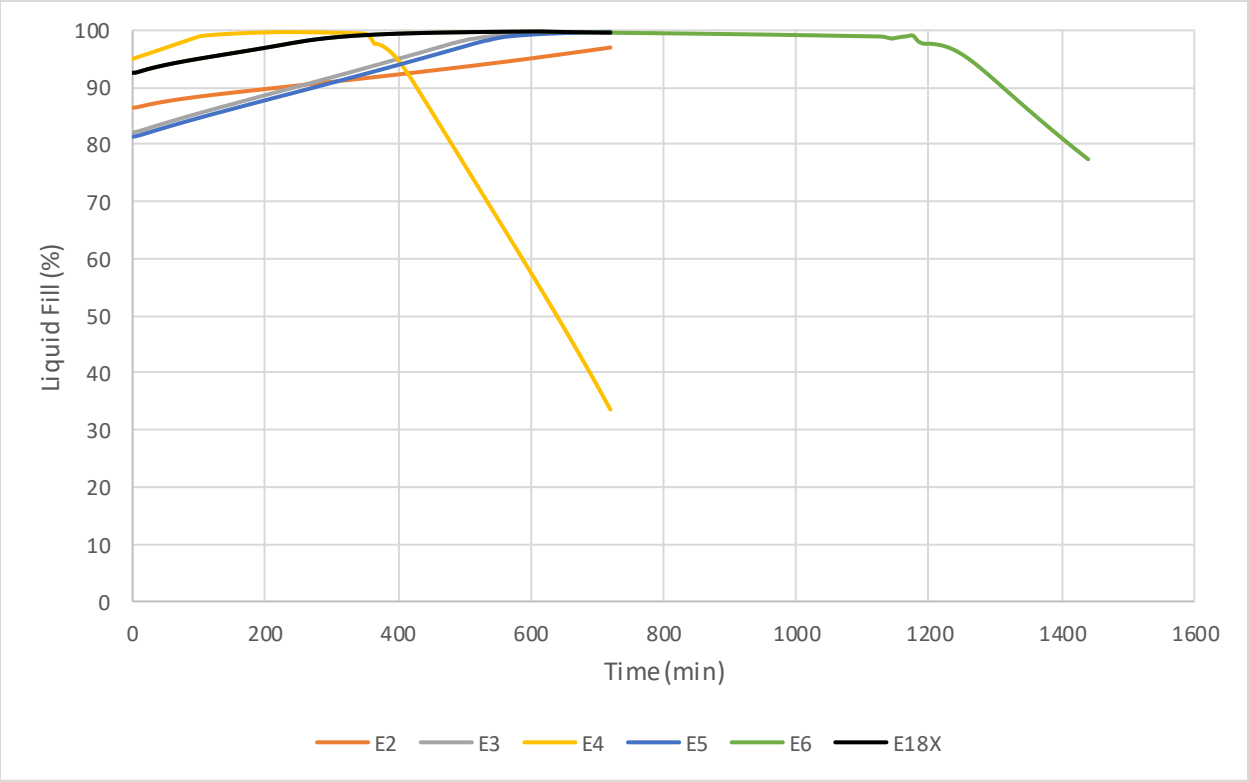

Figure 8.5.14: System liquid fill level versus time for Cases E18X (base line) and E2-E6.

PRV Orientation

Figures 8.5.15 to 8.5.20 present the system average liquid and vapour temperatures, pressure, liquid fill level, and liquid and vapour mass versus time profiles, respectively, for the light (FL178) sample with the PRV in three different positions: 0 degrees (E1), 45 degrees (E7), and 120 degrees (E8). Additional details about the scenario inputs to the HYSYS tank car model can be found in Section 5.5. The following list provides key comparative observations between the three PRV orientations:

- When looking at the system average liquid temperature, pressure, and liquid fill/mass it appears that there is very little change in system performance with change in PRV orientation.
    - The average liquid temperature profiles are nearly identical.
    - In all cases, the initial relief event happens at the ~240 minute mark and the system begins to vent at this point.
- While the overall performance in terms of temperature/pressure profiles is similar, the process by which pressure/venting is maintained is fundamentally different.
    - The performance is the same up to the initial relief event.
    - Based on the fill level (>92%), when the PRV opens liquid is vented from the system for cases E7 and E8, as opposed to vapour in base line case (E1).
    - Figure 8.5.20 shows that there is no initial decrease in vapour mass and the 'pocket' of vapour is maintained until the liquid level drops below the PRV height.

- It is noted that the liquid level (Figure 8.5.18) is maintained and does not continue to increase after the initial relief event, as is the case when vapour is vented.

- It can be concluded that the venting process is shifted from liquid vapourization/vapour venting to liquid expansion/liquid venting.
  - The venting of liquid could be problematic given it would likely be discharged into the surrounding fire.
  - In each case, the PRV appears to be appropriately sized and no system over-pressurization is observed.

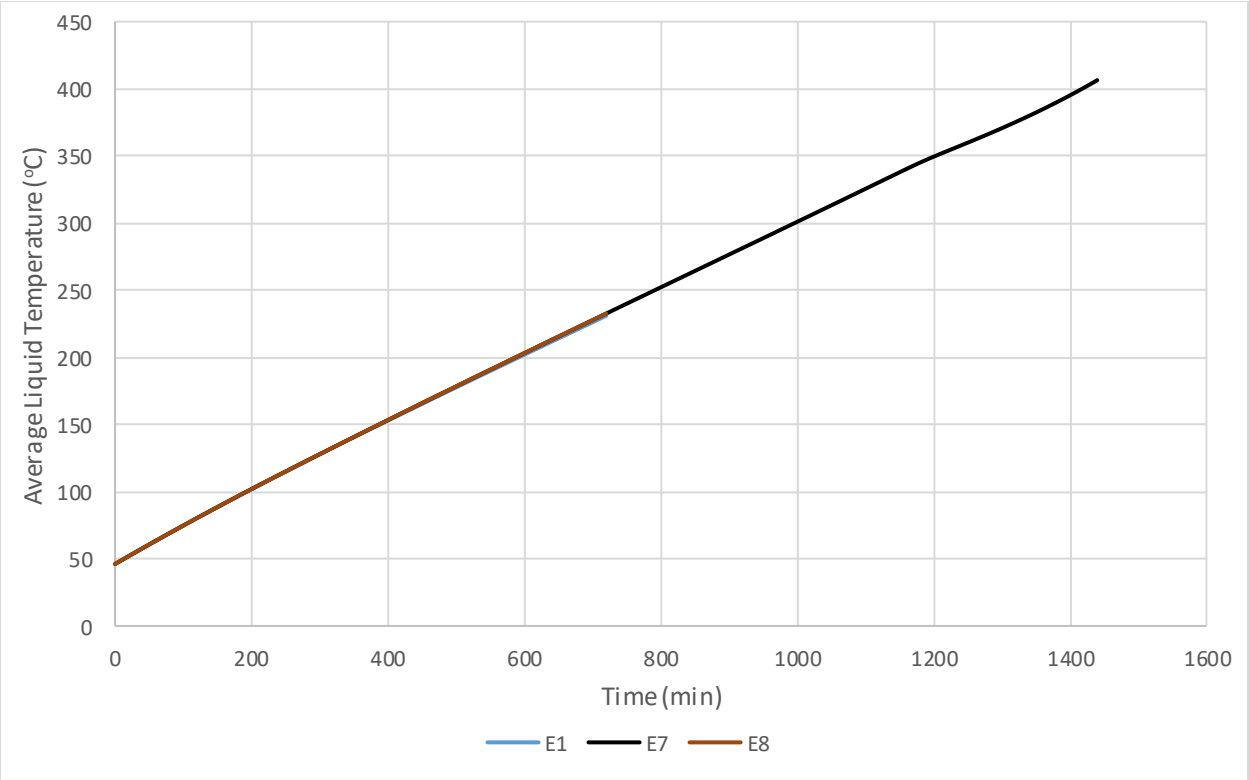

Figure 8.5.15: System average liquid temperature versus time for Cases E1 (base line) and E7-E8.

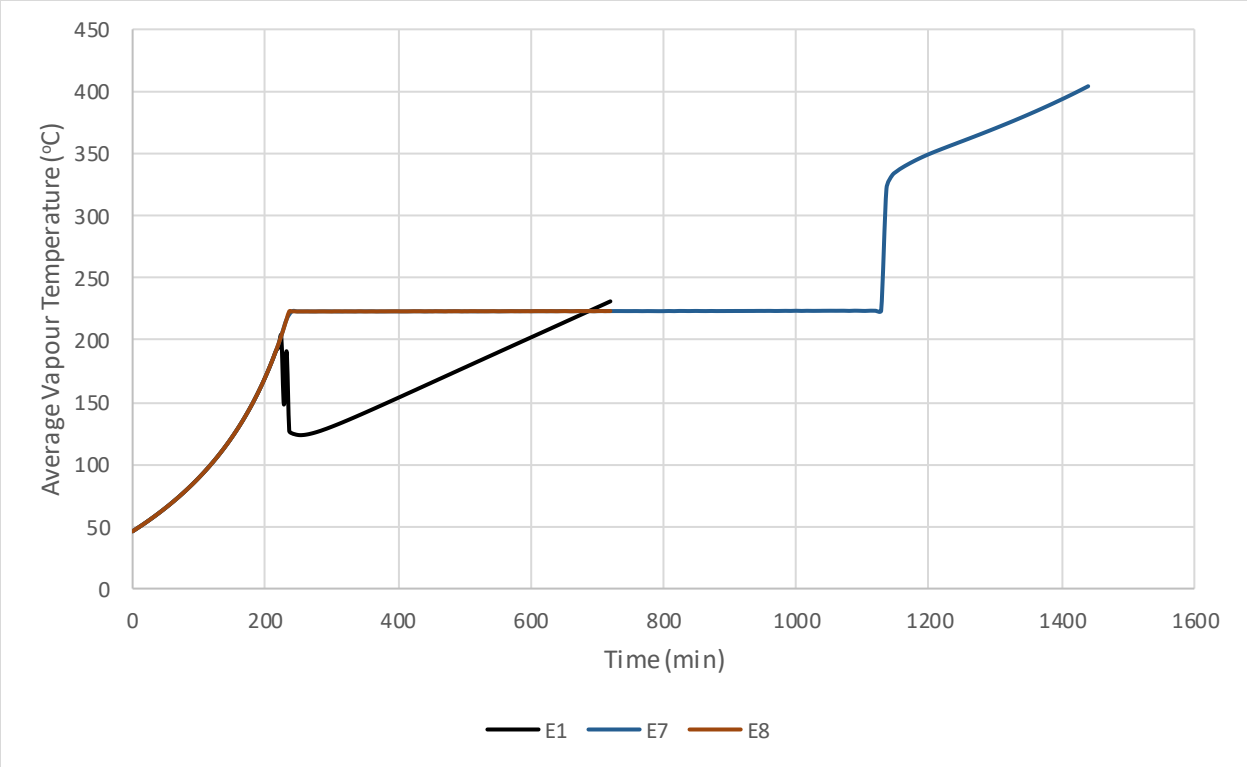

Figure 8.5.16: System average vapour temperature versus time for Cases E1 (base line) and E7-E8.

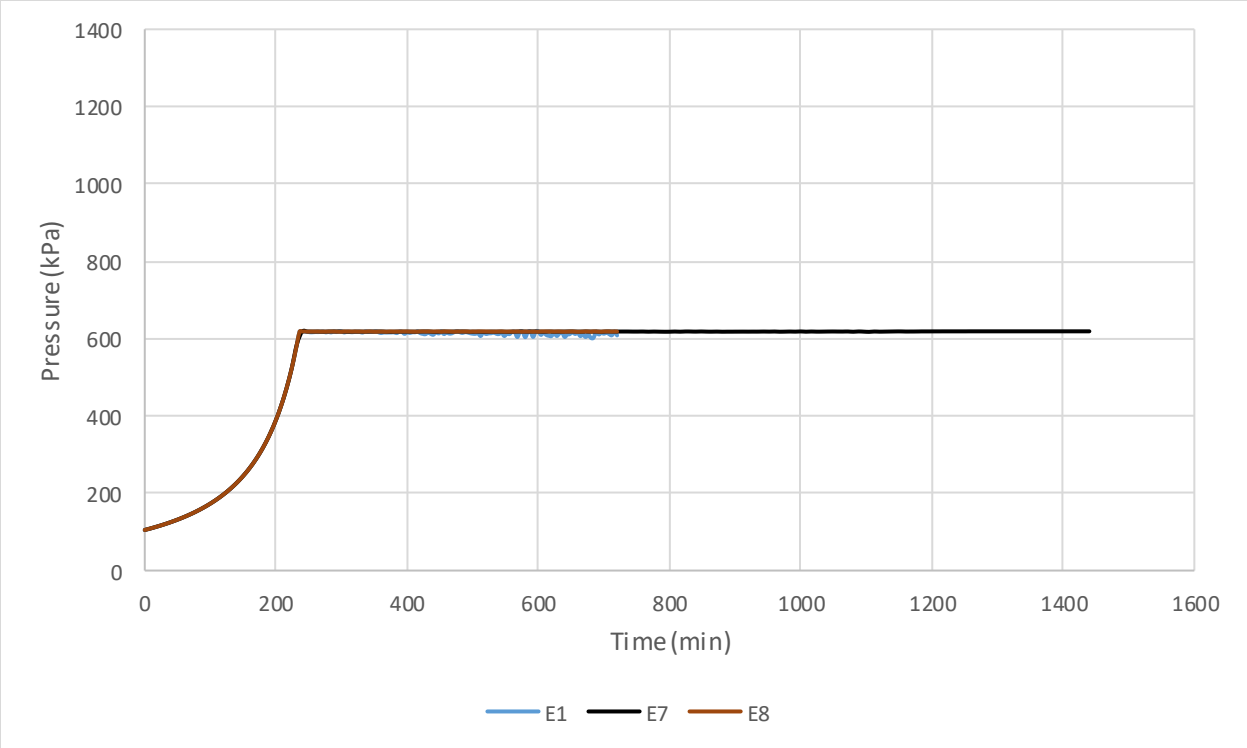

Figure 8.5.17: System pressure versus time for Cases E1 (base line) and E7-E8.

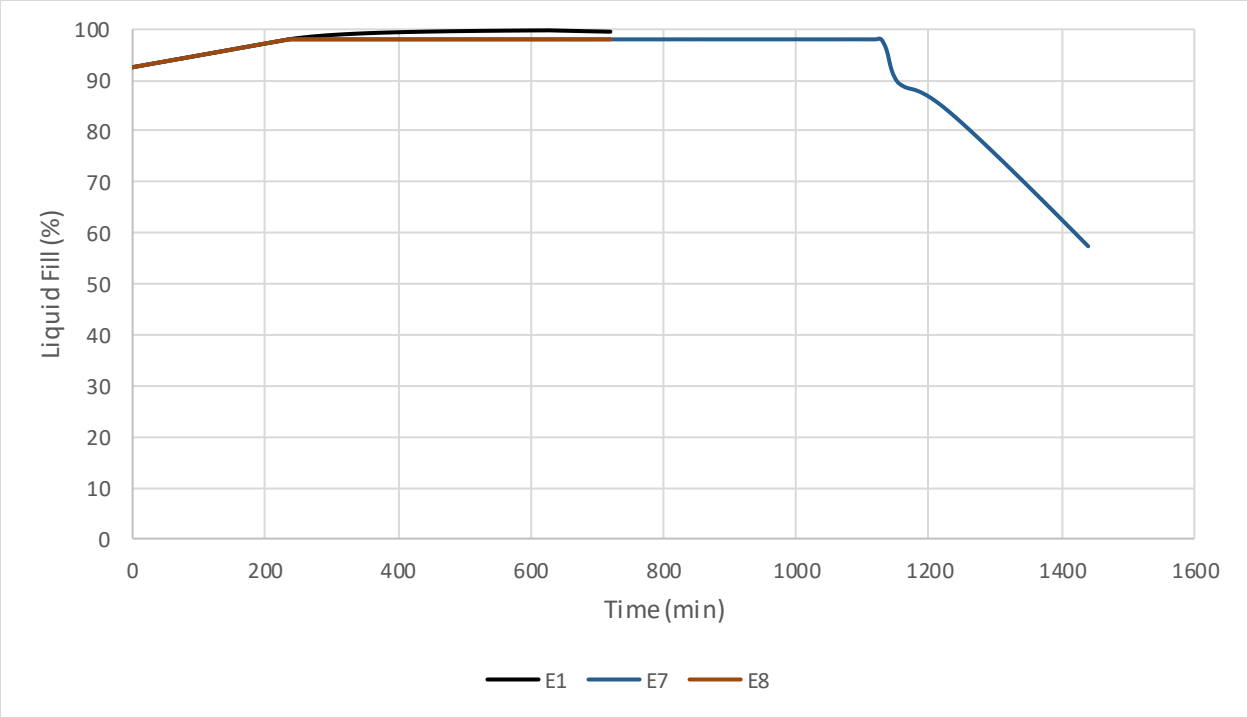

Figure 8.5.18: System liquid fill level time for Cases E1 (base line) and E7-E8.

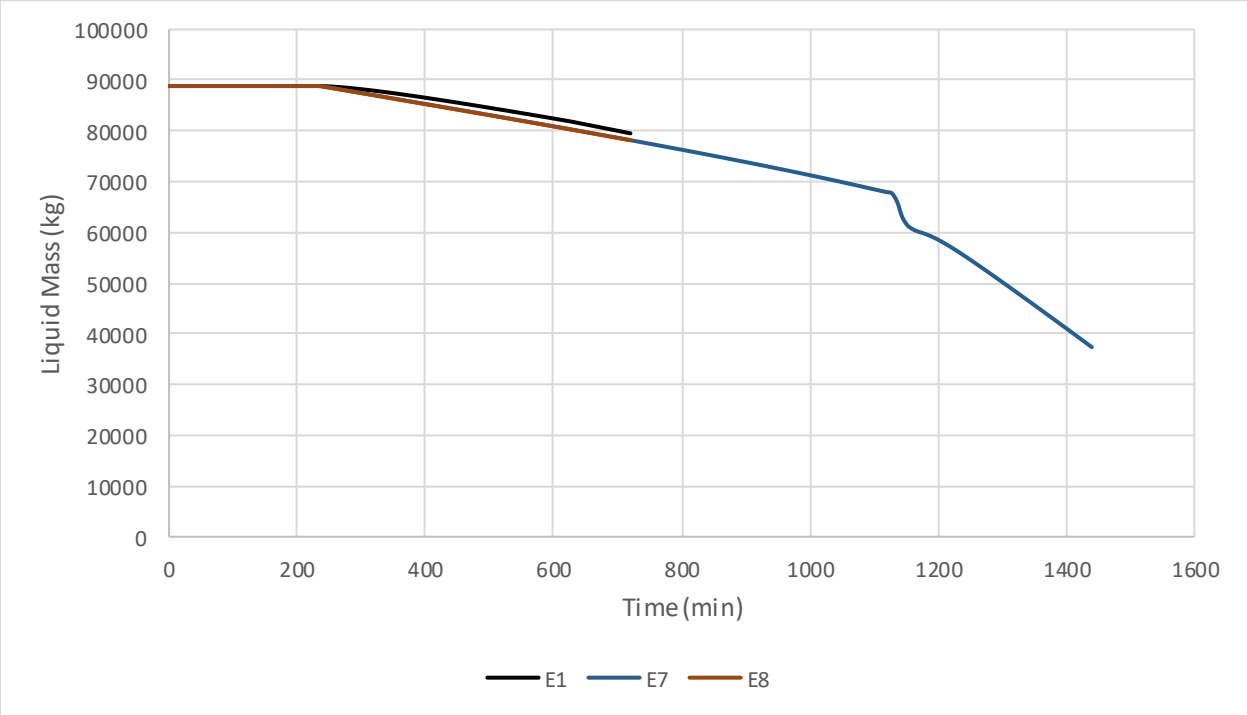

Figure 8.5.19: System liquid mass time for Cases E1 (base line) and E7-E8.

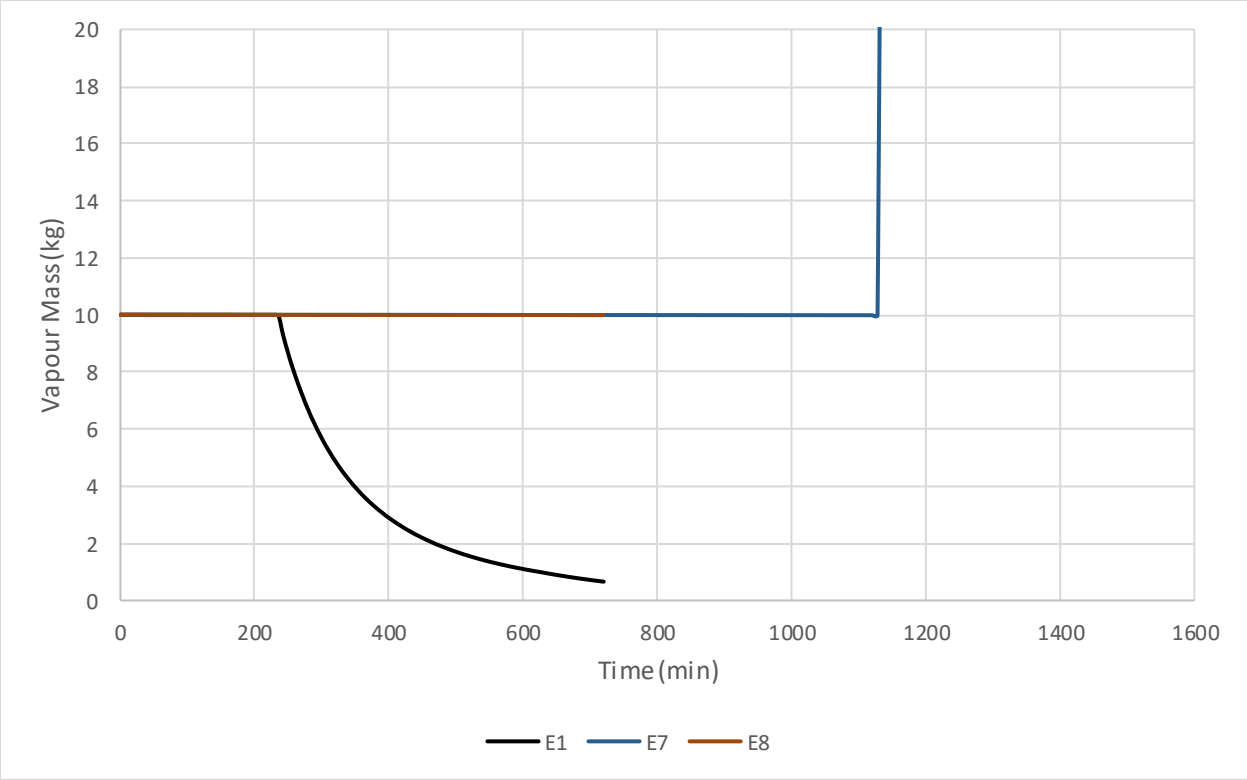

Figure 8.5.20: System vapour mass time for Cases E1 (base line) and E7-E8.

PRV Blockage

Figures 8.5.21 to 8.5.23 present the system average liquid temperature, pressure, and liquid mass versus time profiles, respectively, for the light (FL178) sample with five levels of PRV blockage: 0 (E1), 50 (E9), 80 (E10), 99.8 (E10B), and 100% (E11). Additional details about the scenario inputs to the HYSYS tank car model can be found in Section 5.5. The following list provides key comparative observations between the different levels of PRV blockage:

- It was noted in the 3-D CFD PRV modeling work (Section 8.4) that PRV blockage above 50% results in a reduced maximum flow; however, this did not directly translate to a change in tank car performance as can be seen in the pressure profiles (Figure 8.5.22).
    - PRV blockages of 50 and 80% result in nearly identical performance as the base line case.
    - It takes a PRV blockage of 99.8% to cause any level of over-pressurization under these conditions.
    - It is clear that the rate of vapourization for the light crude under thermally protected conditions is significantly lower than the maximum potential flow through a normally functioning PRV.
- As expected, a fully blocked (100%) PRV results in an exponential increase in tank car pressure.
    - It is estimated that the tank would likely rupture at around the 300 minute mark under these conditions.
    - However, it should be noted that the time to rupture is a strong function of initial fill level and level of thermal protection under fully blocked conditions.

- It can be concluded that PRV blockage is perhaps not as critical a once thought in terms of system venting, as it appears to be greatly oversized when comparing to the estimated rates of vapourization.
    - A change in PRV orientation could alter this conclusion as the PRV performance is different for liquid flow (noted above).
    - A partial blocked PRV scenario could arise during a roll over event.

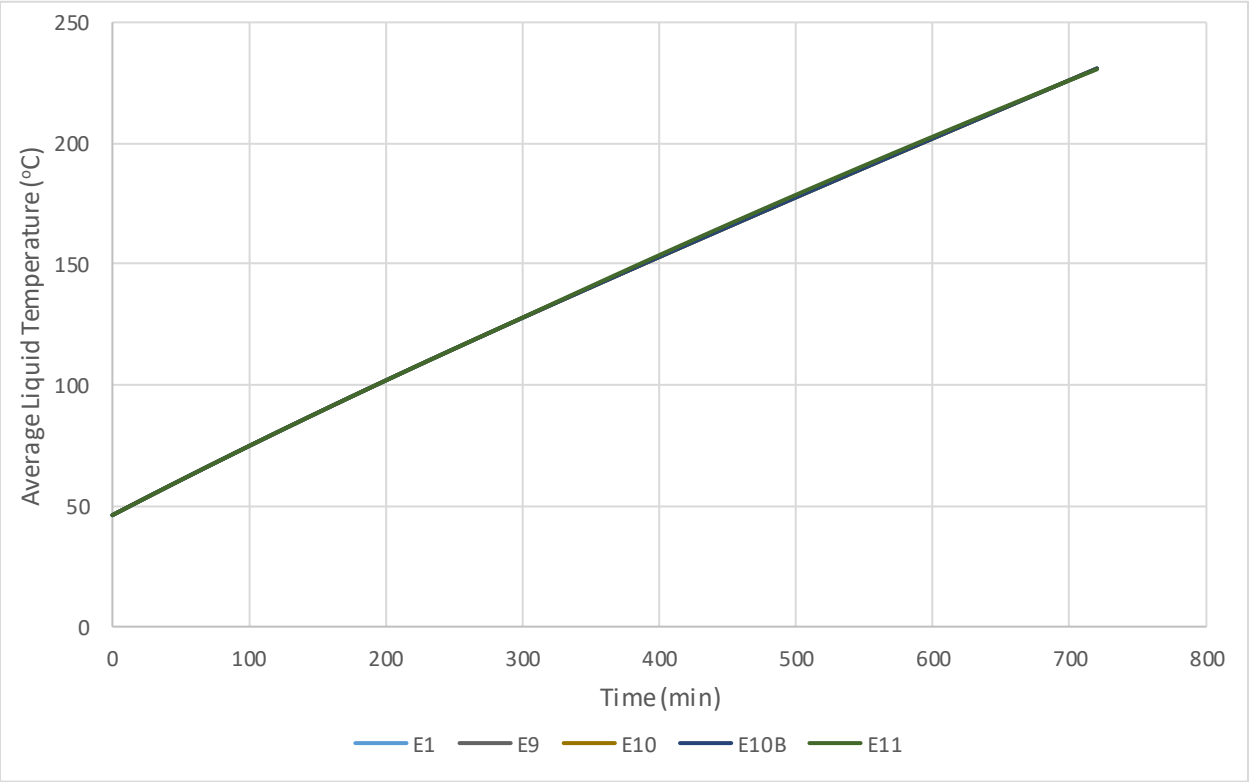

Figure 8.5.21: System average liquid temperature versus time for Cases E1 (base line) and E9-E11.

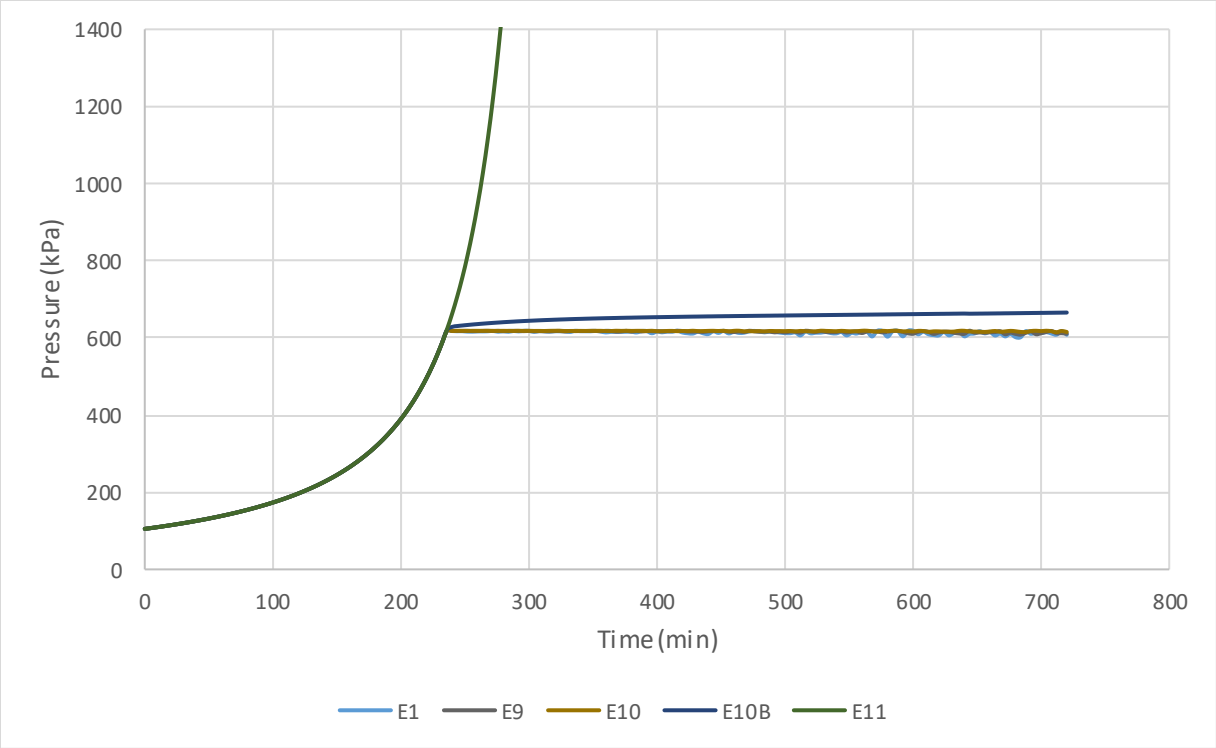

Figure 8.5.22: System pressure versus time for Cases E1 (base line) and E9-E11.

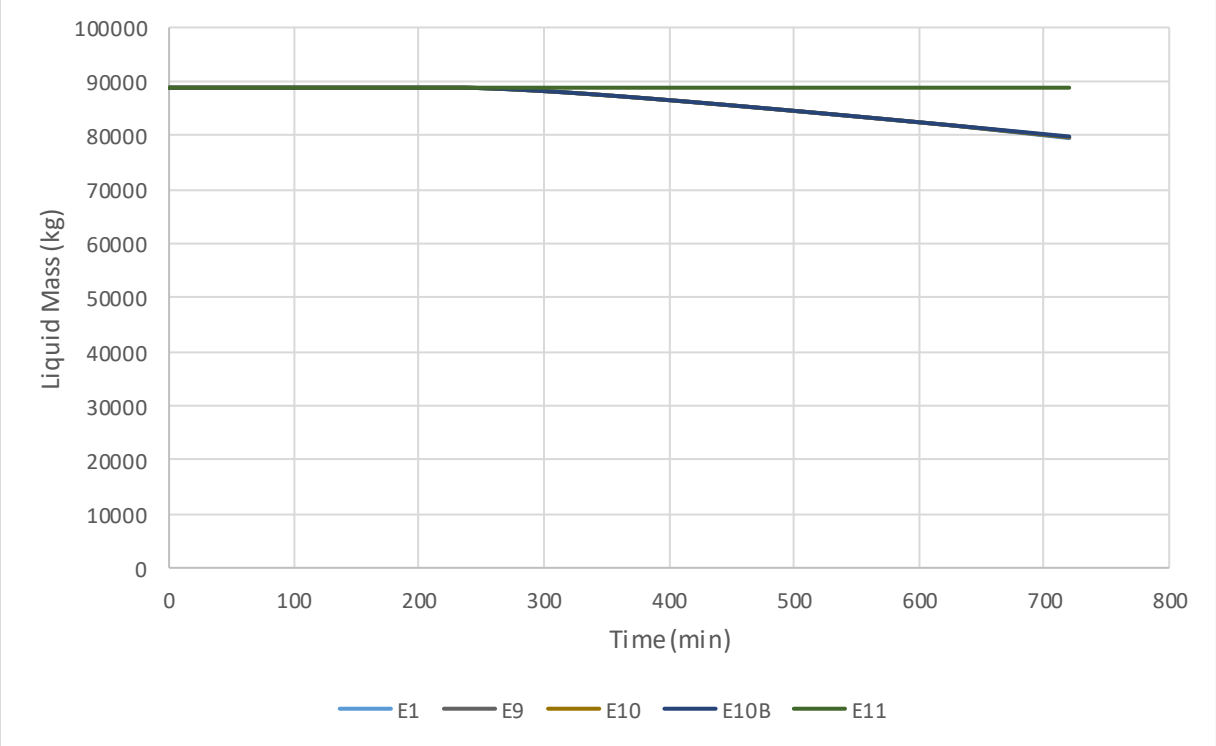

Figure 8.5.23: System liquid mass versus time for Cases E1 (base line) and E9-E11.

Thermal Protection

Figures 8.5.24 to 8.5.28 present the system heat flux, average liquid and vapour temperature, pressure, and liquid fill level versus time profiles, respectively, for the light (FL178) sample with (E18X) and without thermal protection (E12 – bareshell). Additional details about the scenario inputs to the HYSYS tank car model can be found in Section 5.5. The following list provides key comparative observations between the two different levels of thermal protection:

- Unlike most of the other changes in tank car configuration (lading type, PRV orientation, etc.), removing the thermal protection drastically changes the tank car performance both before and after the initial relief event.
    - Figure 8.5.24 shows a large peak in heat flux to the system as the steel shell is raised to near flame temperatures – the heat flux drops rapidly after this point, but still remains at least twice as high as the protected case until the liquid level begins to drop (Figure 8.5.28).
    - As a result, both the liquid (Figure 8.5.25) and vapour (Figure 8.5.26) temperatures are notably higher.
    - Results are in alignment with 2-D CFD tank modeling.
- The initial pressure relief event is decreased from about 240 minutes to 75 minutes (Figure 8.5.27).
    - Over-pressurizing is avoided, even at the increased rates of discharge caused by both accelerated vapourization and higher temperature vapour (low density, higher volumetric flow).
    - It should be noted that very high vapour temperatures (>600°C) are expected once the fill level begins to drop (~450 minutes) that could damage the pressure relief device.
    - Thermal cracking of vapour species is likely at these temperatures, greatly increasing the formation of coke that could plug the PRV.
- It can be concluded that there are a host of potential performance issue if thermal protection is not present or degraded during a fire event.
    - Although not possible at this time with the current HYSYS tank car model, performance assessments at varying levels of thermal protection integrity (i.e., damaged areas) should be examined to get a better understanding of more 'realistic' tank car protection arrangements (pre- and post-accident).
    - Thermal cracking is an important consideration when considering no or partial thermal protection scenarios.

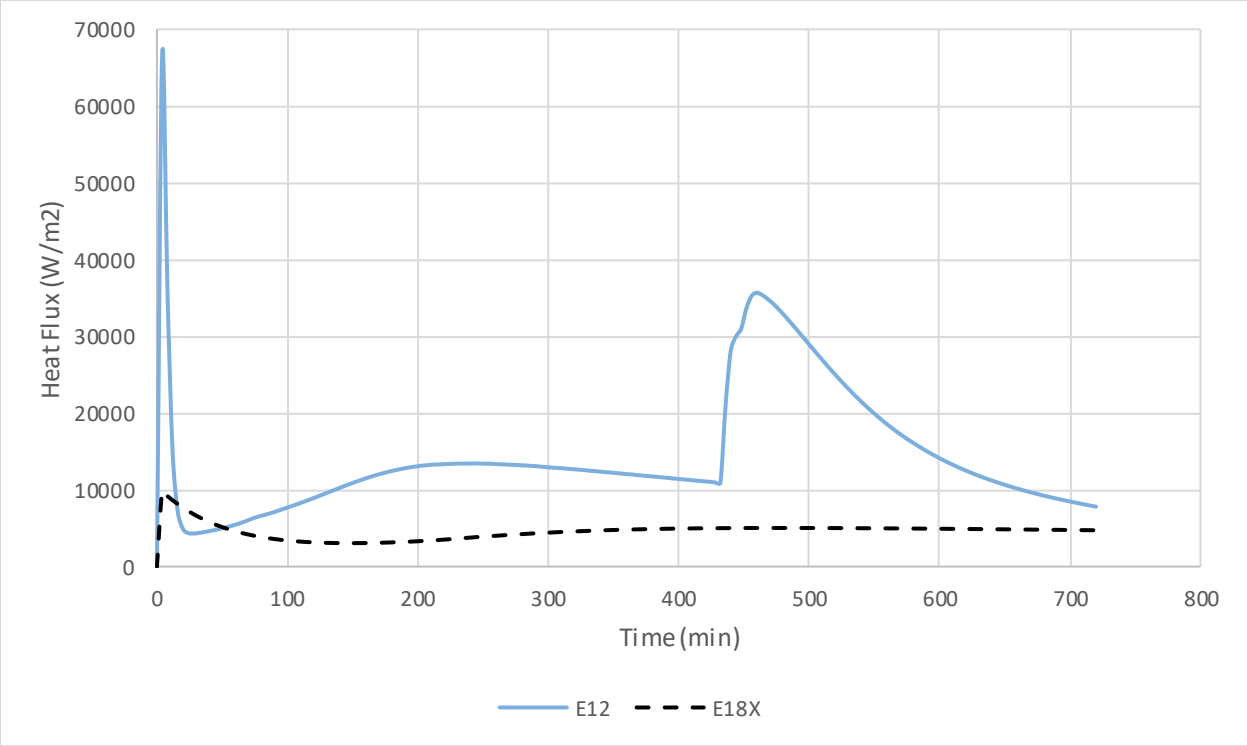

Figure 8.5.24: System heat flux versus time for Cases E18X (base line) and E12.

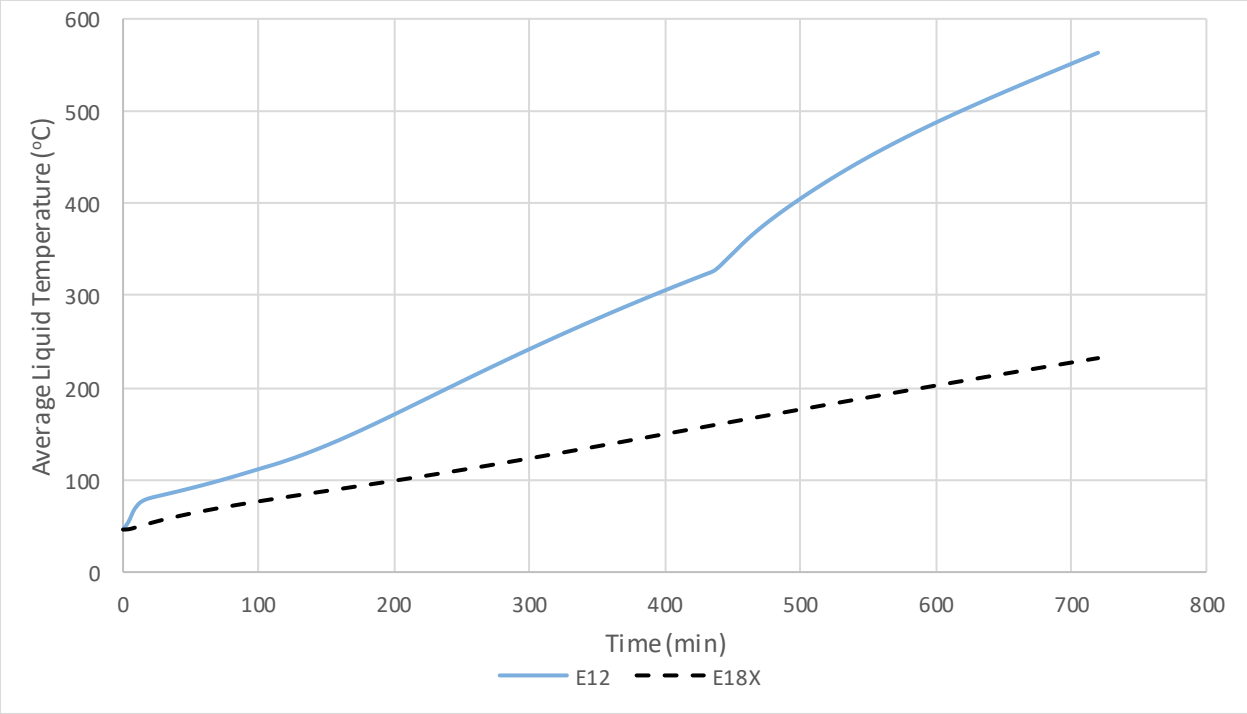

Figure 8.5.25: System average liquid temperature versus time for Cases E18X (base line) and E12.

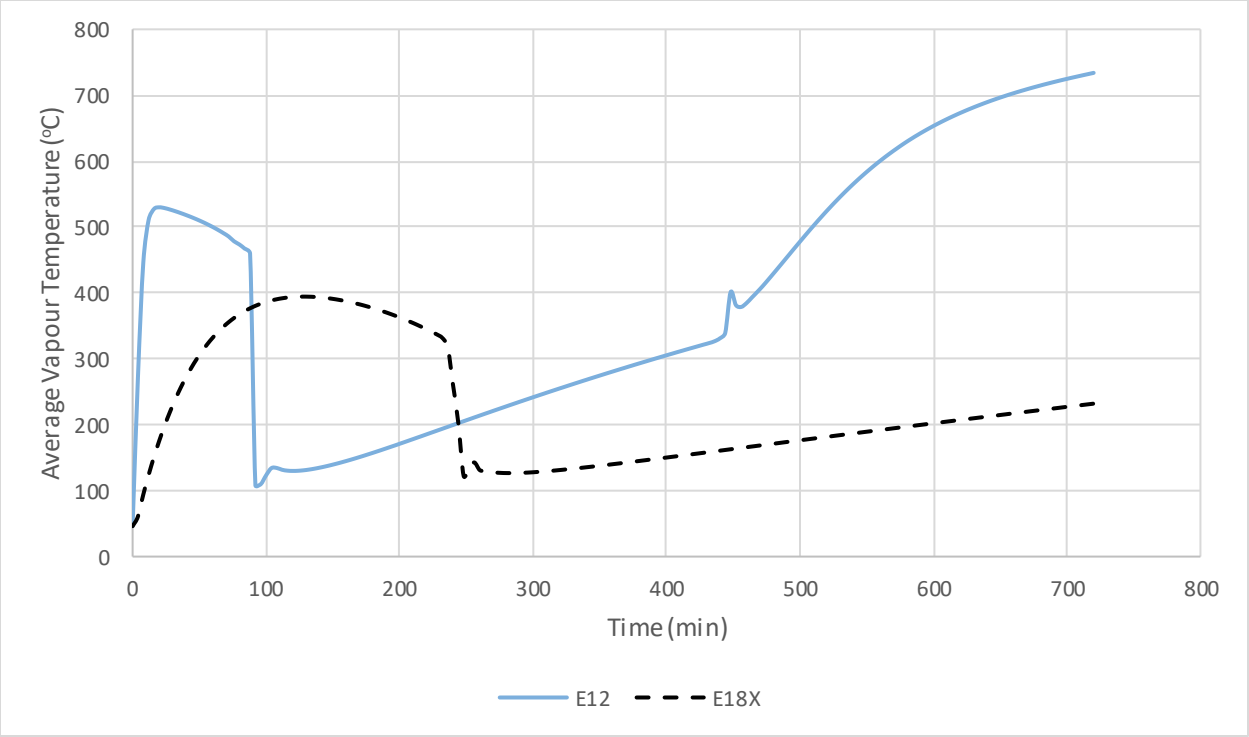

Figure 8.5.26: System average vapour temperature versus time for Cases E18X (base line) and E12.

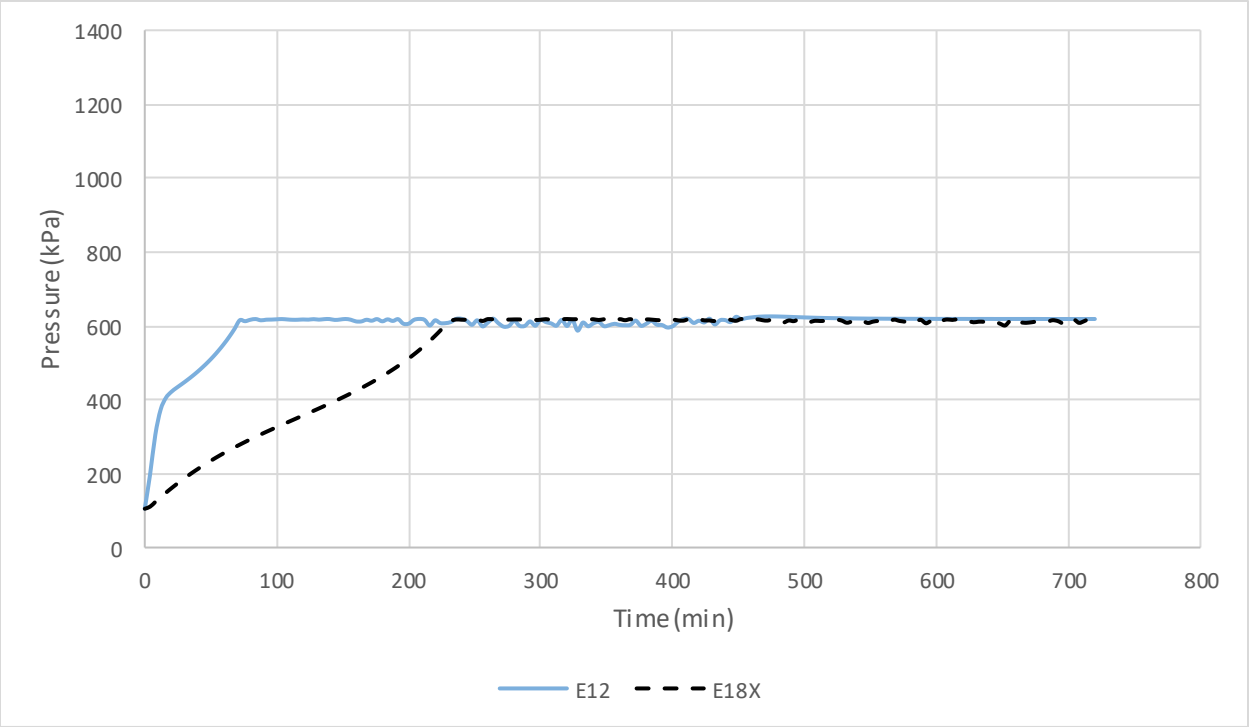

Figure 8.5.27: System pressure versus time for Cases E18X (base line) and E12.

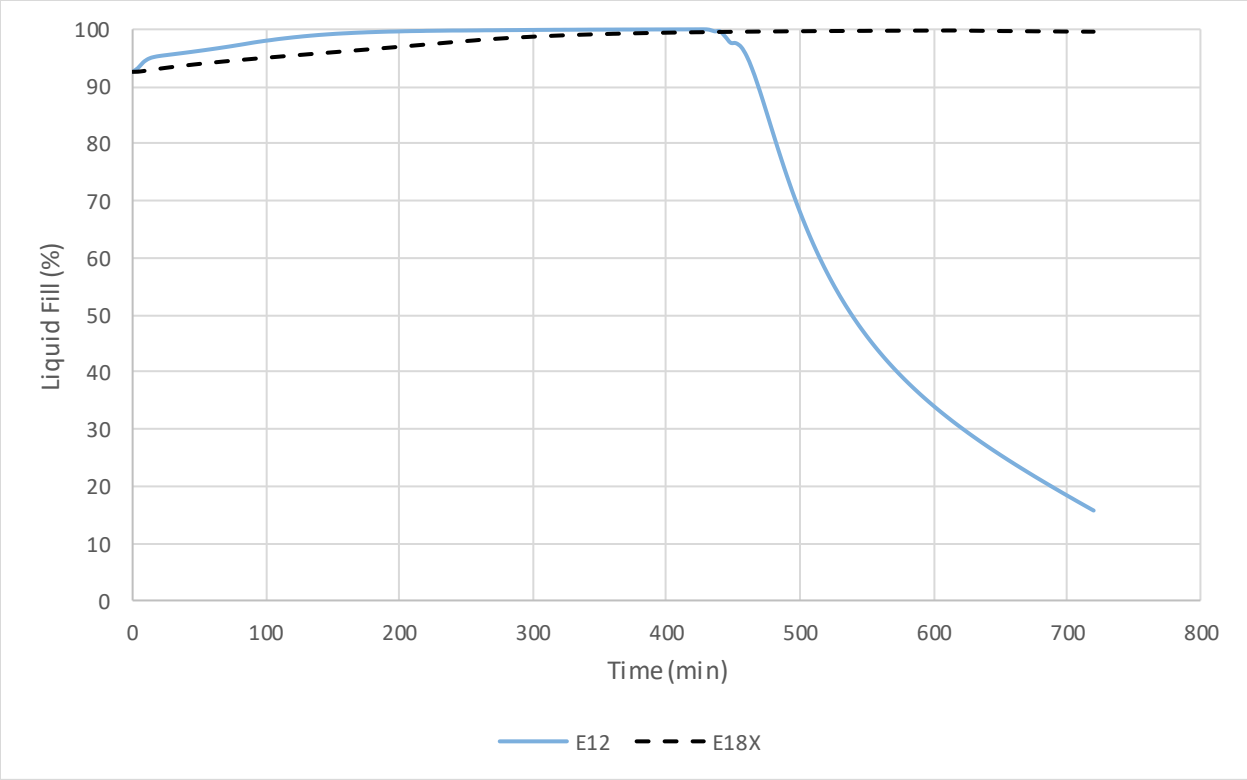

Figure 8.5.28: System liquid fill level time for Cases E18X (base line) and E12.

Volatility

Figures 8.5.29 to 8.5.31 present the average liquid and vapour temperature, and pressure versus time profiles, respectively, for the light (FL178) sample with varying initial vapour headspace compositions: no change (E18X), high C1-C5 (E13), zero C1-C5 (E14), and off-gassed (E15). Initial vapour phase C1-C5 hydrocarbon model fraction rations versus the base line light crude can be found in Table 8.5.1 below. Additional details about the scenario inputs to the HYSYS tank car model can be found in Section 5.5. The following list provides key comparative observations between the four different levels volatility:

- Both the no C1-C5 and off-gassed cases did not result in any significant changes in tank performance against the base line scenario.
    - Liquid temperature (Figure 8.5.29), vapour temperature (Figure 8.5.30), and pressure (Figure 8.5.31) profiles are effectively overlapping.
    - These results can be explained by noting that the initial light hydrocarbon contribution in the vapour headspace is very small in comparison to air and air does not have a strong affinity with crude oils (i.e., there is very little vapour phase hydrocarbon in the air and very little air in the liquid phase hydrocarbon).
- In contrast, the high C1-C5 case changes the tank car performance in a significant manner.
    - There is an observed high liquid temperature and the time to initial relief is nearly halved (130 versus 240 minutes).

- The large quantity of hydrocarbons in the vapour phase changes the VLE of the system, driving down the density of the initial liquid phase (813 versus 830 kg/m^3), thereby increasing the initial liquid fill level and the time it takes to reach the set pressure.
- This change in liquid phase composition also decreases the sensible heating requirements of the sample since larger quantities of the lading are being vented from the system.
- It should be noted that case E13 was run for illustrative purposes to study the effects of volatility and does not reflect a typical lighter crude oil with realistic initial vapour phase C1-C5 hydrocarbons.

- It can be concluded that under normal conditions where the tank car is filled while open to the atmosphere (air), that the level of off-gassing should not impact tank car performance under fire conditions.

Table 8.5.1: Initial vapour phase C1-C5 hydrocarbon mole fraction ratios (versus E18X) for runs E13-15.

Component (hydrocarbons)	E18X FL178	E15 Off-gassed	E14 No C1-C5	E13 High C1-C5
C1	1	0.03	0.00	372
C2	1	0.18	0.00	316
C3	1	0.45	0.00	210
C4	1	0.71	0.00	112
C5	1	0.90	0.00	39

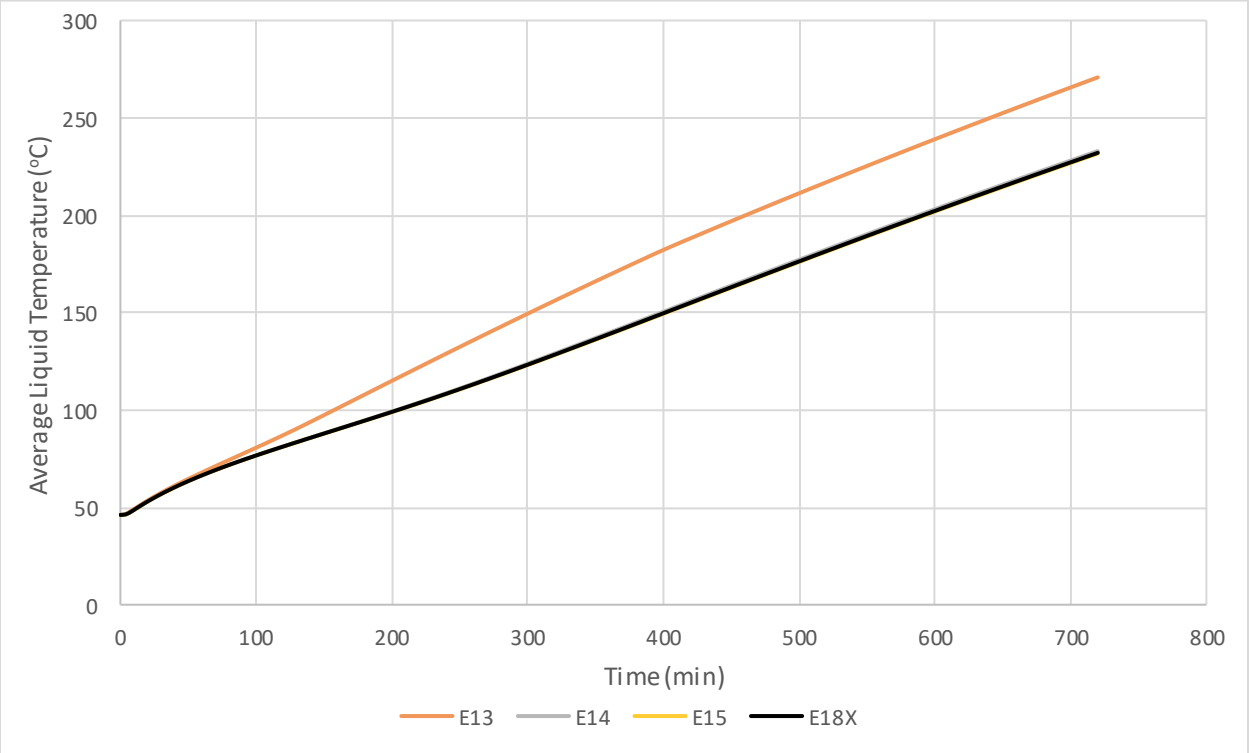

Figure 8.5.29: System average liquid temperature versus time for Cases E18X (base line) and E12-E15.

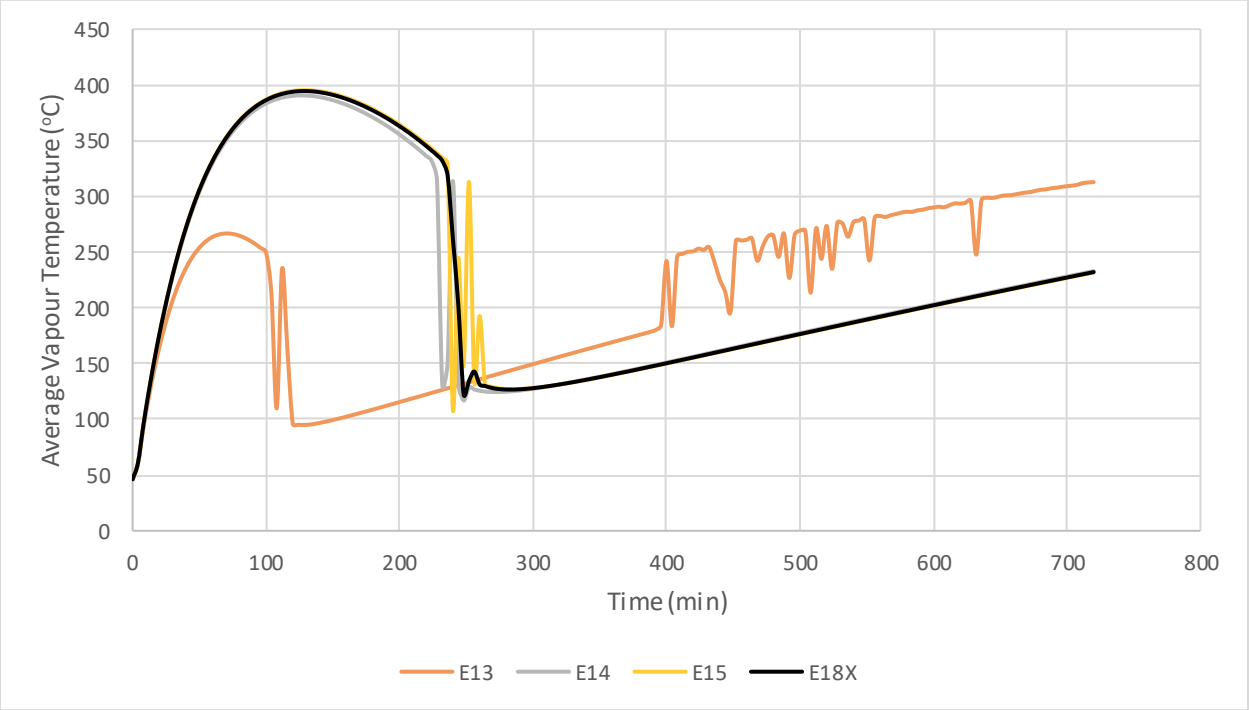

Figure 8.5.30: System average vapour temperature versus time for Cases E18X (base line) and E12-E15.

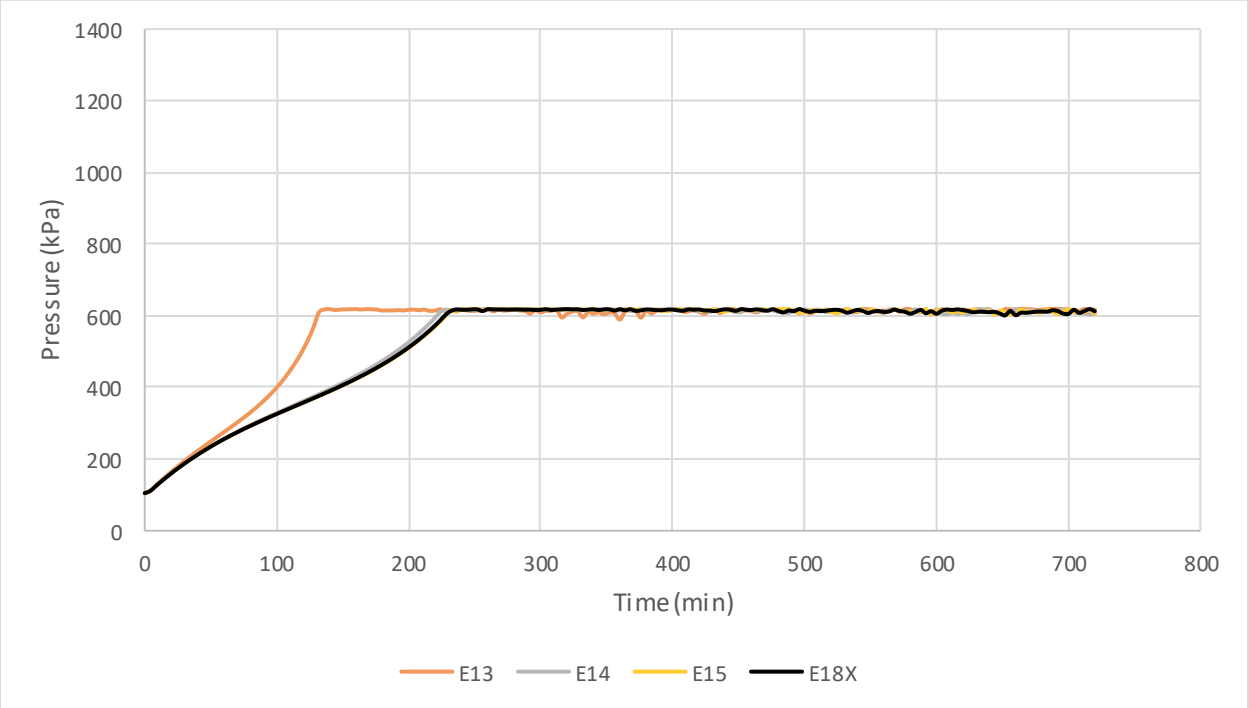

Figure 8.5.31: System pressure versus time for Cases E18X (base line) and E12-E15.

Fire Temperature and Tank Emissivity

Figures 8.5.32 to 8.5.35 present the heat flux, average liquid temperature, pressure, and liquid fill level versus time profiles, respectively, for the light (FL178) sample with varying fire temperatures and tank emissivities:

- **900°C** and 0.90 (E16)
- **950°C** and 0.90 (E17)
- 815.6°C and 0.90 (E18X – baseline)
- **1000°C** and 0.90 (E18)
- **1204.4°C** and 0.90 (E19)
- 815.6°C and **0.92** (E20)
- 815.6°C and **0.80** (E21)
- 815.6°C and **1.00** (E22)

Additional details about the scenario inputs to the HYSYS tank car model can be found in Section 5.5. The following list provides key comparative observations between the different fire and tank properties:

- It is clear that both the heat flux (Figure 8.5.32) and liquid temperature (Figure 8.5.33) profiles are shifted upwards when raising the flame temperature nearly 400°C (from 815.6 to 1204.4°C).
    - As expected, this reduces the time for initial relief from ~240 to 110 minutes (Figure 8.5.34) and would likely represent an upper maximum for a fire scenario in terms of flame temperature.
    - Figure 8.5.35 shows that even after the 720 operating period there is only a small drop in liquid level and only for the 1204.4°C flame temperature case.
    - Even at the higher temperatures, thermal cracking of the liquid hydrocarbons is not significant.
- As the tank emissivity is raised from 0.80 to 1.00, the amount of heat entering the lading is reduced (Figure 8.5.32), increase the time required for initial relief.
    - There appears to be a more significant change in performance when moving from an emissivity of 0.80 to 0.90 than from 0.90 to 1.00.
    - Future work should include cases where the emissivity is lowered beyond 0.80 to further capture potential fire scenarios (e.g., changes in tank emissivity caused by fire and/or deposition).
- It can be concluded that both flame temperature and tank emissivity are important parameters when it comes to predicting tank car performance.
    - While flame temperature measurements are somewhat straightforward to collect, tank emissivity could be more difficult to determine given potential differences in insulation jacketing and crude oil specific depositions (caused by burning of the lading).
    - However, the current level of thermal protection appears to provide good lading stability and performance over a reasonable range of temperatures and emissivities.

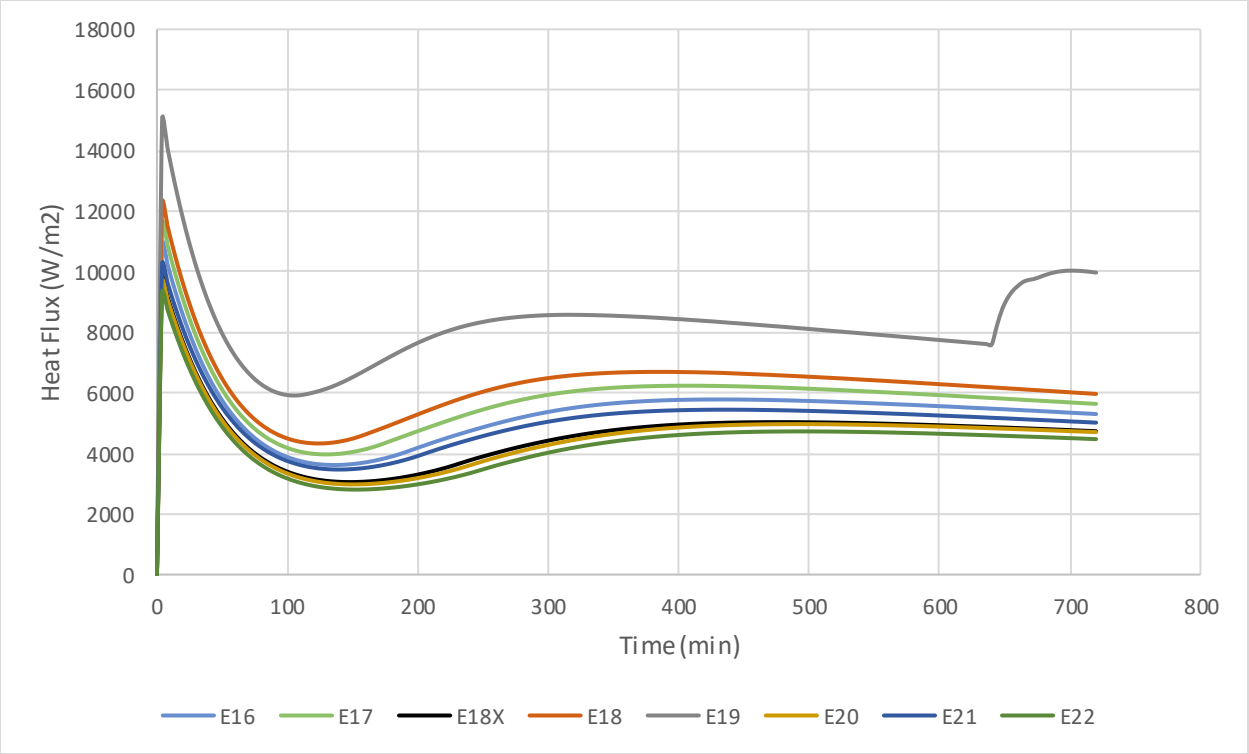

Figure 8.5.32: System heat flux versus time for Cases E18X (base line) and E16-E22.

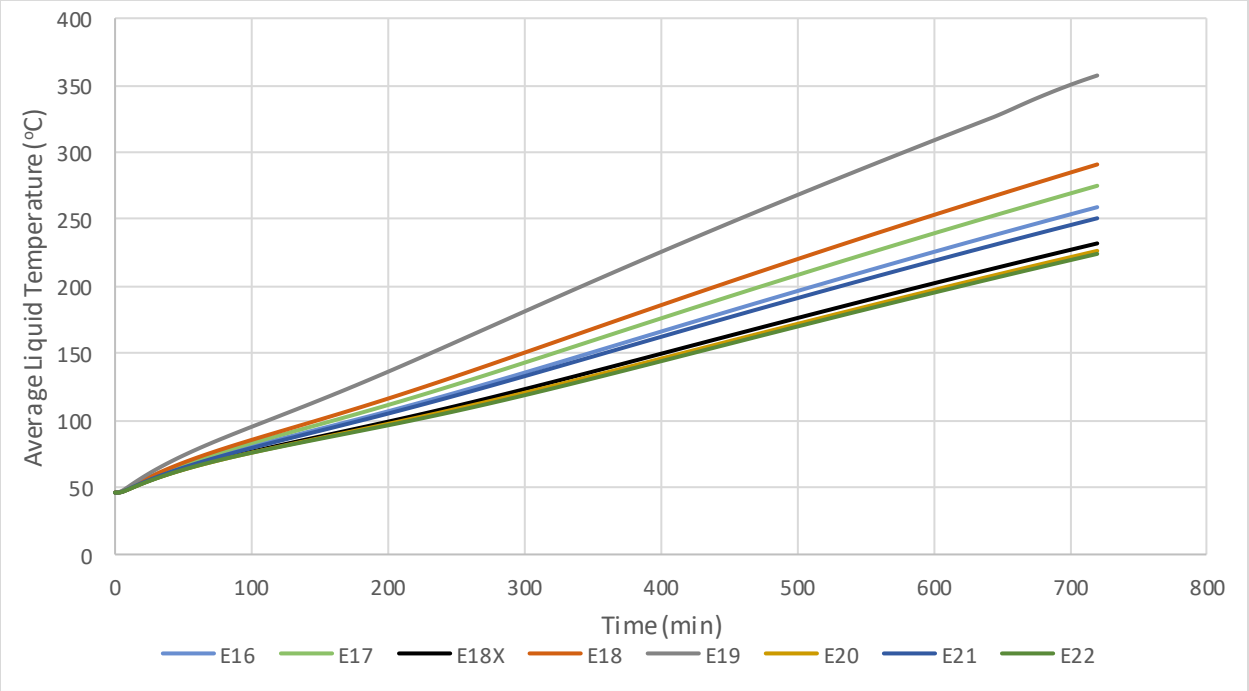

Figure 8.5.33: System average liquid temperature versus time for Cases E18X (base line) and E16-E22.

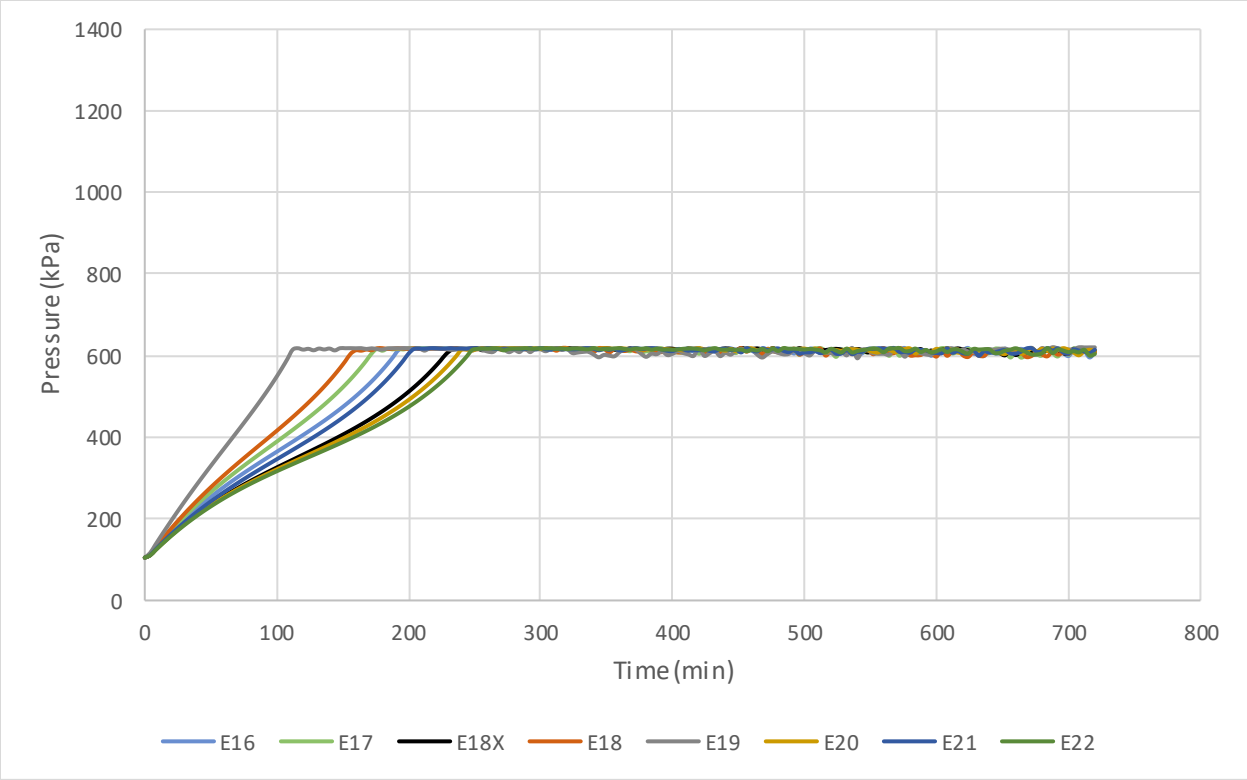

Figure 8.5.34: System pressure versus time for Cases E18X (base line) and E16-E22.

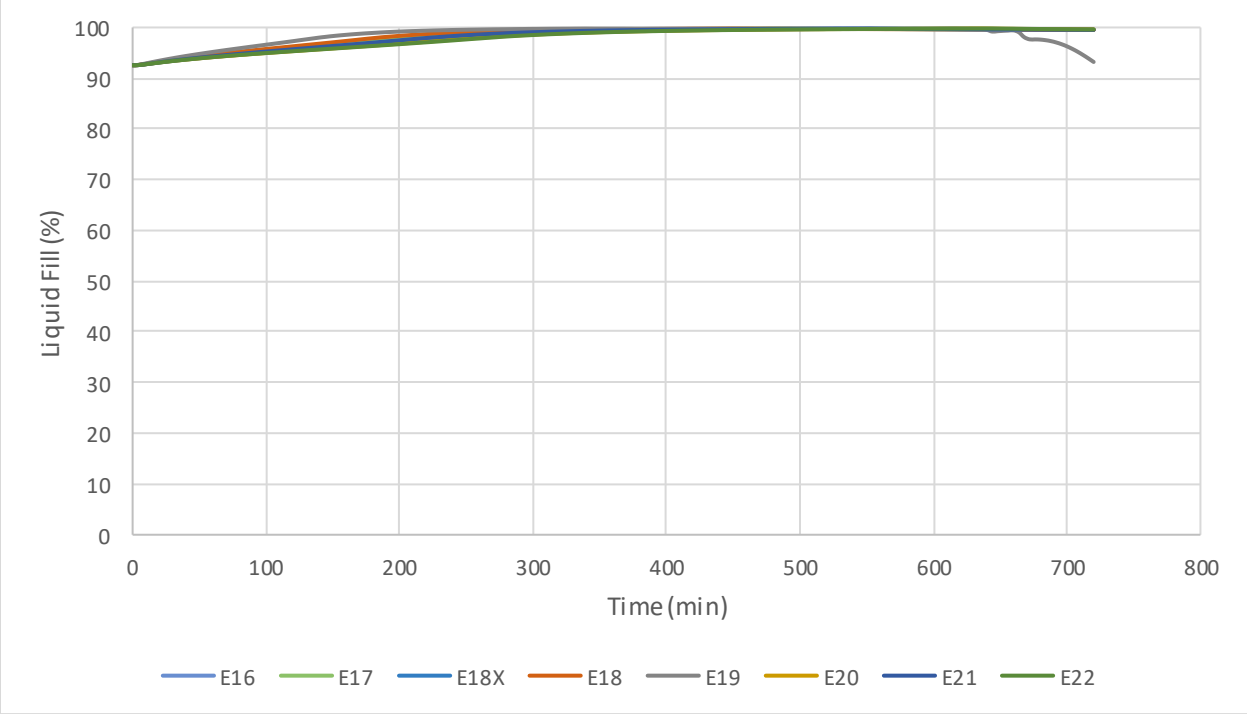

Figure 8.5.35: System liquid fill level versus time for Cases E18X (base line) and E16-E22.

PRV Set Pressure and Fill Level

Figures 8.5.36 to 8.5.40 present the heat flux, average liquid and vapour temperature, pressure, and liquid fill level versus time profiles, respectively, for the light (FL178) sample with a higher set pressure (1239 kPa – E23) and two lower fill levels (87.5% – E24 and 80% – E25). Additional details about the scenario inputs to the HYSYS tank car model can be found in Section 5.5. The following list provides key comparative observations between the different cases:

- Increasing the PRV set pressure shifted the time of the initial relief event by approximately 60 minutes to the 300 minute mark, but in general, the performance is quite similar to the baseline conditions.
    - The only notable difference, which can be seen in Figures 8.5.36 and 8.5.37, is that the elevated pressures cause a shift in system VLE leading to a slight higher rate of heat uptake.
- Since it has already been noted that initial tank car pressurization is primarily driven by liquid expansion, it is not surprising that dropping the liquid level increases the time it takes for venting to begin.
    - It takes approximately 440 minutes at an initial fill level of 87.5% and exceeds the 720 minute period modeled at an initial fill level of 80% (Figure 8.5.39).
- Interestingly, the heat uptake (Figure 8.5.36) is significantly reduced at lower initial fill levels.
    - From Figure 8.5.40, it appears that the heat uptake follows the liquid fill level as the liquid is the primary heat sink (in alignment with CFD results).
    - The vapour temperature is driven higher at lower fill levels (Figure 8.5.38) because a larger fraction of the tank car shell is in the vapour region, but the rate of heat transfer to the vapour is limited as the temperature rises (i.e., less driving force).
- It can be concluded that lower initial fill levels significantly delay tank release.

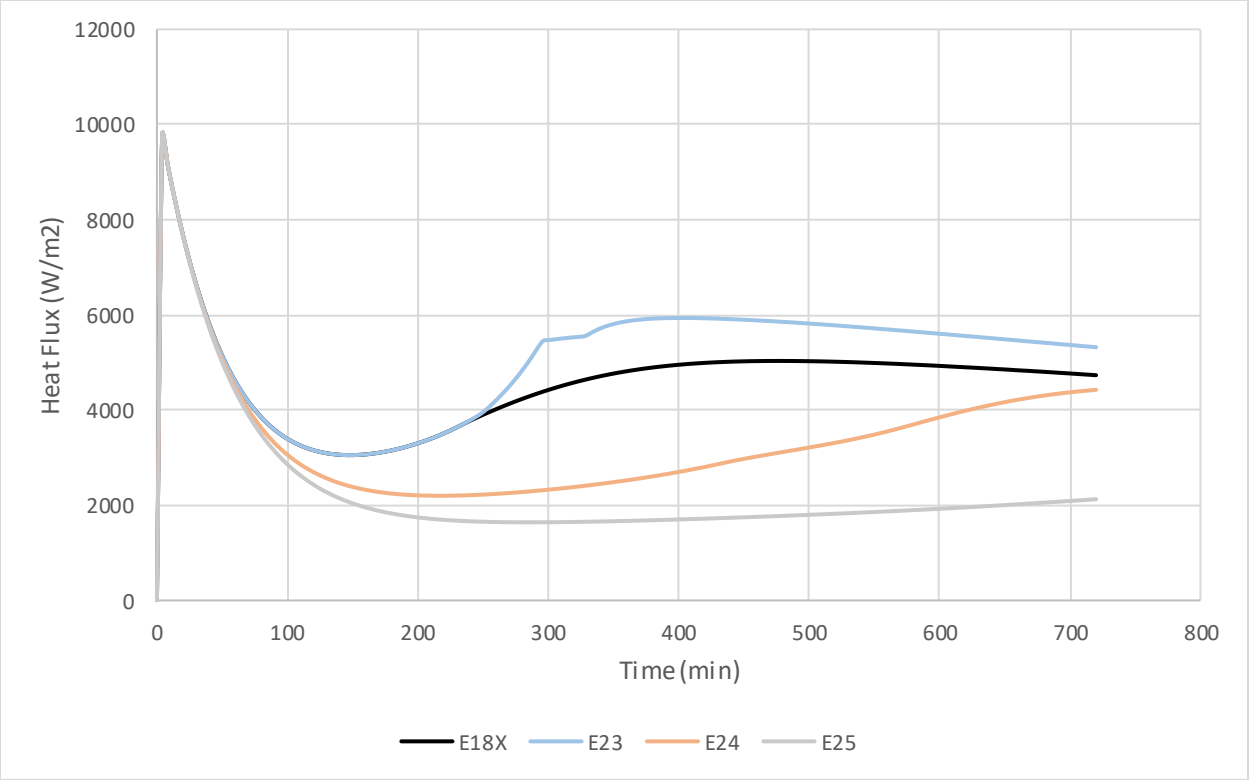

Figure 8.5.36: System heat flux level versus time for Cases E18X (base line) and E23-E25.

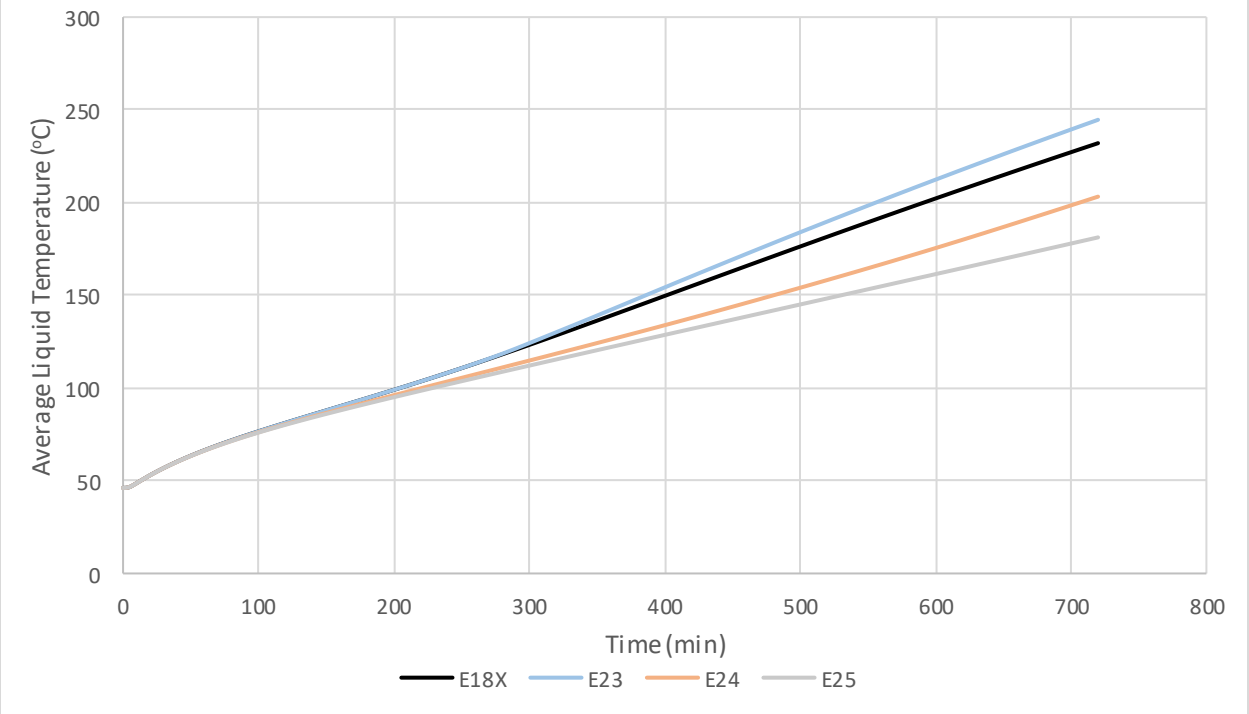

Figure 8.5.37: System average liquid temperature versus time for Cases E18X (base line) and E23-E25.

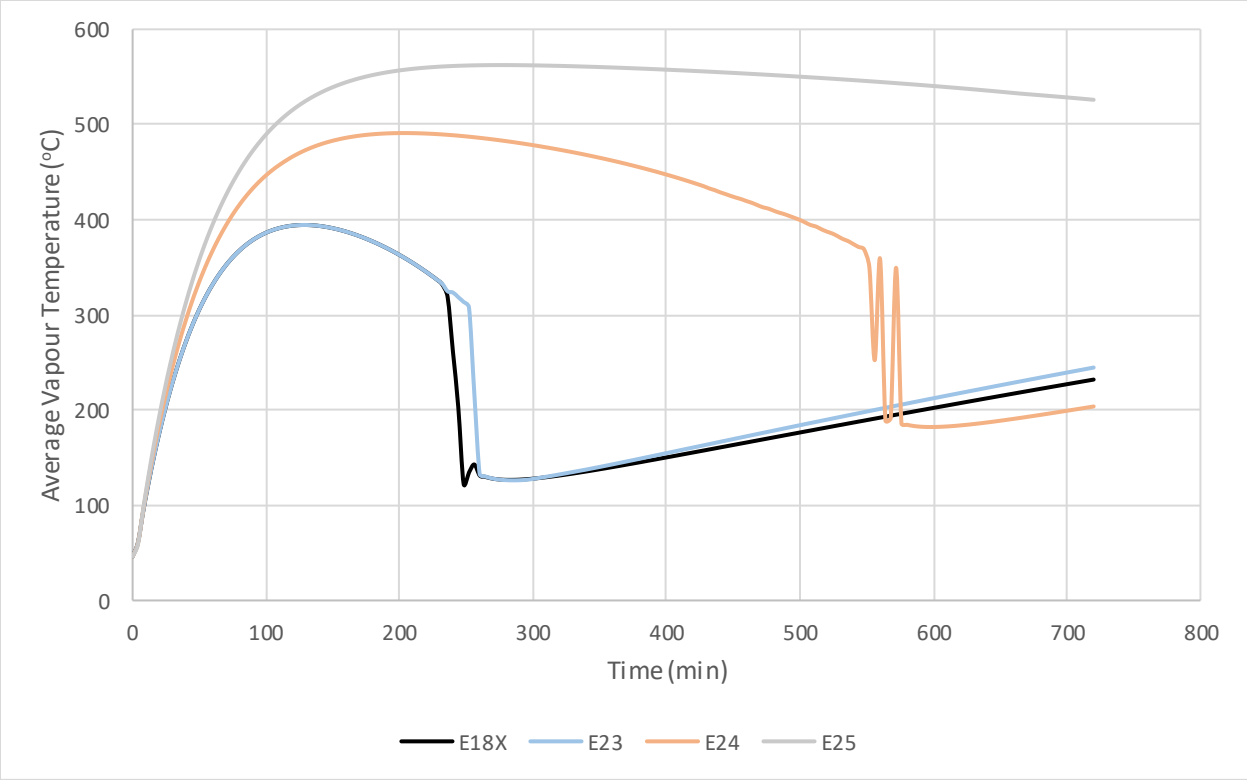

Figure 8.5.38: System average vapour temperature versus time for Cases E18X (base line) and E23-E25.

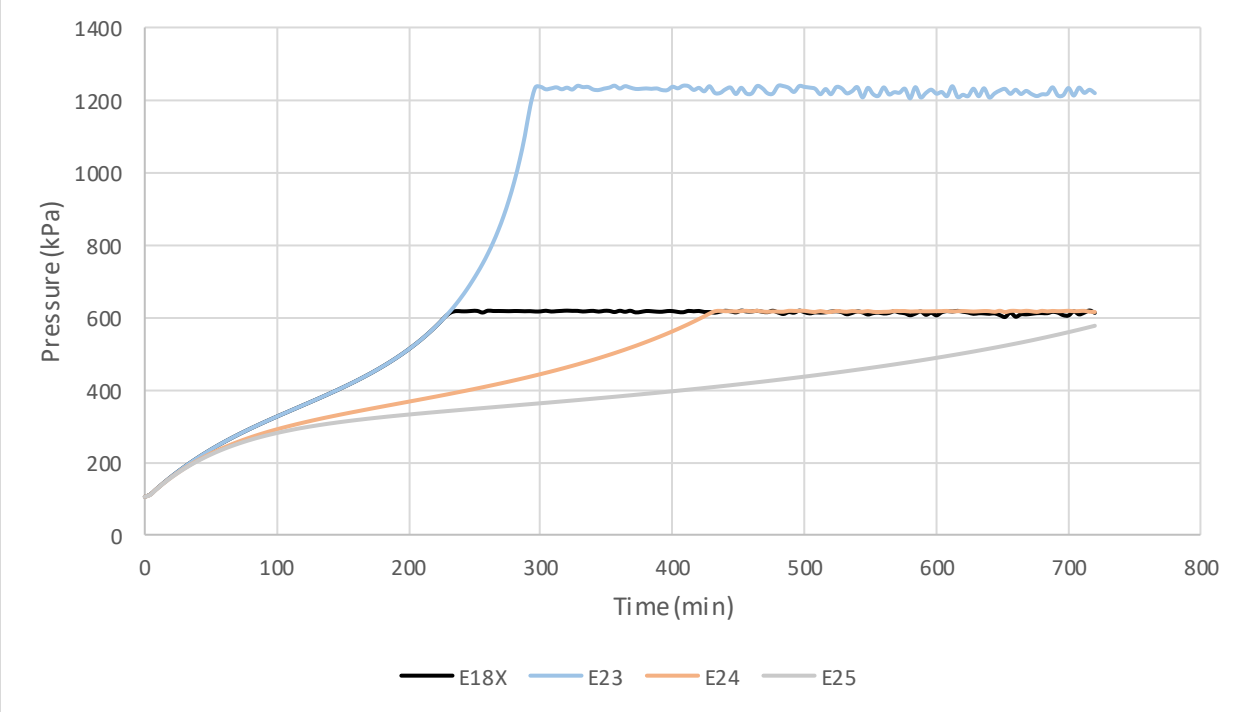

Figure 8.5.39: System pressure versus time for Cases E18X (base line) and E23-E25.

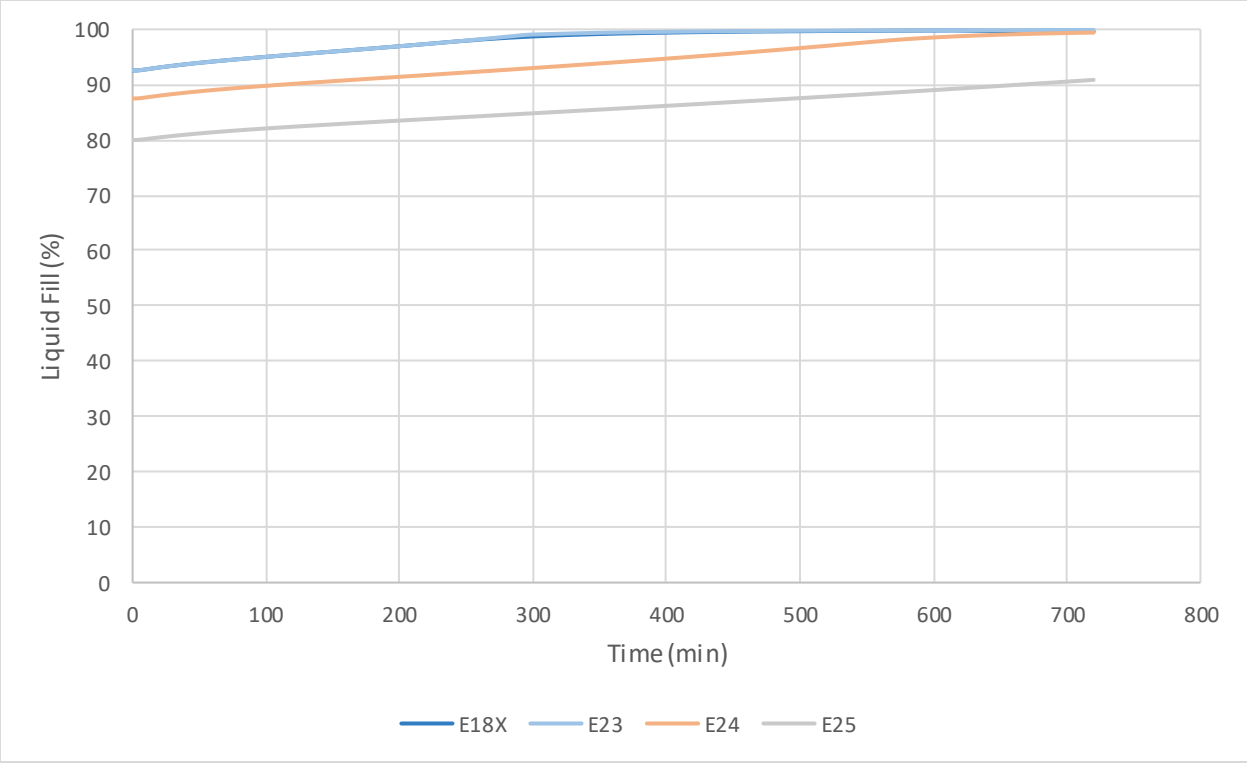

Figure 8.5.40: System liquid fill level versus time for Cases E18X (base line) and E23-E25.

9. Conclusions

9.1 Crude Oil Type

Initial fill level of a tank car plays a key role in time to pressurization in a fire. While the tank fill level for medium and heavy crude oils tends to be limited to below 95% by volume by the maximum gross rail load, this tends not to be the case for lower density ladings like light crudes and condensates. Based on the maximum gross rail load of 286000 lbs, for a DOT 117 (TC 117) car with a tank volume of 30500 US gallons, the light medium crude, LM1, could be filled to 95% by volume, the light crude, L1, could be filled to 97%, and the condensate, C1, could be filled to 100%. Very high fill levels result in rapid pressurization ('rapid' meaning the tank pressurizes with only a small temperature rise) and a higher likelihood of flammable liquid being vented through the pressure relief valve into the fire.

The reduction in liquid density with increasing temperature not only drives convection, it causes an overall liquid expansion in the tank that contributes to, and usually dominates, the initial pressurization of crude oil tanks that are initially 95% full or higher. Because of this overall liquid expansion, the time to reach relief pressure is very sensitive to fill level for high fill levels.

Ladings with a low and narrow boiling point range, such as condensates, have a higher risk of a more severe BLEVE because they present the possibility of rapid vaporization of the entire lading upon loss of containment. Within the substances studied in this report, even the lightest crude oil had a significantly larger range of boiling temperatures than the condensate, which suggests crude oils have a lower

propensity for severe BLEVE than condensates. The condensate, C1, was found to have a low and narrow boiling point range and, hence, a higher chance of BLEVE. This is illustrated by considering a tank containing the condensate, C1, at 85°C and 65 psig, suddenly depressurizing to ambient pressure, at which condition (85°C, 0 psig) the condensate would normally be 100% vapour. The light crude oil, L1, would normally be, at most, 20% vapour at this condition, with the threat reducing for heavier-and-heavier crudes.

9.2 Heat Transfer Mechanisms

Comparison of the model to US DOT/FRA experiments, provided in Appendix A, confirmed that the dominant mechanism for heat transfer from the fire to the tank is *via* radiation, even if the fire is "touching" the tank, as is the case in an engulfing fire. Consequently, for bare tanks, the rate of heat transfer to the lading is limited by the radiative heat flux that can be generated by the fire, not by the rate at which the liquid lading can absorb heat from the tank shell.

The CFD model showed in all cases an initial ramp-up in heat transfer rate from the fire to the lading, plateauing at a rate that depended on several factors. For thermally-protected tanks, the heat transfer rate plateaued at a value that was governed by the thermal protection, not by the type of lading, although the ramp-up time depended on the type of lading, with less viscous ladings reaching the plateau sooner. For bare tanks (the opposite extreme), the heat transfer rate plateaued at a much higher value (though always below the radiant heat flux generated by the fire) and it depended on the type of lading, with less viscous ladings reaching a higher heat transfer rate than more viscous ladings. Again, the ramp-up time to reach the plateau heat transfer rate was shorter for less viscous crude oils.

The dominant heat transfer mechanism across the annular gap between jacket and shell was found to be radiation. Convection and conduction of heat by the air in this annular gap was relatively small. The only curtailment of heat transfer across an unprotected annulus was a result of the steel surfaces bounding the annulus being not perfectly emitting. This implies that significant thermal protection could be achieved by making these surfaces low emitting through, for example, a coating or foil. This could serve to augment or back-up the ceramic fiber blanket thermal protection.

It was found that the thermal protection provided by a ½ inch-thick ceramic fiber blanket could be very effective, dramatically reducing the heat transfer rate to the shell and crude oil, provided it is in place and intact. The thermal protection reduced the heating rate of the light oil to less than a tenth of that for the bare tank. It was, however, observed that over a period of about an hour, despite the relatively low heat transfer rate, the temperature of the steel at the top of the tank could rise to approximately 400°C. This occurred because heat that accumulated in the portion of the shell in contact with the gas headspace had little means of transferring away. This behaviour emphasized the lack of heat transfer provided by gases and vapour in contact with the shell and the ineffectiveness of the shell to conduct heat away from its own hotspots.

9.3 PRV Performance

CFD analysis of a commercial pressure relief valve found that, for the properly functioning valve, the liquid discharge coefficient was the same for all liquids at approximately 0.60 and the gas (or vapour) discharge coefficient was the same for all gases at approximately 0.72. These are within the range of typical values for liquids and gases. Partially blocked valves passing liquid flow were also investigated; blockages of the

PRV may occur in accident scenarios when, for example, chemical reactions in the crude oil produce coking, or when the PRV has been damaged by impact or fire. A 20% blockage caused no significant reduction in discharge. A 50% blockage reduced the liquid discharge coefficient from 0.60 to 0.47 and an 80% blockage further reduced it to 0.17.

In addition, it was apparent from the study that gas flow quickly relieves pressure and discharges little mass, whereas liquid flow rapidly discharges mass and is less effective at quickly relieving pressure. When liquid discharges, the pressure release valve could remain open for a longer time than for gas and discharge a large mass of flammable liquid into the surrounding fire.

9.4 Fire Scenarios

The updated Aspen HYSYS tank car model used crude oil specific heat flux versus time data and PRV discharge coefficients to better understand the significance of several key variables, specifically:

1) Lading type and Reactions
2) PRV orientation
3) PRV blockage
4) Thermal protection
5) Volatility
6) Fire temperature and tank emissivity
7) PRV set pressure and fill level
8) Fill level

The primary objective for the first part of the work was to generate the necessary comparative modeling results under conditions with and without the inclusion of thermal cracking reactions and to determine whether reactions significantly impact tank car performance under typical fire conditions. It was determined that thermal cracking is somewhat insignificant below tank car lading temperatures of ~425°C and could largely be excluded from analyses where this temperature is not exceeded. During this portion of the work, it was observed that VLE of the liquid-vapour interface affected the stability of the tank car model. For this reason, a low recycle efficiency was selected to avoid unfeasible physical system outputs. This allowed for the determination of vapour phase temperature estimates, but it is in the authors' opinion that the effects of system recycle efficiency and radiative heat transfer to the vapour phase should be investigated further.

When examining changes in performance with lading type, it was shown that lighter samples do not reach as high of liquid temperatures as the heavier samples because the lighter samples begin to vapourize and vent earlier, thus removing heat from the system. Although there are differences in rates of vapourization between the five crudes, the relatively high initial fill levels, combined with the low liquid temperatures, limit their influence on tank performance. In these cases, liquid expansion is the dominant force. There are no discernible changes in tank car performance when cracking reactions are not considered. Even when the operating period was extended to 24 hours, the liquid phase temperatures are below the ~425°C mark.

The PRV orientation significantly impacted the venting process as there is a shift from liquid vapourization/vapour venting to liquid expansion/liquid venting. While the venting of liquid could be problematic given it would likely be discharged into the surrounding fire, the PRV used in this work appears to be appropriately sized as no system over-pressurization was observed at any of the orientations studied. When considering venting of vapour with PRV blockage, it appears that the PRV is able to manage tank pressurization with the estimated rates of vapourization even when severely blocked. However, a change in orientation could alter this conclusion as the PRV performance is different for liquid flow – a condition not explored in this work.

Unlike most of the other changes in tank car configuration (lading type, PRV orientation, etc.), removing the thermal protection drastically changes the tank car performance, both before and after the initial relief event, as the liquid and vapour temperatures are notably higher (matching the CFD results). However, over-pressurizing is avoided even at the increased rates of discharge caused by both accelerated vapourization and higher temperature vapour (low density, higher volumetric flow). Thermal cracking is an important consideration when considering no or partial thermal protection scenarios due to the possibility of temperatures above ~425°C mark. Although not possible at this time with the current HYSYS tank car model, performance assessments at varying levels of thermal protection integrity (i.e., damaged areas) should be examined to get a better understanding of more 'realistic' tank car protection arrangements (pre- and post-accident).

After looking at a variety of different levels of crude oil volatility, it can be concluded that under normal conditions where the tank car is filled while open to the atmosphere (air), that the level of off-gassing should not impact tank car performance under fire conditions. An artificially high amount of volatile compounds does significantly increase the rate of pressurization and time to first vent, but this behaviour was not observed to a notable degree in the lading comparison cases, where crude oils with realistic compositions were used for reasons discussed above.

It can be concluded that both flame temperature and tank emissivity are important parameters when it comes to predicting tank car performance. While flame temperature measurements are somewhat straightforward to collect, tank emissivity could be more difficult to determine given potential differences in insulation jacketing and crude oil specific depositions (caused by burning of the lading). However, the current level of thermal protection appears to provide good lading stability and performance over a reasonable range of temperatures and emissivities.

As expected, increasing the PRV set pressure shifts the time of the initial relief event, but in general, the performance is quite similar to the baseline conditions. Since it has already been discussed that the initial tank car pressurization is primarily driven by liquid expansion, it is not surprising that dropping the liquid level increases the time it takes for venting to begin (i.e., delayed tank release).

Acknowledgement

This project was funded by Transport Canada. The authors would like to thank the National Research Council Canada and the USDOT/Federal Railroad Administration for their valuable input and discussions related to this work.

References

[1] A.M. Birk, Scale considerations for fire testing of pressure vessels used for dangerous goods transportation, Journal of Loss Prevention in the Process Industries 25 (2012) 623-630.

[2] A. D'Aulisa, A. Tugnoli, V. Cozzani, G. Landucci, A.M. Birk, CFD Modeling of LPG Vessels Under Fire Exposure Conditions, AIChE Journal, December 2014 Vol. 60, No. 12, 4292-4305.

[3] G. Landucci, A. D'Aulisa, A. Tugnoli, V. Cozzani, A.M. Birk, Modeling heat transfer and pressure build-up in LPG vessels exposed to fires, International Journal of Thermal Sciences 104 (2016) 228-244.

[4] C.M. Yu, N.U. Aydemir, J.E.S. Venart, Transient Free Convection and Thermal Stratification in Uniformly-Heated Partially-Filled Horizontal Cylindrical and Spherical Vessels, Journal of Thermal Science Vol. 1, No. 2, 114-122.

[5] Federal Railroad Administration. (2020). Performance of Tank Car Pressure Relief Devices Under Fire Conditions. Washington: U.S. DOT.

[6] R.A. Guidotti, M. Moss, Thermal Conductivity of Thermal-Battery Insulations, Sandia Report SAND95-1649 · UC-920, Sandia National Laboratories, Albuquerque, NM, August 1995.

[7] Communication from Cecilia Lam of National Research Council Canada, September 2016.

[8] Air – Thermal Conductivity. https://www.engineeringtoolbox.com/air-properties-viscosity-conductivity-heat-capacity-d_1509.html

[9] Y. Ko, C. Lam, E. Gibbs, P. Lafrance, M. Weinfurter. (2020) Rail tank cars exposed to fires: experimental analyses of thermal conditions imposed to a railcar engulfed in crude oil fires (series 1-3 tests), in press, NRC Report No.: A1-010647-01, National Research Council Canada.

[10] Crude Oil Equation of State Final Report – October 18, 2019. https://tc.canada.ca/en/dangerous-goods/crude-oil-research

[11] Andre Guerra, Robert Symonds, Samantha Bryson, Christopher Kirney, Barbara Di Bacco, Arturo Macchi, Robin Hughes. Five-Lump Mild Thermal Cracking Reaction Model of Crude Oils and Bitumen with VLE Calculations, Industrial & Engineering Chemistry Research 2019 58 (36), 16417-16430

[12] J. Singh, M. M. Kumar, A. K. Saxena, and S. Kumar, "Reaction pathways and product yields in mild thermal cracking of vacuum residues: A multi-lump kinetic model," Chem. Eng. J., vol. 108, no. 3, pp. 239–248, 2005.

[13] K. L. Kataria, R. P. Kulkarni, A. B. Pandit, J. B. Joshi, and M. Kumar, "Kinetic Studies of Low Severity Visbreaking," *Ind. Eng. Chem. Res.*, vol. 43, no. 6, pp. 1373–1387, 2004.

[14] Frank P. Incropera, David P. DeWitt, Fundamentals of Heat and Mass Transfer, John Wiley & Sons, 1990.

Appendix A: US DOT/FRA Validation

The model results were compared to measurements from a US DOT/FRA experiment [5] in this validation exercise. This validation shows that the model can predict the measured heat transfer rate. It also shows that the heat transfer rate to the lading is limited by the radiant output of the fire, even when the fire is in contact with the tank. In the experiment, a 1/3-scale (1/27-volume) tank containing water was exposed to an engulfing fire to measure PRV performance in a potential tank car derailment. Pressure relief predictions from the model were compared to the experimental observations. Since the lading response inside the tank was also measured, this provided an opportunity to validate models by simulating a water lading. This validation study also shed light on heat transfer inside the tank. The effect of thermal radiation transfer from the shell adjacent to the gas headspace into the tank was considered.

2-D CFD Model

The 2-D CFD tank car model was simulated with a water lading, and with two potential boundary conditions representing the fire:

1. A temperature-specified boundary condition applied to the outside surface of the shell or thermal protection. This assumes the fire maintains the shell at the fire temperature.

2. A boundary condition describing radiant exchange between the fire and the outside surface of the shell or thermal protection. This assumes the heat output of the fire is limited by its radiation and that the fire does not always maintain the shell at the fire temperature.

The FRA experimental data included four directional flame thermometer measurements of the fire. There was some interpretation required to specify the fire temperature of the experiment because the measured temperatures depended on both location and time (single, nominal values are provided here). There was also some uncertainty for the emissivity of the steel shell and thermal protection. To account for the uncertainty, the following four cases were specified:

Case A: Radiation boundary, high fire temperature (nominally 777°C), high emissivity (0.9 steel, 0.7 thermal protection)

Case B: Temperature boundary, high fire temperature (nominally 777°C), high emissivity (0.9 steel, 0.7 thermal protection)

Case C: Radiation boundary, low fire temperature (nominally 627°C), low emissivity (0.8 steel, 0.6 thermal protection)

Case D: Temperature boundary, low fire temperature (nominally 627°C), low emissivity (0.8 steel, 0.6 thermal protection)

Figure A.1 shows the predicted and measured liquid water temperature and Figure A.2 shows the predicted and measured tank pressure. The predicted curves become dotted when the conditions for water boiling are reached, since the CFD model does not account for evaporation. Note that evaporation

effects will have already begun before the start of the dotted curves. The pressure curves are not expected to be accurate because the tank pressure will be affected by evaporation since water is relatively volatile compared to crude oil. The temperature curves, on the other hand, are expected to be accurate because most of the heat transfer occurs by free convection of the liquid, which is not significantly affected by pressure. (The HYSYS calculation will account for evaporation and, hence, provide an accurate pressure.) Cases A and C, which employ the radiation boundary condition representing the fire, are found to be consistent with the observed behavior of the tank, whereas Cases B and D, which employ the temperature boundary condition, result in much too rapid heating. It is, therefore, clear that the lading heat-up is limited by the radiant output of the fire even though the fire is in contact with the tank. This was the anticipated behaviour once it was found that low-viscosity liquids in bare tanks are capable of transferring much higher heat fluxes than the fire can actually radiate, and this expected behavior has been borne out by the experiment, which involved a low viscosity liquid (water) in a tank that was bare on its underside. Case C provides the temperature profile that is closest to the experimental measurement. The pressure for Case C is significantly lower than the experimental measurement, indicating that water evaporation, indeed, does affect the pressure in the tank.

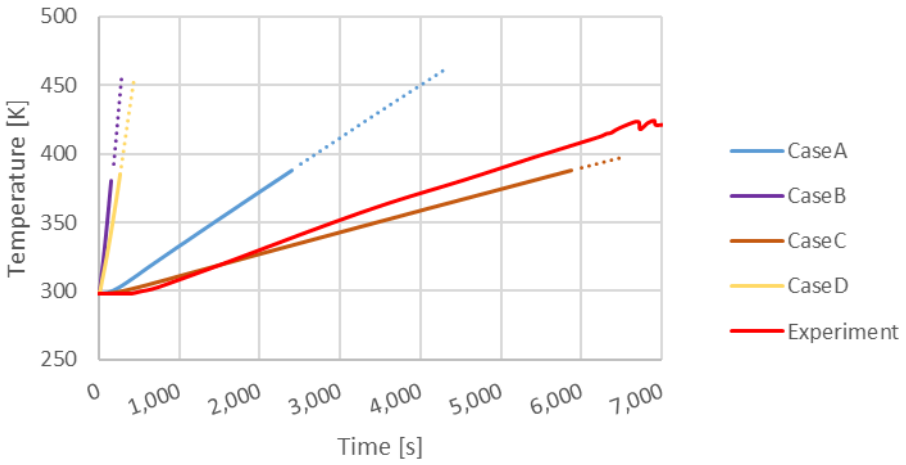

Figure A.1: Volume-averaged liquid water temperature versus time. Cases A-D refer to the CFD simulations. Note that the experimental temperatures have been shifted to account for the starting temperature in the experiment having been 37°C instead of 25°C.

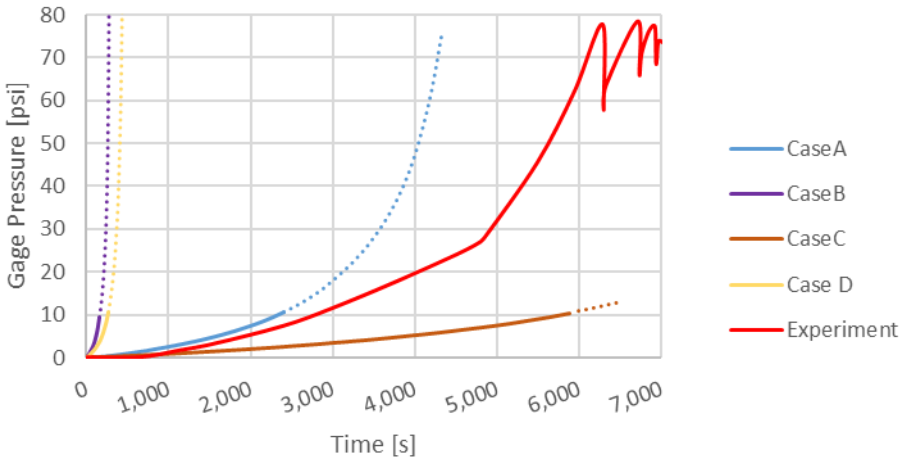

Figure A.2: Tank pressure versus time. Cases A-D refer to the CFD simulations.

The heat flux to the lading versus time for Case C is provided in Figure A.3. The average liquid temperature result from this case came the closest to the measurement, as shown in Figure A.1. The heat transfer rate ramps up over approximately the first ten minutes and then plateaus, with a slow decline thereafter as the lading temperature rises.

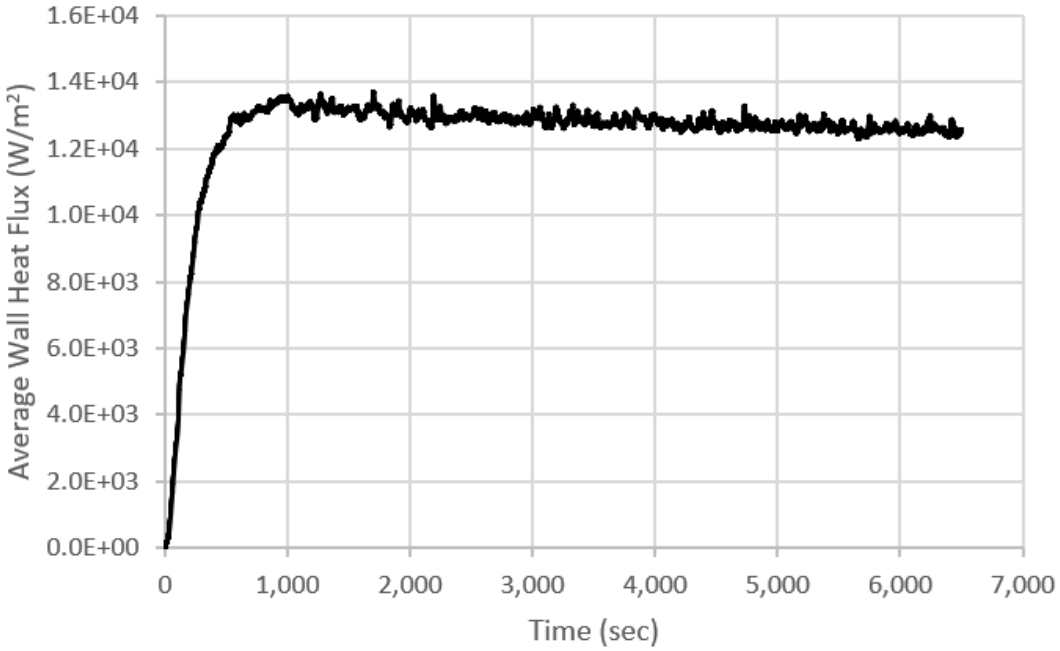

Figure A.3: Average heat flux into the tank for Case C

HYSYS Model

The heat flux profile from Figure A.3 was used as an input to the HYSYS simulation of the tank, which accounted for water evaporation. The tank pressure response from HYSYS is shown in Figure A.4, which shows that the predicted time to reach the relief pressure was within 5% of the experiment. Moreover, the HYSYS model continued to track additional pressure relief events and the resulting frequency and amplitude of the tank pressure response closely matched the experimental measurement. Note the importance of evaporation when water is the lading. Water is much more volatile than crude oil, resulting in a large difference in tank pressure between the CFD and HYSYS predictions.

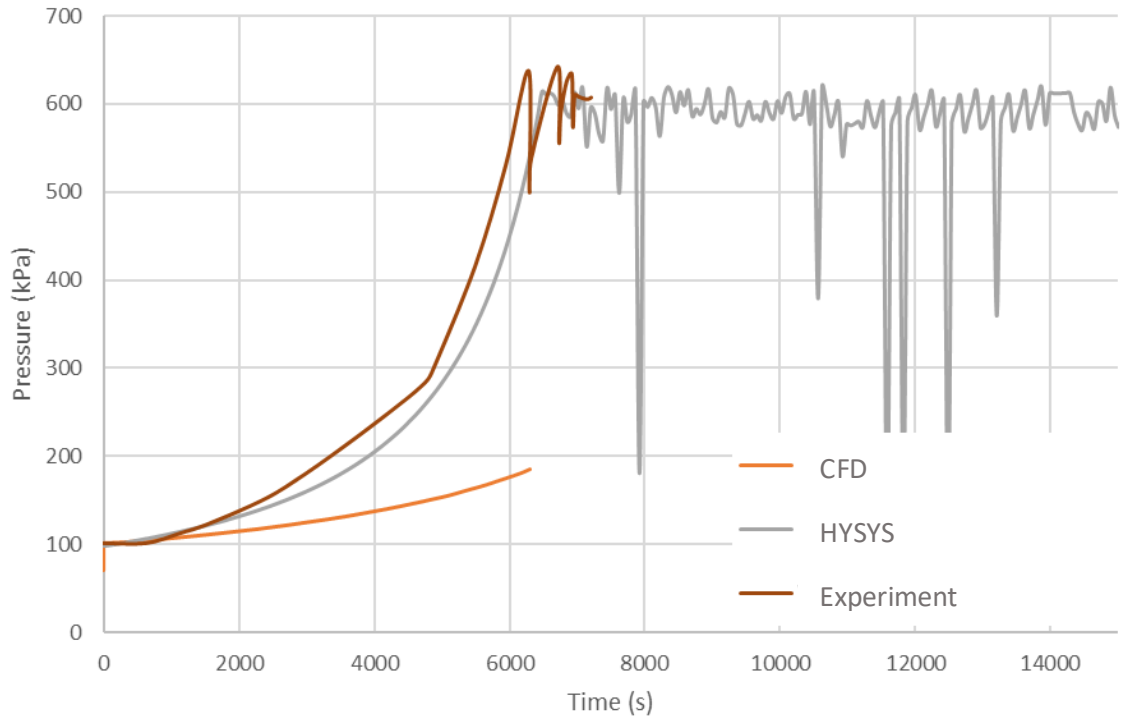

Figure A.4: Tank (absolute) pressure versus time

2-D CFD Model – Radiation inside the Tank

Radiation *inside* the tank was also investigated for one case through a newly available beta feature in ANSYS-CFX. Note that this was a separate study that does not refer to the previous cases specifically. The calculation used the discrete transfer method with 32 discrete directions (rays). The radiant properties were zero absorption coefficient (transparent) in the vapour space and a liquid water absorption

coefficient[1] of 10^4 m^{-1}, which implies very strong absorption given the diameter (*i.e.*, length scale) of the tank. It is interesting to note that liquid water is essentially opaque to thermal radiation in the wavelength range 1 µm to 10 µm (it is far more transparent in the visible range 0.4 µm to 0.8 µm), so there is effectively only radiation from the hot shell to the water surface through the vapour space, much the same as with a crude oil lading. Also note that, even when the shell transfers heat by radiation to the liquid surface, the heated liquid cannot drive convective flow because this liquid is already at the top of the tank. Free convection is driven by warmer, less dense fluid being below cooler fluid. Therefore, radiation from shell to liquid will raise the local liquid temperature rather than drive overall heating inside the tank (for high fill levels).

Figure A.5 shows that there is almost no difference in results with and without radiant transfer inside the tank, at least during the period up to the first pressure relief. This is partly because the fill level is high so there is little hot shell surface and little liquid surface to exchange heat. In addition, for the FRA test, there was thermal protection on top of the tank so the shell did not get as hot as it would have if it were unprotected. This finding might not apply to all tank and fire scenarios, for example to unprotected or poorly protected tanks, to thermally protected tanks heated over long periods, or to low liquid fill levels.

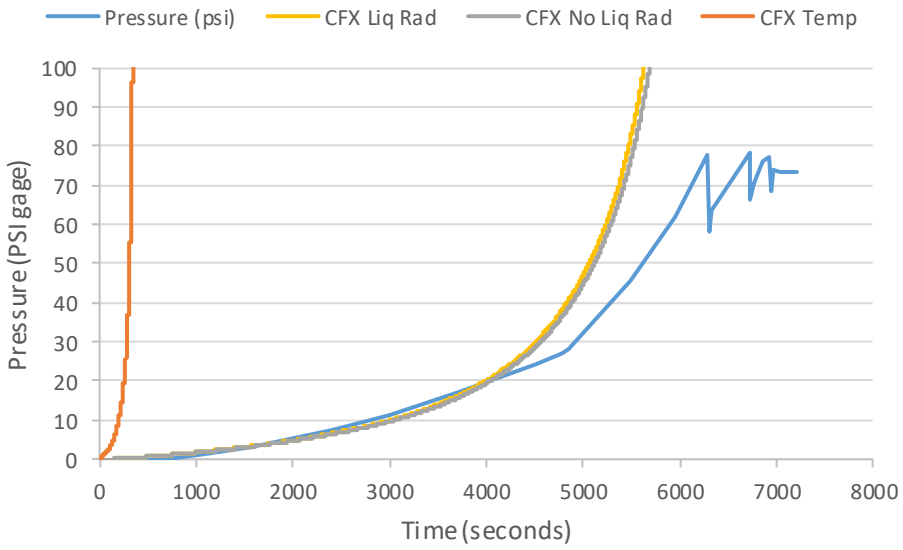

Figure A.5: Pressure versus time for the water tank validation. Orange: CFD - Temperature-specified fire boundary condition, Yellow: CFD - Radiation fire boundary condition, with radiation inside the tank, Grey: CFD - Radiation fire boundary condition, without radiation inside the tank, Blue: Measurement from FRA test (Note that the main emphasis here is not the comparison of the CFD model to experiment but, rather, the comparison of the "with radiation inside" curve to the "without radiation inside" curve.)

[1] See, for example, http://www1.lsbu.ac.uk/water/water_vibrational_spectrum.html or https://en.wikipedia.org/wiki/Electromagnetic_absorption_by_water

Appendix B: Heat Transfer between Jacket and Shell

The thermal protection provided by the annular air gap between the shell and jacket of a double-walled tank was assessed, taking into account conductive, convective, and radiant heat transfer mechanisms, and it was compared to the FyreWrap® thermal protection. The study incorporated a computational fluid dynamics (CFD) model to provide a detailed analysis of the convective heat transfer across the annular air gap. Figure B.1 shows the relevant geometry for this analysis.

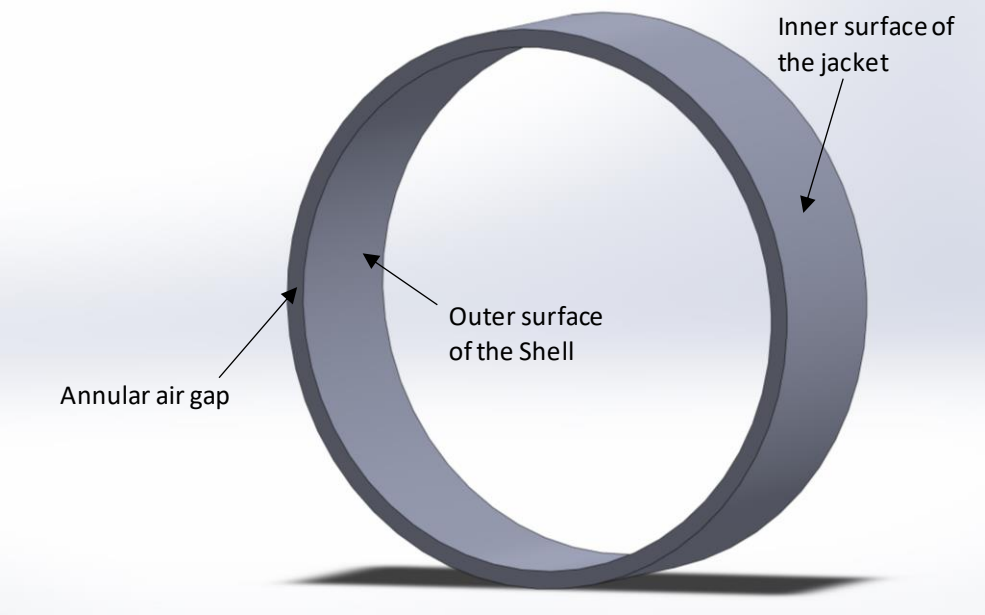

Figure B.1: Relevant geometry of shell and jacket. Note that this geometry represents the annular air gap between the shell and jacket, *i.e.*, it is not a solid.

Concepts

Conduction refers to the diffusion of heat via random motions of air molecules. Fourier's law describes the overall heat transfer. The planar solution to Fourier's law illustrates the nature of conduction, in which the heat flux (W/m^2) is given by

$$q" = \frac{k}{L}(T_H - T_C) \qquad \text{(B.1)}$$

where k is the thermal conductivity $(W/(m \cdot K))$ of the air, T_H and T_C are the temperatures $(K \; or \; ℃)$ of the hotter and colder surfaces respectively, and L is the distance (m) between the surfaces.

Convection refers to heat transfer by the bulk, or average or collective, motion of the air. Newton's law of heating/cooling describes this heat flux,

$$q'' = h(T_H - T_C) \quad \text{(B.2)}$$

where h $(W/(m^2 \cdot K))$ is the convection coefficient, and T_H and T_C are the temperatures $(K\ or\ ℃)$ of the surface and the surrounding air respectively. The type of convection in this case is free, or natural, convection as opposed to forced convection.

Radiant heat is transported by electromagnetic waves, the same type of waves that transmit light. The nature of radiation is illustrated by the Stefan-Boltzmann law, which, below, describes the radiant exchange between two flat, parallel, infinite, black surfaces with a non-participating medium between them,

$$q'' = \sigma\left({T_H}^4 - {T_C}^4\right) \quad \text{(B.3)}$$

where σ is the Stefan-Boltzmann constant $(W/(m^2 \cdot K^4))$, and T_H and T_C are the absolute temperatures (K) of the hotter and colder surfaces respectively.

Comparing Equations (B.1) to (B.3), we note that conduction and convection increase in proportion to temperature whereas radiation increases in proportion to the fourth power of temperature. Consequently, radiation increasingly dominates with higher temperature and it is expected to dominate in high temperature crude oil pool fires.

Free convection flow can be either turbulent or laminar. The Rayleigh number calculated for this flow between two plates indicated that it is laminar. The Raleigh number also indicated that the flow should not be greatly affected by disturbances in the third (axial) direction. Since the geometry and boundary conditions do not vary in the axial direction (at least in terms of the present calculation), significant flow patterns involving this spatial dimension are not expected. This enables the problem to be simplified to a two-dimensional description of an infinitely long cylinder, in which the end effects of the tank are neglected.

CFD Model

The ANSYS-CFX® software, version 18.0, was used to create the model. The outside diameter of the shell was 118 7/16 inches. There was a 4-inch annular gap between the outer surface of the shell and the inner surface of the jacket. Since the model was two-dimensional, the geometry consisted of a ring having arbitrary thickness of 0.01 meters and translational periodicity was applied as the boundary condition on the vertical planes bounding the ring.

The temperature of the jacket was assumed to reach 900°C. The radiation from the jacket to the shell is automatically bounded by the blackbody radiation at 900°C. The shell was set to 60°C as a representative temperature when the liquid is effectively cooling it. The emissivity of the two surfaces was set to 0.8 to represent the radiant properties of steel.

The air in the annular gap does not participate in thermal radiation. Table B.1 lists the relevant properties of air for conduction and convection.

Table B.1: Density ($\boldsymbol{\rho}$), specific heat ($\boldsymbol{C_p}$), dynamic viscosity ($\boldsymbol{\mu}$), and thermal conductivity ($\boldsymbol{k}$) of air

Properties of Air at Atmospheric Pressure				
$T\ (K)$	$\rho\ (kg/m^3)$	$C_p\ (kJ/(kg\cdot K))$	$\mu\ (kg/(m\cdot s))$	$k\ (W/(m\cdot K))$
300	1.1774	1.0057	1.85E-05	0.02624
350	0.998	1.009	2.08E-05	0.03003
400	0.8826	1.014	2.29E-05	0.03365
450	0.7833	1.0207	2.48E-05	0.03707
500	0.7048	1.0295	2.67E-05	0.04038
550	0.6423	1.0392	2.85E-05	0.04360
600	0.5879	1.0551	3.02E-05	0.04659
650	0.543	1.0635	3.18E-05	0.04953
700	0.503	1.0752	3.33E-05	0.05230
750	0.4709	1.0856	3.48E-05	0.05509
800	0.4405	1.0978	3.63E-05	0.05779
850	0.4149	1.1095	3.77E-05	0.06028
900	0.3925	1.1212	3.90E-05	0.06279
950	0.3716	1.1321	4.02E-05	0.06525
1000	0.3524	1.1417	4.15E-05	0.06752
1100	0.3204	1.16	4.44E-05	0.07320
1200	0.2947	1.179	4.69E-05	0.07820

Extensive checks on the model setup were performed (the spatial grid and the number of radiation rays), the boundary conditions, the material properties, and the solver settings) by checking the accuracy of numerical results for simpler conduction, convection, radiation, and combined mode problems with known solutions. Based on these checks, it was decided to use the surface-to-surface discrete transfer radiation model with eight rays. The computational mesh was created with approximately 1.6 million elements. The laminar flow solver was used because the value of the Rayleigh number suggested the free convection flow was laminar.

Results

Figure B.2 shows the air velocity profile in the annulus between shell and jacket. This flow pattern is expected. Rolling eddies are present at the bottom, resembling the flow pattern between parallel horizontal plates in which the bottom plate is hotter than the top plate. The highest convective heat transfer occurs along the sides of the tank, where the eddies are more elongated and the flow speeds are highest. Toward the top of the tank, the flow begins to stabilize and at the very top, there is no convective motion, as would be the case between parallel horizontal plates in which the bottom plate is colder than the top plate.

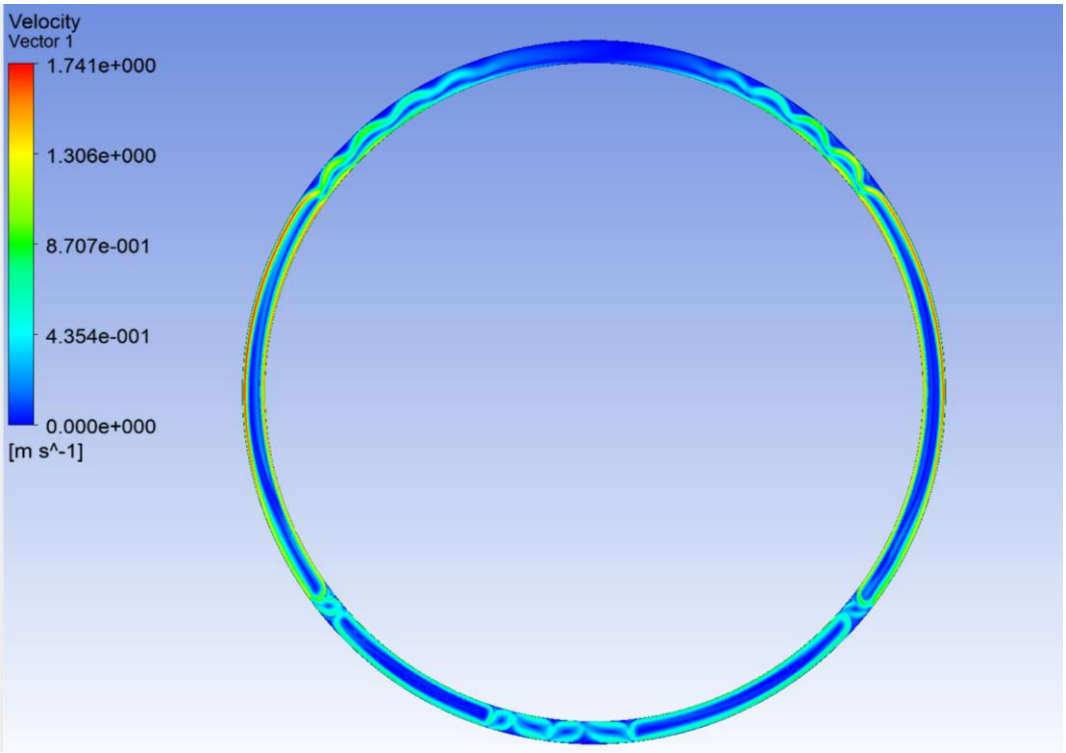

Figure B.2: Velocity [m/s] profile in the annulus between shell and jacket

Table B.2 shows the average, maximum, and minimum total heat flux (which includes convection, conduction, and radiation) and the same for combined convection and conduction only. The average heat fluxes show that convection and conduction account for only about 3% of the total heat transfer. Radiation is the dominant mode of heat transfer. Note that the average total heat fluxes for the inside of the jacket and outside of the shell are different. This does not reflect a failure to conserve energy; rather, it reflects the difference in surface area between the inside of the jacket and outside of the shell, since they are heat fluxes, not flows.

Table B.2: The average, maximum, and minimum total heat fluxes and the same for combined convection and conduction only

	Total Heat Flux (W/m^2)			Convection and Conduction only (W/m^2)		
	Average	Max	Min	Average	Max	Min
Inside of Jacket	68748	84906	66754	2052	18211	60
Outside of Shell	73437	83103	71370	2237	11890	176

Conduction is the only mode of heat transfer present when using the FyreWrap® thermal protection. The resulting heat flux for the same set of conditions was 7 kW/m^2.

The heat transfer by conduction and convection was compared in the CFD simulation to that obtained using the correlation for concentric cylinders provided by Incropera and DeWitt [14]. This direct comparison is possible because radiation is independent of conduction/convection because the air does not absorb or emit radiation (it is non-participating). Table B.3 contains the experimental correlation and CFD simulation results for the combined convection and conduction heat transfer. Note that the heat transfer is expressed on a per-unit-length basis (in the axial direction of the tank), not per-unit-area. The CFD results agree with the experimental correlation within approximately 10%. This is an acceptable difference, as the correlation was created based on experimental data where the experimental geometry and conditions would certainly have been much different from the rail car tank.

Table B.3: Combined convection and conduction heat transfer per unit length: the CFD simulation compared to the experimental correlation

Average Combined Convection and Conduction Heat Transfer Per Unit Length (W/m)		
CFD Simulation	Inside of Jacket	20706
	Outside of Shell	21143
Experimental Correlation from Incropera and DeWitt [14]		23448

Discussion: Method to Suppress Radiant Heat Transfer

It has been shown that the annular gap is not effective at blocking heat transfer and that radiation is the dominant mechanism for heat transfer across this gap. The narrow profile of the annulus effectively suppresses convective heat transfer (convection flow occurs but its contribution to the total heat transfer is small compared to radiation). Heat conduction through the air is also comparatively small.

As shown in Figure B.3, it is suggested to coat the steel surfaces with a low-emissivity paint or material to suppress radiant transfer. The low-emissivity surface property has the effect of reducing emission of radiation from hot surfaces and increasing reflection of radiation from cold surfaces.

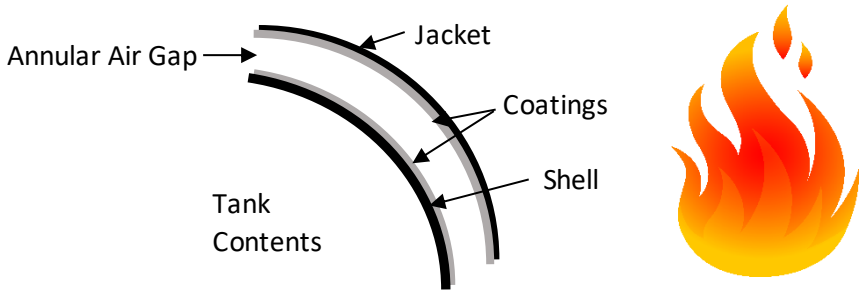

Figure B.3: Potential thermal protection strategy

The heat transfer was calculated assuming a coating emissivity of 0.1, which represents an achievable low-emissivity coating. Table B.4 provides the expected average heat fluxes into the shell. Coating the outer surface of the shell achieves an 82% reduction in heat transfer. Coating both the outer surface of the shell and the inner surface of the jacket achieves an 89% reduction in heat transfer. Surface coatings might provide a sufficient heat transfer barrier and be more cost-effective and durable than the ceramic fiber blanket.

Going a step further, the optimum annular air gap width was calculated, that is, the gap width that minimizes heat transfer. Reducing the annular gap width suppresses the natural convection flow but conduction heat transfer begins to dominate for very small gaps. The optimal gap width was found to be 1-inch instead of the standard 4-inch gap, although the reduction in heat flux was not substantial.

Table B.4: Expected heat transfer. The coating has emissivity of 0.1.

Thermal protection strategy	**Average heat flux (kW/m^2)**
Annular air gap with no surface coatings	73.4
Coating the inner surface of the jacket only	13.2
Coating the outer surface of the shell only	12.9
Coating both the outer surface of the shell and inner surface of the jacket	8.1
Coating both outer shell and inner jacket, 1-inch air gap instead of 4-inch	7.8
No surface coating, use of 1/2 inch-thick ceramic fiber thermal protection	7.0

Conclusions

Radiation is the main contributor to heat transfer when air is the thermal protection in the annulus between the shell and jacket. Convection and conduction contributed only approximately 3% of the total heat flux. The average heat flux entering the outer shell was 73.4 kW/m^2 with the maximum heat flux reaching 83.1 kW/m^2. For comparison, the measured heat flux from fires is typically around 100 kW/m^2, meaning that the annular air gap provides little thermal protection.

An alternative thermal protection method was proposed and analyzed. It is achieved by coating the outer surface of the shell and/or the inner surface of the jacket with a low-emissivity (emissivity of 0.1) coating. Compared to the air gap with no coating, an 89% reduction in heat transfer to the shell was achieved when coating both the outer surface of the shell and inner surface of the jacket. Its effect is approximately the same as that of the 1/2 inch-thick ceramic fiber blanket.